

**Passive biomimetic actuators:  
the role of material architecture**

**Dissertation**

Zur Erlangung des akademischen Grades  
Doktor der Naturwissenschaften (Dr. rer. Nat.)  
in der Wissenschaftsdisziplin "Science of Biomaterials"

eingereicht an der  
Mathematisch-Naturwissenschaftlichen Fakultät  
der Universität Potsdam

angefertigt am  
Max-Planck-Institut für Kolloid- und Grenzflächenforschung

von

**Lorenzo Guiducci**

geboren am 1. Februar 1982 in Carrara, Italien  
Potsdam, im November 2013

This work is licensed under a Creative Commons License:  
Attribution - Noncommercial - Share Alike 3.0 Unported  
To view a copy of this license visit  
<http://creativecommons.org/licenses/by-nc-sa/3.0/>

Published online at the  
Institutional Repository of the University of Potsdam:  
URL <http://opus.kobv.de/ubp/volltexte/2014/7044/>  
URN [urn:nbn:de:kobv:517-opus-70446](http://nbn-resolving.org/urn:nbn:de:kobv:517-opus-70446)  
<http://nbn-resolving.org/urn:nbn:de:kobv:517-opus-70446>

*a Fede*  
*...e al nostro passero pure!*



## Contents

Abstract.....	9
1. Introduction .....	13
2. Basic Concepts .....	17
2.1 Material architecture in passive actuators .....	20
2.1.1 Stiff fibres in swellable matrix.....	20
2.1.2 Constrained swelling in a closed cellular structure.....	27
2.2 Two dimensional cellular materials .....	29
2.2.1 Shape, size, topology.....	29
2.2.2 Honeycomb mechanics.....	32
2.2.3 Estimation of cellular materials properties by numerical homogenization	
34	
2.3 Volumetric changes by fluid sorption.....	36
2.3.1 Statistical treatment of swelling.....	37
2.3.2 Adsorption .....	41
3. Materials & Methods .....	49
3.1 Finite Element analysis of pressurised periodic lattices .....	50
3.1.1 Finite Element method .....	51
3.1.2 Geometry of the cellular structures .....	54
3.1.3 Simulation details: prescribed conditions.....	55

3.1.4	Estimation of swelling eigenstrains and elastic properties .....	58
3.1.5	Finite-size, periodic system comparison .....	59
3.2	Micromechanical analysis of pressurised lattices .....	60
3.2.1	A fluid-structure model .....	60
3.2.2	Parameterization of the fluid-structure potential .....	62
3.3	Swelling experiments of honeycombs .....	64
3.3.1	Generation of 3D models.....	64
3.3.2	Materials synthesis and swelling protocol.....	65
3.3.3	Assessment of mechanical and swelling properties .....	67
3.4	Monte-Carlo simulations of water in nanosized pores .....	67
3.4.1	Monte Carlo simulations of molecular systems.....	68
3.4.2	The TIP4P/2005 water model.....	69
3.4.3	Simulation details for bulk water system .....	71
3.4.4	Preliminary results of the simulations of bulk water .....	73
4.	Results.....	75
4.1	Finite Element analysis of pressurised anisotropic honeycombs .....	75
4.1.1	Microscopic deformation and macroscopic behaviour upon pressurization 75	
4.1.2	Influence of fluid pressure and wall stiffness on swelling eigenstrains ....	80
4.1.3	Influence of fluid pressure and material stiffness on apparent honeycomb stiffness 81	
4.2	Micromechanical analysis of diamond honeycombs .....	82
4.2.1	Strain energy density and swelling eigenstrains .....	84
4.2.2	Lattice apparent stiffness .....	85
4.2.3	Honeycomb based actuator.....	88
4.2.4	Tuneable Poisson's ratio material .....	90
4.3	Role of architecture in the expansion of non-convex lattices .....	91
4.3.1	Two-scale deformation of non-convex lattices.....	92
4.3.2	Microscopic patterns and macroscopic deformations of non-convex lattices 94	
4.3.3	Generation of macroscopic anisotropy and shearing expansions .....	102

4.3.4	Influence of cell convexity on swelling eigenstrains .....	104
4.3.5	Influence of lattice connectivity on swelling eigenstrains .....	105
4.3.6	Apparent stiffness.....	109
4.3.7	Conclusions.....	113
4.4	Swelling in composite bidimensional cellular solids.....	114
4.4.1	Hydrogel filled honeycomb .....	114
4.4.2	Mechanical and free swelling properties of rapid prototyped materials .	116
4.4.3	Honeycombs with soft inclusions .....	117
4.4.4	Non-convex lattices.....	125
4.4.5	Conclusions.....	127
5.	Conclusions & Outlook .....	129
6.	Publications .....	136
7.	References .....	137
	Acknowledgements .....	143





## Abstract

Passive plant actuators have fascinated many researchers in the field of botany and structural biology since at least one century. Up to date, the most investigated tissue types in plant and artificial passive actuators are fibre-reinforced composites (and multilayered assemblies thereof) where stiff, almost inextensible cellulose microfibrils direct the otherwise isotropic swelling of a matrix. In addition, Nature provides examples of actuating systems based on lignified, low-swelling, cellular solids enclosing a high-swelling cellulosic phase. This is the case of the *Delosperma nakurense* seed capsule, in which a specialized tissue promotes the reversible opening of the capsule upon wetting. This tissue has a diamond-shaped honeycomb microstructure characterized by high geometrical anisotropy: when the cellulosic phase swells inside this constraining structure, the tissue deforms up to four times in one principal direction while maintaining its original dimension in the other.

Inspired by the example of the *Delosperma nakurense*, in this thesis we analyze the role of architecture of 2D cellular solids as models for natural hygromorphs. To start off, we consider a simple fluid pressure acting in the cells and try to assess the influence of several architectural parameters onto their mechanical actuation. Since internal pressurization is a configurational type of load (that is the load direction is not fixed but it “follows” the structure as it deforms) it will result in the cellular structure acquiring a “spontaneous” shape. This shape is independent of the load but just depends on the

architectural characteristics of the cells making up the structure itself. Whereas regular convex tiled cellular solids (such as hexagonal, triangular or square lattices) deform isotropically upon pressurization, we show through finite element simulations that by introducing anisotropic and non-convex, reentrant tiling large expansions can be achieved in each individual cell.

The influence of geometrical anisotropy onto the expansion behaviour of a diamond shaped honeycomb is assessed by FEM calculations and a Born lattice approximation. We found that anisotropic expansions (eigenstrains) comparable to those observed in the keels tissue of the *Delosperma nakurense* are possible. In particular these depend on the relative contributions of bending and stretching of the beams building up the honeycomb. Moreover, by varying the walls' Young modulus  $E$  and internal pressure  $p$  we found that both the eigenstrains and 2D elastic moduli scale with the ratio  $p/E$ . Therefore the potential of these pressurized structures as soft actuators is outlined.

This approach was extended by considering several 2D cellular solids based on two types of non-convex cells. Each honeycomb is build as a lattice made of only one non-convex cell. Compared to usual honeycombs, these lattices have kinked walls between neighbouring cells which offers a hidden length scale allowing large directed deformations. By comparing the area expansion in all lattices, we were able to show that less convex cells are prone to achieve larger area expansions, but the direction in which the material expands is variable and depends on the local cell's connectivity. This has repercussions both at the macroscopic (lattice level) and microscopic (cells level) scales. At the macroscopic scale, these non-convex lattices can experience large anisotropic (similarly to the diamond shaped honeycomb) or perfectly isotropic principal expansions, large shearing deformations or a mixed behaviour. Moreover, lattices that at the macroscopic scale expand similarly can show quite different microscopic deformation patterns that include zig-zag motions and radical changes of the initial cell shape. Depending on the lattice architecture, the microscopic deformations of the individual cells can be equal or not, so that they can build up or mutually compensate and hence give rise to the aforementioned variety of macroscopic behaviours. Interestingly, simple geometrical arguments involving the undeformed cell shape and its local connectivity enable to predict the results of the FE simulations. Since the lattices' microstructure

changes so drastically upon pressurization, a corresponding change in their apparent elastic properties is observed. Depending on the direction along which the beams align, the lattices can stiffen along their principal axes or become more compliant. Also a generalized increase of the shearing rigidity is observed.

Motivated by the results of the simulations, we also created experimental models of such actuating structures. 3D printing was used to produce both anisotropic diamond shaped honeycombs and non-convex cellular solids made of two components: a stiff phase for the walls and a soft swellable phase for inclusions/ layers lining the cell. When swollen, the models undergo substantial deformation with deformation patterns qualitatively following those predicted by the simulations. In these systems though the anisotropy of swelling depends also on the choice of the materials for walls and inclusions. In particular, anisotropy arises as a consequence of the mismatch in free swelling between stiff and soft materials. To assess this evidence we derived an analytical model that predicts the swelling expansions in a diamond honeycomb with stiff walls and soft inclusions. When the ratio between materials stiffness is too low, the expansion is isotropic. When the walls are several orders of magnitude stiffer than the inclusions, no swelling is observed. In our prediction a stiffness ratio of 100 to 1000 maximizes both the anisotropy and expansion along the honeycomb's soft axis. A major difference between the swelling and pressurized honeycombs simulated via FE is that while in the pressurized honeycombs the eigenstrains scale with the ratio  $p/E$ , in the swelling system there isn't such a scaling law and the swelling expansion depends on the absolute values of both the walls and inclusions elastic modulus.

This work highlights how the internal architecture of a swellable cellular solid can lead to complex shape changes which may be useful in the fields of soft robotics or morphing structures.



## 1. Introduction

Passive plant actuators have fascinated many researchers in the field of botany and structural biology since at least one century [1-4]. A more recent rediscovery of these systems has occurred in the fields of bioinspired engineering and materials design [5-8] where concepts peculiar to actuating biological systems have been transferred to technological applications such as morphing structures [9] and soft robotics [10-13]. Here at least three fundamental features can be isolated; for first, their ability to generate a complex actuation –that is desired motion and/or force- in absence of a metabolic source of energy; secondly, the observation that complex actuation results from proper distribution of materials with contrasting properties; and finally, that different material properties are mainly achieved by controlling their structure at several hierarchies, since in natural materials the choice of basic constituents is limited [7, 14, 15].

Up to date, the most investigated tissue types in plant and artificial passive actuators are fibre-reinforced composites (and multilayered assemblies thereof) where stiff, almost inextensible cellulose microfibrils direct the otherwise isotropic swelling of a matrix [8]. In addition, Nature provides more examples of actuating systems based on tissue architectures that reach beyond the class of fibre reinforced composite materials, as in the case of the *Delosperma nakurense* seed capsule. Here, a remarkable, reversible, hygroscopic unfolding of the seed valves is powered by water sorption occurring in a specialized tissue (hygroscopic keel) [16]. At a macroscopic scale this tissue is based on a

## 1. Introduction

highly anisotropic honeycomb structure, with lignified walls enclosing a cellulosic inner layer (CIL). At a lower scale, the cellulosic inner layer exhibits an open structure with porous lamellae filling the gap between denser cellulosic mats [17]. Due to its porous microstructure reminiscent of a hydrogel, swelling of the CIL happens only at partial pressures of water close to saturation. Then, the anisotropic honeycomb structure acts as a constraint for the CIL free swelling. As a result the tissue deforms up to four times in one principal direction while maintaining its original dimension in the other. The case of the *Delosperma nakurense* seed capsule is highly inspiring because shows that materials' structure both regulates the onset of swelling (at micro- and nanoscale) and complex actuation (at macroscale). The co-presence of many levels of structure (typical in natural materials) might influence the water-substrate interaction in materials that actuate by swelling. Designing a material at the nanoscale exerts dramatic changes in its macroscopic properties [18]. This applies also to the adsorption of fluid on solids with a nanoscopic porosity ( $50\text{nm} > d_{\text{pore}} > 2\text{nm}$ ). Here, as the size of the pores becomes comparable to that of the fluid molecules, a nonmonotonic deformation is observed, with the pores contracting at low vapour pressures and expanding at higher pressures [19-21]. On the one hand, this has been studied in exemplary systems involving mesoporous silicates and simple potential fluids like the Lennard-Jones fluid [21, 22]. On the other hand, nanoconfinement of water has also been extensively studied, and showed to influence water's properties [23], although only in rigid undeformable pores. Similarly to what observed in the case of the CIL material, understanding what is the role of nanoporosity on solid-water interactions will help improve our understanding of biological actuators.

Honeycombs and more generally cellular materials have been widely studied given their abundance both in biological and engineering materials [24-28]. Their properties depend mainly on their shape, and scale non-linearly with their density allowing a remarkable control of properties through architecture thus enabling the engineer to fill the so-called "holes in materials property-space" [29]. They cover a big range of structural and functional applications such as low density fillers in hybrid sandwich panels, crash energy absorbers, negative Poisson's ratio materials or thermal/acoustic insulators. Surprisingly, the possibility to use them as building blocks for artificial actuators, as

observed in the *Delosperma nakurense* seed capsule, has been overlooked. In this view, the interplay between their architecture, expansion properties and mechanical performance is crucial.

Therefore, the aims of the present thesis are:

- to simulate several designs of two-dimensional cellular materials and correlate their geometrical and topological features to their actuation behaviour
- to interpret the simulation results in terms of a micromechanical model
- to test simulation and theoretical study by means of swelling experiments on two-materials physical models
- to set up a numerical model to investigate water adsorption in a nanometric slit-pore

The present document has been organized in the following sections:

- Chapter 2 introduces the reader to the topic of passive actuators and delimits the scope of the research. Concepts relative to adsorption and swelling are provided, as well as basic quantities to describe the topological, geometrical and mechanical properties of two-dimensional cellular materials
- Chapter 3 lists the methods used, and motivates their choice; details regarding Monte Carlo and Finite Element simulations are included, and the setup for the swelling experiments.
- Chapter 4 reports the main results obtained; these are critically discussed; also a possible explanation for the major difficulties encountered is given.
- In chapter 5 the main findings are put in the broader picture of passive actuators; also the merits and limits of this work are highlighted with respect to the state of the art.





## 2. Basic Concepts

In the present thesis we refer to actuating materials as a class of materials that are able to generate a reversible complex motion and/or force as a response to an external stimulus. This means that we consider actuation essentially as a mechanical phenomenon. Many materials would fall into this broad definition (e.g. shape memory polymers, shape memory alloys etc) however we focus on those materials that actuate by virtue of the specific architecture and expansion properties of their constituents. It turns out that many of such systems are present in Nature, especially in the plant kingdom.

As a mechanical phenomenon, actuation is a transformation from an initial undeformed state of the material to a final one where its shape has changed. In contrast to a general mechanical phenomenon, this transformation is not due to an external load or boundary condition, but to a contactless interaction between an external field like temperature or humidity. The mapping between these two states is operated by the so called *eigenstrains* which represent the “natural” strains (*eigen*, German for own) that spontaneously originate in the material in response to the external stimulus. In order to obtain a specific desired shape in the actuated state, the eigenstrains are not uniform. In virtually all plant actuators, this is achieved by the distribution, at lower scales, of materials with contrasting expansion properties [1, 2, 5, 8, 14-16, 30, 31]. Therefore understanding the effect of material microstructure to obtain non uniform expansion is crucial.

## 2. Basic Concepts

In plant actuators, the expansion of the basic constituents that form the tissues arise as a consequence of water sorption. Plant tissues are made of large biomolecules (like cellulose, hemicellulose, lignin and pectins) with various chemical formulations. In particular amorphous polysaccharides present in the matrix of plant cells (cellulose, hemicellulose, pectins) are hydrophilic, thus enabling plant tissues to swell when exposed to water. Since sorption is a spontaneous process, some plant actuators are “passive” as they don’t need an internal source of energy to work. Indeed the mechanical energy needed to power actuation results from the difference in chemical potential between the fluid and the solid phase. This characteristic makes these systems simple compared to others [6, 32] where the energy needed for mechanical actuation is obtained by a biological metabolic machinery. In the view of bioinspired material design, passive plant actuators are more appealing: understanding their design rules can lead more promptly to implementation into artificial actuating materials.

As these aspects are crucial to understand how passive actuators work, in the remainder of the chapter we will present in more detail the following topics:

- Architecture of passive actuators. Although material architecture has been extensively studied especially regarding its influence on the mechanical properties, comparatively a lot less is known about the role of architecture on the actuation properties of the material. Most actuating materials studied so far are fibre reinforced composites where stiff inextensible fibres are dispersed in a swellable matrix. This strategy is implemented in wood in order to generate stresses and small deformations at the cell level. A different class of actuating materials, as epitomized by the *Delosperma nakurense*, is based on cellular materials. Here the swelling phase is located inside the cells of the tissue. In subchapter 2.1 we will present (giving relevant examples) these two main categories of architectures: fibre reinforced and cellular materials with constrained swelling.
- Cellular materials. Whereas for fibre reinforced materials the possibility are mainly limited to the choice of the basic constituents for matrix and fibres and the orientation of the fibres, in cellular materials the architecture is implemented at the tissue level which extends the range of possibilities: cellular materials show a

## 2. Basic Concepts

vast range of properties depending on their apparent density and the geometry of their cells. Although this is very well known with respect to their structural mechanical properties (stiffness, toughness, etc), the geometry of cellular materials strongly affects their actuation properties too and this surprisingly has not been investigated till now. A basic introduction about cellular materials will therefore be given in subsection 2.2.

- Volumetric changes by fluid sorption. As plant actuators are based on the sorption of water into the tissues, some aspects of the physics of sorption will be introduced in subchapter 2.3. This same phenomena are also relevant for many artificial systems, in which the interaction between solid and fluid can be enhanced by nanoscopic confinement.

In the view of the writer, the aforementioned aspects are necessary to properly introduce the reader to the matter. From this brief introduction, it can be deduced that material actuation will be treated as a static phenomenon. Nonetheless, a more complete description of passive actuating materials should consider the transport of the fluid phase in the material [33].

As water transport is a dynamic phenomenon, plant actuators will work at different limiting speeds depending on the characteristic dimension of their tissues (usually the smallest macroscopic dimension of the moving part) [34]. To generate faster movements many plant systems implement elastic instabilities. Fast movements are the result of the abrupt transition from a mechanical high energy state to a low energy one due to a buckling event. Examples of these are snap-buckling of thin shells due to their curvature inversion as for the leaves of the Venus flytrap [6] and the trap door of the underwater *Utricularia* [32] or explosive fracture of ferns' spore capsules [8].

## 2. Basic Concepts

### 2.1 Material architecture in passive actuators

#### 2.1.1 *Stiff fibres in swellable matrix*

Fibre reinforced materials are composite materials based on stiff fibres embedded in a compliant matrix. When the matrix undergoes a volumetric change due to temperature or humidity change, a resulting anisotropic expansion occurs.

In plants, one of the strategies used is to control the anisotropic deformation of cells upon swelling and shrinking by an adjustment of the cell wall architecture [8]. These walls are built as composites of stiff cellulose fibrils embedded in a swellable matrix composed of a variety of macromolecules such as hemicelluloses, pectin and lignin. Cellulose fibrils are composed of (infinitely) long glucan chains based on 1-4 glucose that pair laterally forming a network of classical O–H $\cdots$ O hydrogen bonds (HBs) and nonconventional C–H $\cdots$ O contacts [35]. The resulting molecular structure is crystalline and shows outstanding mechanical properties, with an estimated longitudinal stiffness of 137 GPa [36]. Also this structure help to render the material insoluble in water and most organic solvents, although cellulose fibrils can be dissolved or swollen in presence of ionic liquids [37].

Hemicelluloses are chemically affine to cellulose, but they have a branched structure. The similar chemical structure enables them to attach to the cellulose whereas the branching ensures anchoring in the matrix. The rest of the matrix is composed of pectins which are hydrophilic short chained sugars, and lignin which is a large polyaromatic molecule. The aromatic rings are thought to give a hydrophobic character to this molecule. This molecule is produced at later developmental stages and is involved in cross linking of the matrix which increases its stiffness.

The multilayered fibre-reinforced structure of the cell wall stems from the developmental stages of plant cell growth, when complex machineries called cellulose synthase complexes lay down cellulose microfibrils on the plasma membrane in a spiralling fashion [38, 39]. These units are attached and guided by microtubules in the cytoskeleton so that the cell controls the direction of deposition [40], thereby influencing the cell shape [41]. At later stages, new layers of cell wall continue to form, with the microfibril orientation now set to increase the cell wall mechanical stability.

Material	$E_l$ [GPa]	$E_t$ [GPa]	$G_{lt}$ [GPa]	$\varepsilon_l$	$\varepsilon_t$
<b>Cellulose</b> (transversely isotropic)	150	17.5	4.5	0	0
<b>Hemicellulose</b> (transversely isotropic)	8	3.4	1.2	0	0.5
<b>Lignin</b> (isotropic)	6			0.333	

**Table 2-1** Estimated mechanical and expansion properties of the wood polymers (taken from [42]).

*Engineering constants refer to the dry polymers;  $l$  and  $t$  subscripts stand for the longitudinal and transversal direction (for transversely isotropic materials). The expansion strains refer to a change from 0% to 100% in environment relative humidity.*

Besides being involved in the growth processes and mechanical stabilization of their walls, plant cells control the cellulose orientation to generate a prestress in the tissues (as in various type of woods [43]) or build passive systems actuating upon swelling and shrinking. In this highly organized structure, swelling is possible only perpendicularly to the stiff non-swelling cellulose fibrils [8, 40, 41]. Therefore their orientation, measured by the microfibril angle (MFA), is crucial to assess the direction at which the wood cell will expand due to swelling.

In an effort to understand the mechanisms of generation of prestress in wood and motion in the seed dispersal units, Fratzl *et al.* provided a simple mechanical model of the cell wall that relates the MFA and matrix swelling to its ability to generate either compressive or tensile stresses and strains [44]. As can be seen from Figure 2-1, when no axial deformation is possible, the cell produces a tensile stress (cell pulls) in an intermediate range of MFA. If the MFA is larger than  $45^\circ$ , the stress is always compressive. This situation envisages adaptations occurring in conifers to bear the increased weight of growing branches. It is observed that contracting cells (MFA= $12^\circ$ - $25^\circ$ , [43, 44]) are produced on the upper side of the branch and compressive ones on the lower side (MFA= $52^\circ$ ). Cell contraction can also be enhanced. This strategy is found in the tension wood of hardwood plants like poplar [45] and contracting roots of red clover [46]. Here a supplementary inner layer (G-layer) lines the cell walls internally. This G-layer consists

## 2. Basic Concepts

of highly crystalline cellulose fibres oriented axially ( $MFA=0^\circ$ ) accompanied by some xyloglucan. The complete absence of lignin makes this layer highly swellable. This layer swells laterally (since axial expansion is impeded by the stiff cellulose microfibrils), and creates an internal pressure on the cell walls. The pressure produces an additional hoop stress in the cell wall, which is translated to even larger longitudinal contractile stresses by the mechanism explained earlier [14].

In the other limiting case where the cell is free to deform longitudinally, the model predicts shrinking for intermediate MFA and expansions for MFA larger than  $45^\circ$ . The case of randomly oriented microfibrils produces compressive stress or expansion strains. Cell wall actuation is complex as both tensile and compressive behaviours can be achieved, and their value depends non trivially on the microfibril angle.

It is also noted that this mechanism works similarly to a lever arm, producing either high stresses or high strains. Zero longitudinal strains correspond to a maximum stress scenario; conversely, a zero stress condition individuates the case of maximum strain that can be developed. These two situations embody the physical bounds in which the system operates, any real scenario falling between these two limit cases. In absolute terms, the highest possible stresses are tensile, while the highest strains are extensional.

Examples of plant actuators working at low stresses (

Figure 2-2) can be found among many seed dispersal units, where, due to the small size of the organs, generation of big forces is not needed. The most well known example of them is the pine cone [1, 8, 47].

Upon drying, pine cones open due to a bending movement of their scales. In these scales, differently structured tissue layers on the upper and lower sides can be distinguished. In the upper side of the scales, the cell walls exhibit a MFA close to  $0^\circ$ , which translates in minor deformation in the axial direction upon drying. On the scales' lower side, cellulose microfibrils are oriented almost perpendicular to the cell axis, which makes these cells prone to strong longitudinal contraction upon drying. The combined action of both strongly connected tissue layers leads to a bending of the scale, which opens the cone [8].

## 2. Basic Concepts

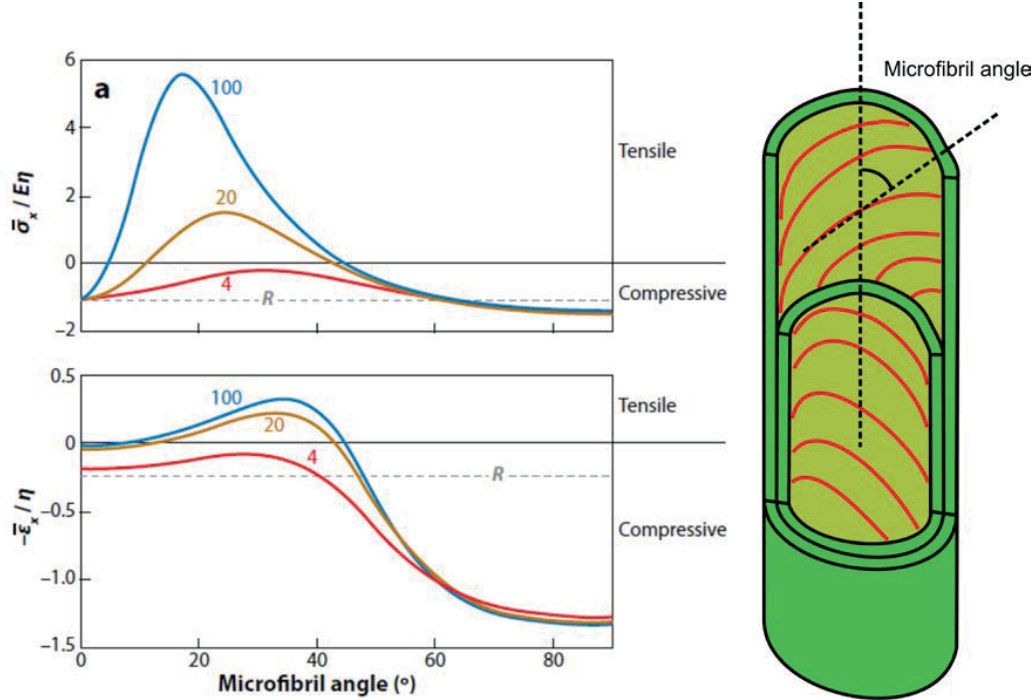


**Figure 2-1 Cell wall actuation through microfibril angle.**

A simple mechanical model ([44]) can describe the ability of plants cell wall to generate either compressive or tensile stresses/strains depending on the fibres orientation. The relative stress and strain are reported with respect to the matrix Young modulus  $E$  and isotropic swelling expansion  $\eta$ . The stiff cellulose fibres are wound at a variable microfibril angle (MFA) in the cell wall (right) and direct the isotropic swelling. Maximum stresses are created when cell is axially constrained (left upper panel) whereas maximum strains happen in case of free axial swelling (left lower panel). Depending on the average microfibril angle, either compressive or tensile stresses and strains can be generated. A high fibres-to-matrix stiffness ratio  $f$  maximizes the mechanism of stress/strain generation (in plant cell walls  $f \approx 20$  [36]). The model predicts high tensile stresses for  $MFA \approx 25^\circ$  and compression stresses for  $MFA > 45^\circ$ . These values are similar to the ones found respectively in cells from the upper and lower part of conifer branches, and serve to bear the increased load of the growing branch. Large deformations are predicted for MFA of almost  $90^\circ$ , which is found in the pine cone scales to achieve large deformations. The dashed line corresponds to random cellulose fibres orientation, which is found in the seed dispersal unit of wild wheat, where large stresses aren't needed. (Reprinted with permission from [14]).

A similar system can be found in the seed dispersal unit of the wild wheat [48, 49]. It consists of two awns attached to seed. They are elongated structures with an internal portion (the cap) connected to an external one (the ridge) in a bilayer fashion. In the cap, the cellulose fibrils in the cell walls are aligned with the awn axis, so that it doesn't respond to a humidity change; in the lower portion of the ridge instead, the cells exhibit a random distribution of microfibril angle which results in isotropic shrinkage upon drying (see dashed line R in Figure 2-1). During the day the awns bend outwards, while in the

## 2. Basic Concepts

humidity at night they move towards each other. The presence of barb-like silica hairs on the awns' surface ensures that this opening-closing movement translates in an effective locomotion when the seed dispersal unit lies on the ground.

In both systems, similarly to a bimetal strip subjected to a temperature increase [50], bending results from incompatible elongation of the two layers. Each system though is tuned to accomplish slightly different tasks. The pine cone scales enclose the seeds until the cone dries out. As the scales are thick and short, larger stresses are needed to bend the scales. Here the highest possible contrast in longitudinal strain is achieved by a parallel orientation in the upper layer and almost perpendicular orientation in the lower one. Wheat awns instead serve for locomotion, and given the low weight of the seed to be moved, big forces are not needed. Indeed, a smaller difference in strains is implemented only in the portion proximal to the seed; then, the long, slender distal portions geometrically amplify the bending deformations, and maximize the displacement at the tip. Pine cone scales and wild wheat awns represent the class of bending bilayers, but more complex movements can be achieved.

Indeed, as in the *Bauhinia* seed pods [51], coiling deformations upon drying can result when a flat elongated strip is cut from a bilayer sheet with perpendicular fibres. The deformed shape can vary from a helicoid (where the strip twists around its main axis) to a ribbon (where the strip has the shape of a cylindrical envelope). When the strip main axis is at  $\pm 45^\circ$  to the fibres orientation, the bilayer tries to bend at perpendicular directions [52] which leads to mechanical frustration. If the strip is narrow, the two bending processes are balanced and the strip twists along the mid-line (with a local saddle shape). If the strip is wide, the saddle deformation is energetically non favoured and the strips adopts a ribbon shape (one curvature vanishes). These competing processes lead to a continuous transition between the two shapes [51].

Interestingly, when the strip mid-line is inclined at angles other than  $\pm 45^\circ$  to the fibres, several coiled shapes can result. Therefore, the bilayer bending is simply a special case (mid-line at  $0^\circ$  and  $90^\circ$  to the fibres) of a more general phenomenon.

Ribbons are also obtained when thin monolayer strips of fibre reinforced elastomer are swollen [53]. As the in plane expansion of the swelling portions is prevented by the stiff fibres, the strip buckles out of plane and a single principal curvature appears along the



## 2. Basic Concepts

fibres' direction. Since the strip midline is inclined with respect to the fibres, a cylindrical coiling is obtained. In the Stork's bill awn [31, 54] a coiling movement is generated with yet another underlying mechanism. The cells of the awn tissue show a tilted arrangement of the cellulose microfibrils. Upon drying, each longitudinal segment of the cell bends and twists locally, resulting in cells that spontaneously coil. Since the cells are elongated and aligned with the awn longitudinal axis, this motion is collectively transferred to the whole awn.

To summarize, actuation based on fibre-reinforced cells is generated at the level of the cell wall and can be tuned for creating either stresses or strains that can be both compressive and tensional depending on the microfibril angle. This mechanism can be enhanced by adding a swellable internal layer that pressurizes the cells. Stresses and strains are exerted axially to the cell wall and translate unchanged at the level of the tissue (affine strains between cells and tissue). Movements are generated by juxtaposing tissues with contrasting swelling properties. In bilayers, bending results as a way to release internal stresses due to differential expansion. More complex movements like twisting and coiling are generated if the mechanisms of stress release are in competition: in this case the type of movement will depend on the object's geometry.

## 2. Basic Concepts

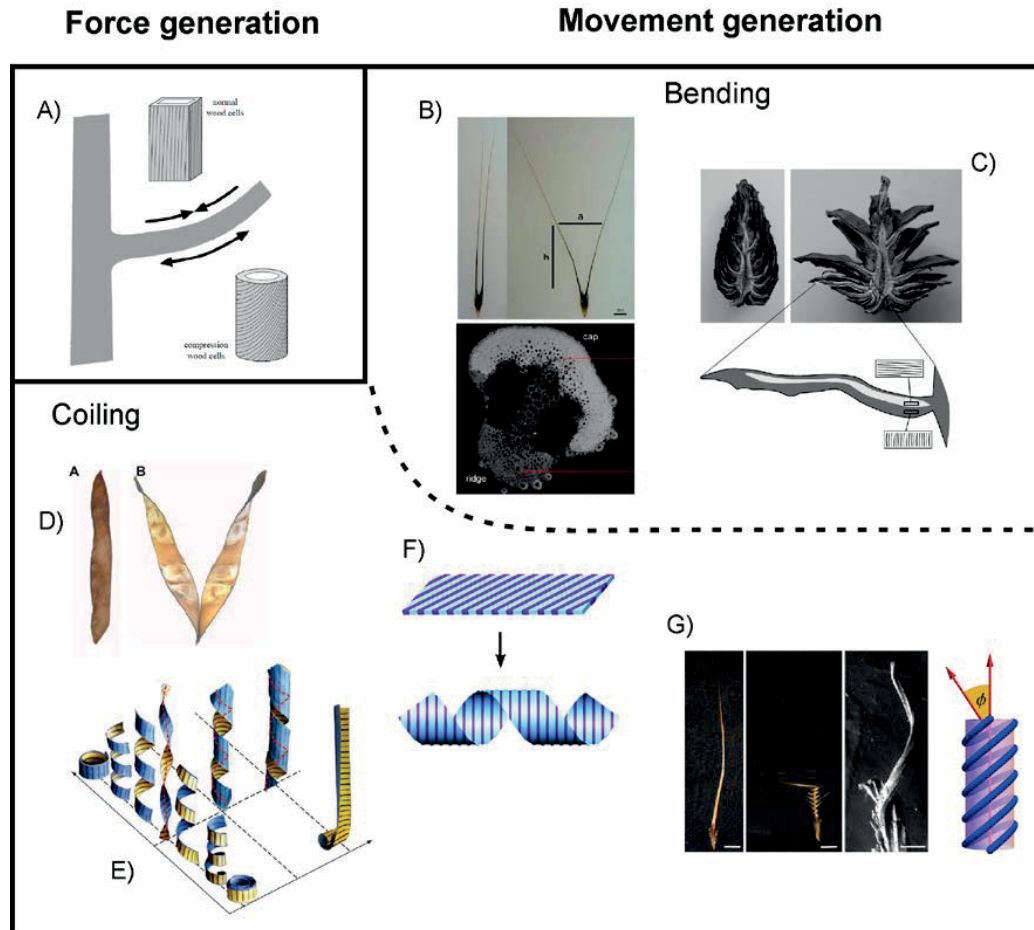


**Figure 2-2 Examples of actuating systems based on fibres reinforced materials.**

Simple actuating plant and artificial systems based on stiff fibres embedded in swellable matrix “designed” to generate forces or movements. Force generation: A) in conifers, late local deposition of tension wood and compression wood on respectively upper side and lower side of the branch to counteract gravity (Reprinted with permission from [8]). Movement generation: B and C) Bending movements in response to humidity changes in wild wheat awns and pine cone scales result from their bilayered structure with different axial hygroscopic coefficients (Reprinted with permission from [49] and [8]). Coiling movements can result from several mechanisms. D) Each valve of the Bauhinia seed pods, is made of two layers of tissue with fibres oriented at  $\pm 45^\circ$  to the pod main axis; double bending along perpendicular axes results in valve twisting (Reprinted with permission from [51]). E) Perpendicular fibres arrangement in a bilayered strip can also result in ribbons, for larger strip widths (Reprinted with permission from [52]). F) A monolayer strip made of alternating stiff non-swellable and soft swellable fibres buckles out of its plane upon swelling; a single principal curvature appears along the fibres’ direction and the flat strip morphs into a ribbon as the fibres are inclined with respect to the strip midline (Reprinted with permission from [53]). G) In the Stork’s bill awn each cell possesses a peculiar tilted arrangement of cellulose microfibrils; the cells bend and twist locally, resulting in a collective coiling of the awn (Reprinted with permission from [54]. Copyright 2012 by The American Physical Society).

### ***2.1.2 Constrained swelling in a closed cellular structure***

Nature provides more examples of actuating systems based on tissue architectures that reach beyond the class of fibre reinforced composite materials, as in the case of the *Delosperma nakurense* (ice plant) seed capsule [16].

The seed capsule contains five seed chambers, separated by septa (Figure 2-3). In the dry state, five valves close the chambers to prevent accidental seed dispersion, with the centre of each valve pushed against a corresponding septum. As liquid water comes into the tissues, the valves unfold, moving away from the septa, spanning an angular trajectory of about 150°. The specialized organ promoting this movement is the hygroscopic keel, a prominent tissue attached to the centre of the inner valve surface, consisting of two halves which, in the dry state, pack onto the septum [16]. The keels are attached to a thin, sclerotized tissue which doesn't experience significant expansion upon hydration, to form a bilayer. At a macroscopic scale the keels consist of a highly anisotropic honeycomb structure, with lignified walls enclosing a cellulosic inner layer (CIL). At a lower scale, the CIL exhibits alternating sheets of dense cellulosic fibres parallel to the cell walls joined by a loose, interconnected network of cellulose fibrils [17], with a structure similar to some engineering superporous hydrogels [55]. Relative humidity even up to about 90% did not induce any deformation of the keels, which start to bend only when wetted by liquid water [17].

Given the high porosity and water affinity of the CIL tissue, significant swelling occurs when liquid water is absorbed. Similarly to the hardwood tension wood, the cell walls act as a constraint for the CIL free swelling. But differently from it, the cells undergo an in-plane deformation, directing the expansion along the cells short axis, where the honeycomb is softer. As a result the tissue deforms up to four times in the cells' short axis direction, while maintaining its original dimension in the other. As the keel is joined to the non swelling backing tissue, a huge bending motion is generated that enables valve opening. Moreover, in the open state the valves curvature is localized in a small portion which works as a hinge [16].

In this system, design concepts present in other passive plant actuators are implemented to accomplish different tasks. Firstly, the constrained high swelling of the CIL material is

## 2. Basic Concepts

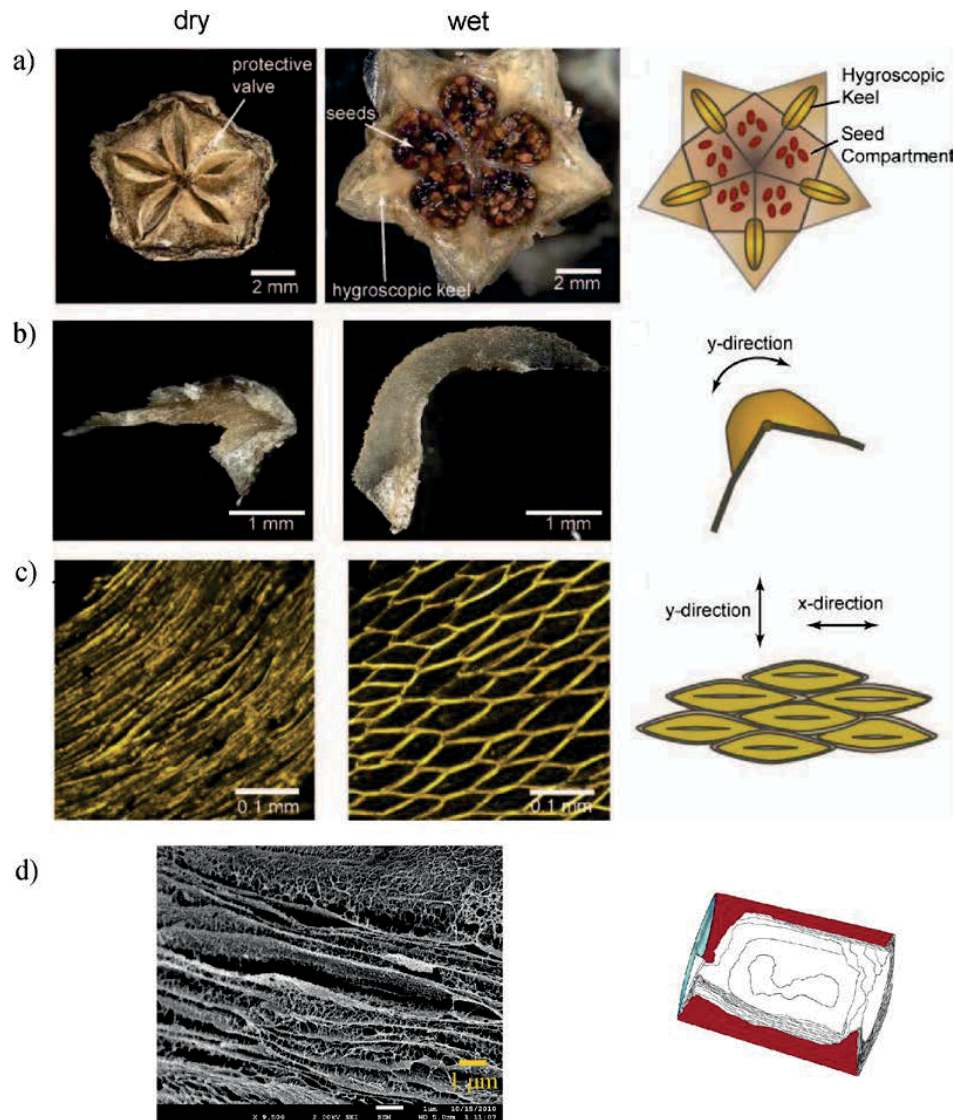


**Figure 2-3 Ice plant seed capsule unfolding is based on constrained swelling in closed cellular space.**

The unfolding of the ice plant seed capsule is an orchestrated movement relying on many levels of hierarchy; still it is powered by the swelling of a cellulosic inner layer found in the cells of the keels. *a)* The seed capsule is composed of five seed chambers, which in the dry state are tightly closed by valves and open up upon swelling. *b)* A specialized tissue (keels) forms with the valve a bilayer that bends around a "hinge" portion. *c)* The keels tissue is composed by highly anisotropic cells with lignified walls lined by a hygroscopic cellulosic inner layer (CIL). In the dry state these cells are compacted together, but expand up to four times along their short axis (y-direction) when wetted. *d)* The microstructure of the CIL with its alternating layers of crystalline and hydrogel-like amorphous cellulosic material is believed to contribute to the unidirectional expansion and its specific onset in presence of liquid water. (Reprinted with permission from [16]. Images a-c) courtesy of Dr. Matt Harrington; image d) courtesy of Khashayar Razghandi).

here “used” to maximize cell walls deformations rather than pressures, with the cellular solid architecture resulting in high anisotropic deformation. Secondly, the bilayer bending motion is optimized to obtain strong localized curvature of the valves which is needed for the reversible opening and closing of the seed chambers.

### 2.2 Two dimensional cellular materials

Cellular solids are materials in which a structural part encloses a void closed space. They can occur as three dimensional foams where cells are enclosed by faces, which are surrounded by edges, which are delimited by vertices [24] or as two dimensional solids where the cells are obtained as extrusions of planar faces (in the latter case they are also called honeycombs). Their structure can be regular, with cells having always the same shape (as for bees honeycombs), or irregular as in the case of certain natural materials like cork.

In this section we will provide the theoretical tools to describe the geometry and the mechanical properties of two dimensional cellular materials, which will be referred to later in the manuscript (especially paragraphs 3.1.2 and 4.3).

#### 2.2.1 Shape, size, topology

As we will see later, the geometrical and topological properties of two dimensional cellular materials are strictly influencing their mechanical behaviour, so we now introduce some basic concepts related to simple geometries that can be applied also to more complex cases.

In the simplest case honeycombs are formed by regular polygons that pack together to tessellate the Euclidean plane, leaving no gaps nor overlaps. In a tessellation (from Latin *tessera*: tile) neighbouring polygons share full edges and have coincident vertices. For example structures like the triangular lattice at the bottom of the central column in Figure 2-4 are not a tessellation while all others are. In all tessellations, angles meeting at one vertex sum up to  $2\pi$ . For this reason there are only three regular tessellations: these are based on triangle, square and hexagon (since  $360^\circ/6=60^\circ$ ,  $360^\circ/4=90^\circ$ ,  $360^\circ/3=120^\circ$ . The

## 2. Basic Concepts

same can be said for semi-regular tessellations, which are composed by more than one regular polygon.

In a honeycomb (or planar lattice) there are as many edges as angles meeting at one vertex. By noting that in a lattice each edge connects two vertices one can define the edge connectivity as [56]:

$$Z_e = 2 \frac{E}{V} \quad 2-1$$

A topological rule that goes under the name of Euler's law relates the number of vertices  $V$ , edges  $E$ , cells  $C$ :

$$C - E + V = 1 \quad 2-2$$

From the previous two relations, it can be demonstrated [24] that the average number of sides per cell  $\bar{n}$  is:

$$\bar{n} = \frac{2Z_e}{Z_e - 2} \quad 2-3$$

This rule holds also for irregular honeycombs, or semi-regular honeycombs (as in the Kagome lattice for example). This means that a three-connected honeycomb has, on average, six sides per cell, a four-connected one has four sides per cell and so on.

Honeycombs can be periodic when they show translational symmetry. Regular and semi-regular tessellations are periodic whereas random tessellations, like the Voronoi honeycomb, are non periodic. Nonetheless also non periodic tessellations based on a limited set of repeating polygons are possible, as the famous Penrose tiling.

The number of possible tessellations is infinite when the polygons are non regular, that is anisotropic or non-convex.

A honeycomb is geometrically anisotropic if its base polygon is elongated (like in a rectangular honeycomb), or in case of unequal internal angles (like in a rhombus/diamond). Shape anisotropy can be quantified as:

$$R = \frac{\bar{L}_1}{\bar{L}_2} \quad 2-4$$

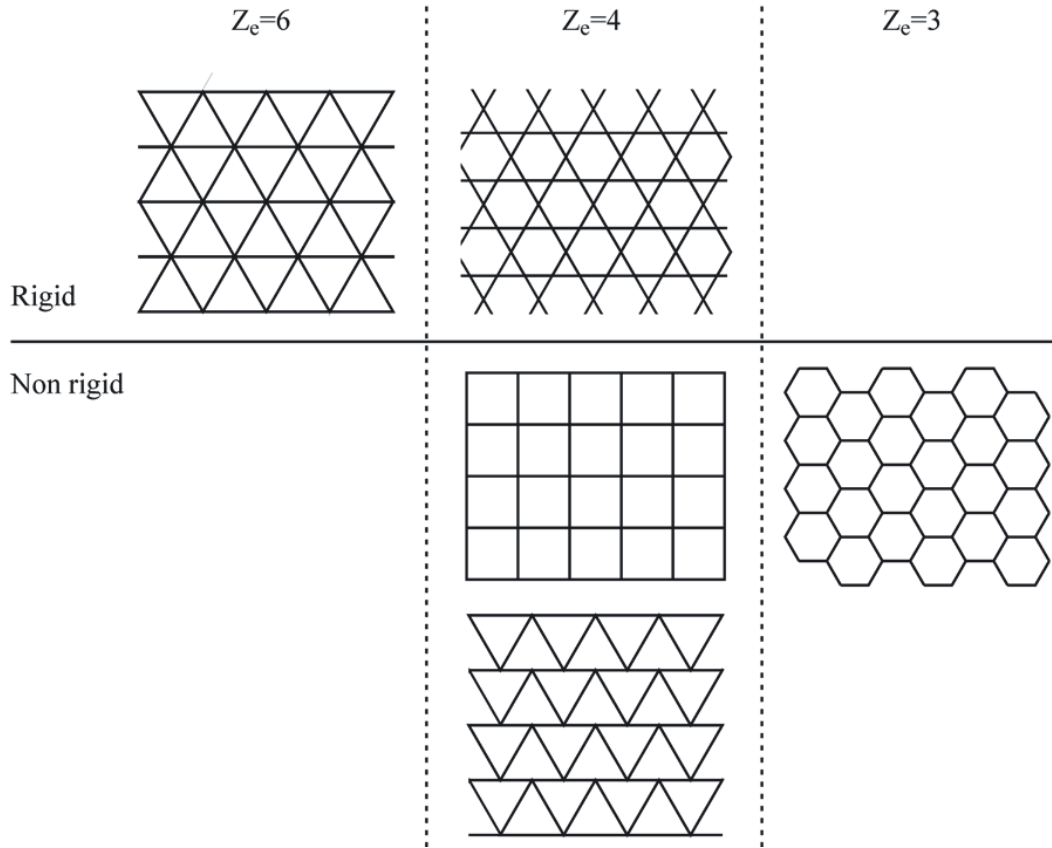


**Figure 2-4 Two dimensional honeycombs and tessellations based on convex polygons.**

The regular triangular, square and hexagonal lattices are also tessellations since they fill the two dimensional space. Strictly speaking the triangular lattice at the bottom of the central column is not a tessellation, since neighbouring polygons don't share same edges and vertexes: in reality this is a degenerate quadrangular lattice. Planar lattices can be grouped in topological classes depending on their connectivity  $Z_e$  –that is, the number of edges meeting in a vertex. Lattices with  $Z_e > 4$  are rigid as any external load results in stretching of the walls. Lattices with  $Z_e < 4$  are non rigid since they deform by bending the walls. The case of  $Z_e = 4$  can show both types of behaviour depending on the presence of periodic mechanisms (as in the square lattice) or their absence (Kagome lattice – first from above).

where  $\bar{L}_1$  and  $\bar{L}_2$  (with  $\bar{L}_1 > \bar{L}_2$ ) are the number of cells per unit length of a straight line lying parallel to each of the two honeycomb principal directions.

Cell convexity can be measured as the ratio between the area of the polygon and the square of its perimeter, multiplied by  $4\pi$ :



## 2. Basic Concepts

$$C = \frac{4\pi A}{p^2} \quad 2-5$$

This parameter takes a maximum value of one in the case of the circle, and a minimum value of zero for a degenerate polygon with zero internal angles. For regular polygons, convexity is directly proportional to the number of sides. Re-entrant honeycombs [57], are based on non-convex cells (which have internal angles larger than  $\pi$ ) and show negative values of Poisson's ratio.

### 2.2.2 *Honeycomb mechanics*

Due to their abundance both in nature and in engineering applications, honeycombs' mechanics has been studied in a number of different aspects, like linear elasticity, buckling, failure mechanisms, and the influence of specimen size, cell shape variability and defects on these [24, 25, 27, 28, 58-67].

Both experiments and theory show that the mechanical properties of a honeycomb depend on their density. This is defined in relative terms with respect to the density of the material of the walls. For periodic two-dimensional cellular materials the density derives from the geometry of the lattice and is proportional to the aspect ratio of its edges, which is the ratio between the edge thickness  $t$  and length  $l$ :

$$\frac{\rho}{\rho_s} = k \frac{t}{l} \quad 2-6$$

where  $k$  is a constant that depends on the geometry of the cell.

Assuming small strains and standard beam theory, Gibson and Ashby [24, 68] calculated the in-plane elastic properties of a hexagonal honeycomb by looking at the deformation of the walls under an external load. They showed that the mechanical response of a hexagonal honeycomb is dominated by the bending rigidity of its walls, which is proportional to the cube of  $t/l$ :



$$\frac{E_1}{E_s} = \left(\frac{t}{l}\right)^3 \frac{\cos \alpha}{(h/l + \sin \alpha) \sin^2 \alpha} \quad 2-7$$

$$\frac{E_2}{E_s} = \left(\frac{t}{l}\right)^3 \frac{(h/l + \sin \alpha)}{\cos^3 \alpha}$$

The same formulas can be applied to four connected honeycombs (like square and diamond shaped honeycombs) if we consider the vertical member  $h$  vanishing. But when the load is aligned with the walls, then the structure resists by axial extension or compression of the walls so that the effective modulus is proportional to  $t/l$ :

$$\frac{E_1}{E_s} = \frac{E_2}{E_s} = \frac{t}{l} \quad 2-8$$

In triangular lattices the microscopic deformation involves always wall stretching or compression, regardless of the loading direction. Hence the in plane elastic properties are isotropic and scale again with  $t/l$ :

$$\frac{E_1}{E_s} = \frac{E_2}{E_s} = 1.15 \frac{t}{l} \quad 2-9$$

Equations 2-7 to 2-9 show that the apparent stiffness of triangular honeycomb is intrinsically higher than that of a hexagonal one: the former scales with the first power of density whereas the latter scales with its cube. This difference depends, as we have seen, on how the honeycomb microstructure responds to a macroscopic load, namely with a bending dominated or a stretching dominated behaviour.

Maxwell [56] suggested a criterion setting out the necessary condition for a planar pin-jointed frame of  $b$  struts and  $j$  frictionless joints to be rigid:

$$b = 2j - 3 \quad 2-10$$

If the frame has more struts, it will be overconstrained, whereas if they are less, the frame will behave as a mechanism. Applying this criterion to planar lattices, Fleck showed that [56, 69], a connectivity  $Z_e=6$  (triangular lattice) is sufficient to make the lattice rigid (or stretching dominated). With  $Z_e < 4$  ( $Z_e=3$  in a hexagonal honeycomb) any macroscopic deformation will cause the honeycomb's wall to bend, so that the lattice response is not rigid. The case of  $Z_e=4$  is at the boundary and includes non rigid, bending dominated structures when there are periodic mechanisms arising in the lattice (in a square lattice for

## 2. Basic Concepts

instance a shear deformation will cause a periodic shearing of each cell) or stretching dominated ones (as in the Kagome lattice – see Figure 2-4): these conditions clearly set a relationship between lattice topology (see equation 2-1) and its mechanical behaviour.

It has to be mentioned that all former considerations apply for small deformations and the Gibson-Ashby prediction typically fail to predict the honeycomb mechanical properties when the strain range becomes consistent ( $\epsilon > 10\%$ ). This can happen because of material non linearities (creep for polymers; plasticity in the case of metals; brittle fracture in case of ceramics and glasses), loading non linearities such as elastic buckling caused by compressive loads on the honeycomb walls, or because at high deformations, there is a strong distortion of the honeycomb geometry, and the walls tend to align with the load direction, stiffening the response.

Warren and Kraynik also developed a linear elasticity theory for predicting the in-plane properties of hexagonal lattices [27]. They also provided explicit formulas which don't restrict to cell walls of uniform thickness. Later they also developed a non linear elastic theory [28] on the assumptions that microscopic mechanisms entail the possibility of walls stretching and rotating. They showed that the effect of finite strains becomes relevant for strains larger than 10%; in particular, shear stress has cubic components dominated by cell walls stretching, while uniaxial stress is dependent on their bending rigidity and is asymmetric (different behaviour in compression and tension).

### ***2.2.3 Estimation of cellular materials properties by numerical homogenization***

In the former paragraph we have seen that the mechanical properties of honeycombs can be easily predicted, under certain assumption, by knowing their geometry. The microstructure of real cellular materials instead is not always so regular and other approaches that go under the name of homogenization methods have been proposed.

The underlying assumption of homogenization methods is that the effective properties of a heterogeneous material (materials with more than one phase) can be estimated from the knowledge of the constitutive laws and spatial distributions of their components [70].

## 2. Basic Concepts

A major difference has to be made between analytical and numerical homogenization. In analytical methods, the heterogeneous material is considered as a random infinite system where its properties are given in a statistical fashion (for example: volume fraction of the phases, aspect ratio and orientation of inclusions); the more statistical information is known about these, the finer the properties' estimation will be. Numerical methods instead consider a real finite sample of material (a microstate) and derive the effective properties of the material by means of finite element simulations (an introduction to the finite element method is given in paragraph 3.1.1). This is entailed in the concept of Representative Volume Element, which is a necessary condition for the application of numerical homogenization. The RVE is usually regarded as a volume  $V$  of heterogeneous material that is sufficiently large to be statistically representative of the composite. It means that the effective properties are calculated as a spatial average. Another possibility is to use a set of volumes smaller than the RVE and estimate the effective properties by taking their ensemble average (an ergodicity property is granted [71]).

If the existence of an RVE is still a matter of debate [72], it is obvious that for ideal cellular materials like the ones we will consider later, an RVE exists since these materials are periodic.

In the following we will introduce the basic theoretical notions needed to understand the numerical homogenization of the elastic mechanical properties of a heterogeneous material.

In the simplifying hypothesis of a heterogeneous material with linear elastic phases, the mechanical state of the material at any point  $\mathbf{x}$  is described by the local stress-strain relationship:

$$\tilde{\boldsymbol{\sigma}}(\mathbf{x}) = \tilde{\mathbf{c}}(\mathbf{x}) : \tilde{\boldsymbol{\varepsilon}}(\mathbf{x}) \quad 2-11$$

Considering a RVE of volume  $V$ , we define the global stress and strain as the spatial averages on the RVE of their local counterparts:

$$\begin{aligned} \tilde{\boldsymbol{\Sigma}} &= \frac{1}{V} \int \tilde{\boldsymbol{\sigma}} dV = \langle \tilde{\boldsymbol{\sigma}} \rangle \\ \tilde{\mathbf{E}} &= \frac{1}{V} \int \tilde{\boldsymbol{\varepsilon}} dV = \langle \tilde{\boldsymbol{\varepsilon}} \rangle \end{aligned} \quad 2-12$$

Then the effective (homogenized) mechanical properties  $\tilde{\mathbf{C}}_{eff}$  are found as [73, 74]:

## 2. Basic Concepts

$$\tilde{\mathbf{C}}_{eff} = \tilde{\mathbf{E}}^{-1} : \tilde{\mathbf{\Sigma}} \quad 2-13$$

Operationally the problem reduces to the calculation of the global stress  $\tilde{\mathbf{\Sigma}}$  due to an imposed global strain  $\tilde{\mathbf{E}}$ . This can be done by means of a FE simulation. Since the volume of material is in equilibrium, the sum of the volume forces equals the sum of the surface forces, so that the global quantities can also be defined as:

$$\tilde{\mathbf{\Sigma}} = \frac{1}{\partial V} \int \tilde{\mathbf{\sigma}} \cdot \mathbf{n} \, dS \quad 2-14$$

Obviously, the effective value of  $\tilde{\mathbf{\Sigma}}$  and hence of  $\tilde{\mathbf{C}}_{eff}$  will depend on the choice of the global strain to be applied. Regarding the global strain, there are three possible choices to apply a mean strain. In the case of kinematic uniform boundary conditions the strain on the volume is imposed by displacing its boundaries by a constant value  $\mathbf{u}$ :

$$\mathbf{u} = \tilde{\mathbf{E}} \cdot \mathbf{x} \quad \forall \mathbf{x} \in \partial V \quad 2-15$$

In the case of stress uniform boundary conditions, the boundaries are displaced such that the traction  $\mathbf{t} = \tilde{\mathbf{\sigma}} \cdot \mathbf{n}$  is constant throughout the boundary. In the case of periodic boundary conditions, the boundaries are displaced by a value which is the sum of an average strain plus a periodic fluctuation  $\mathbf{v}$ :

$$\mathbf{u} = \tilde{\mathbf{E}} \cdot \mathbf{x} + \mathbf{v} \quad 2-16$$

It has been shown [70, 73] that kinematic uniform BC tend to underestimate the effective stiffness whereas stress uniform BC overestimate it, regardless of the size of the RVE chosen. Given the intrinsic periodicity of the materials we will deal with, the natural choice is to assume periodic boundary conditions. Indeed, it is known that in this case the homogenization problem gives exact results [75].

### 2.3 Volumetric changes by fluid sorption

As seen in chapters 2.1-3 passive natural actuators rely on sorption as a source of volumetric strain needed to perform complex actuation.

Depending on the location at which sorption takes place, one can distinguish between surface-based phenomena (adsorption, desorption) and bulk-based phenomena (swelling).

In the first category, a free phase (adsorbate) interacts with a solid “dense” material (adsorbent) without diffusing in it. This phenomenon is very relevant for materials with high surface-to-volume ratio and accessible porosity. The second category considers all those systems where the free phase can diffuse inside the substrate.

Materials that make up biological actuators will in general be subjected to both phenomena, being at the same time porous and based on materials permeable to water.

### *2.3.1 Statistical treatment of swelling*

When a soft, polymeric material is swollen, its molecular network gets stretched. Hence, studying swelling of polymers, is analogous to study the problem of their elasticity. In the following we will introduce the basics of elasticity and swelling theory of cross-linked elastomers in its statistical treatment, as proposed by Kuhn, Flory-Rhener and Treloar starting from the 30's [76-78].

Consider a polymer as a collection of long chains cross-linked together. Each chain is formed by a number of freely rotating links. In their natural state the chains are random coils (the distance between cross links –or end-to-end distance- is sensitively smaller than the chains' extended length) that interact with each other by low energy interactions. Fixing one end of the chain, the probability of finding the other end at a given distance  $r$  is given by the Gaussian error function [78] (which is an exponential form of the square of the end-to-end distance). Now, since the entropy of a system is proportional to the logarithm of the number of total configurations available [76], the entropy of the chain is proportional to the square of the end to end distance. Under certain assumptions (polymer incompressibility, affinity of deformations between macroscopic polymer and chains), this result can be extrapolated to a network of cross-linked chains. Imposing a deformation to the network will limit the number of available configurations of the chains, decreasing their entropy. At the same time the number of lateral interactions doesn't change, since old bonds are replaced by new ones, that is, the change in internal energy is zero. Hence the work of deformation on the network equals the change in entropic energy and is given by:

## 2. Basic Concepts

$$W_e = \frac{1}{2} N k_B T (\lambda_1^2 + \lambda_2^2 + \lambda_3^2 - 3) \quad 2-17$$

Where the subscript “e” stands for elastic,  $N$  is the number of chains per unit volume,  $k_B$  is the Boltzmann constant,  $T$  is the temperature, and  $\lambda_i$  are the extension ratios along three Cartesian coordinates. It is useful to put:

$$G = N k_B T \quad 2-18$$

which represents the shear modulus.

The 2-17 is called the strain energy function and describes the mechanical behaviour of a cross-linked rubber-like material such as an elastomer. The stress-strain relationships are calculated by differentiation, given appropriate mechanical boundary conditions (compatible with the incompressibility condition:  $\lambda_1 \lambda_2 \lambda_3 = 1$ ).

When swelling occurs, fluid molecules migrate from the pure liquid to the polymer creating a mixed phase. When the mixture is in equilibrium with the pure liquid (or saturated vapour:  $p=p_0$ ), the change in the Gibbs free energy of dilution upon further swelling (i.e. the partial molar free energy of dilution – at fixed number of solute molecules) is zero. This is written as:

$$\frac{\partial \Delta G}{\partial n} = \frac{\partial \Delta H}{\partial n} - T \frac{\partial \Delta S}{\partial n} = RT \ln\left(\frac{p}{p_0}\right) = 0 \quad 2-19$$

where  $\Delta H$  is the partial molar enthalpy of dilution and  $\Delta S$  is the partial molar entropy of dilution.

From the statistical standpoint, swelling corresponds to an increase of entropy, since when the chains are more diluted, the number of sites available for each chain's segment increases. When the polymer is cross linked, the swelling process will take place until the network itself undergoes mechanical stretching, otherwise it will continue indefinitely. Nonetheless swelling is not entirely an entropic phenomenon, as can be assumed from the previous relation. Fluid molecules that enter the mixed phase will interact with the polymer chains. The strength of these interactions depends on the chemical nature of solvent and polymer; and can be actually stronger than the entropic contribution and become the main driving force for swelling. The latter is usually the case of mixtures of water and hydrophilic polymers like cellulose. Still, an entropic description of swelling in

## 2. Basic Concepts

these systems can still be appropriate at large dilutions, when all the sites for lateral polymer-fluid interactions are already occupied, and newly added fluid molecules can only interact with other “liquid” molecules.

Here we report the classical result by Flory and Huggins [77] for the partial molar free energy of dilution of a non cross-linked polymer by considering a statistical derivation of the entropy contribution (the complete treatment can be found in [76]) as a function of the polymer volume fraction  $v_2$  in the mixture:

$$\frac{\partial \Delta G}{\partial n} = RT (\ln(1 - v_2) + v_2 + \chi v_2^2) \quad 2-20$$

where the first two terms in the parenthesis represent the entropic contribution and the quadratic term represents the enthalpic contribution, with  $\chi$  depending on the chemical affinity between liquid and polymer. The polymer volume fraction  $v_2$  in the mixed phase corresponds to a uniform linear extension  $\lambda_0$  in the swollen state:

$$v_2 = \lambda_1^{-1} \lambda_2^{-1} \lambda_3^{-1} = \lambda_0^{-3} \quad 2-21$$

As expected, the equilibrium swelling is reached for infinite dilution of the polymer ( $v_2=0$ ). In case of cross linking, one has to consider also the contribution due to the entropic elasticity of the network (eq. 2-17). At equilibrium the change in free energy of dilution (eq. 2-20) equals the derivative of the elastic work of deformation (eq. 2-17), with respect to  $n$ , so that:

$$\frac{\partial \Delta G}{\partial n} = RT \left( \ln(1 - v_2) + v_2 + \chi v_2^2 + \frac{G}{\frac{RT}{V_f}} v_2^{1/3} \right) \quad 2-22$$

where  $G$  in the last term is the polymer shear modulus in the dry state and  $V_f$  is the molar volume of the fluid: again, given its entropic nature, the contribution due to network elasticity doesn't depend on any chemical properties.

In this case, the equilibrium strain is found for the value of  $v_2$  that satisfies  $\frac{\partial \Delta G}{\partial n} = 0$ .

In the former two cases we described the equilibrium of the network with an external mechanical solicitation or an external liquid phase (free swelling). In the examples of

## 2. Basic Concepts

swelling driven actuation described earlier in this chapter, these two “modes” merge: the material’s swelling is always *constrained*, either by stiff fibres or by a confining cellular structure.

In this most general case, the polymer volume fraction at equilibrium will in general be different than in the free swelling case. Intuitively, stretching a fully swollen polymer along one direction will cause more fluid molecules to enter, so that the polymer will laterally expand. At equilibrium, the polymer volume fraction is smaller than in the free swollen state.

Following the derivation by Treloar [76], this new case can be studied in a combined chemical-mechanical sense, where the chemical free energy of dilution equals an external mechanical work done on the polymer. We consider to apply a (small) probing stress  $\sigma_1$  on a portion of polymer in equilibrium with the pure liquid and constrained to dimensions  $\lambda_1, \lambda_2, \lambda_3$ . Under condition of constant temperature and pressure, the work done by  $\sigma_1$  corresponds to an incremental change in the Gibbs free energy:

$$\delta \Delta G = \delta \Delta W = \sigma_1 l_2 l_3 \delta l_1 = \sigma_1 V_f \delta n_f \quad 2-23$$

Here the rightmost member follows from the hypothesis of volume additivity of polymer and fluid and  $n_f$  is the number of fluid molecules entering the polymer.

The former equation can be put in its differential form to give an explicit relation for the stress  $\sigma_1$ :

$$\sigma_1 = \frac{1}{V_f} \left( \frac{\partial \Delta G}{\partial n_f} \right)_{l_2 l_3} \quad 2-24$$

Where,  $\Delta G$  is the total change of the Gibbs free energy due to the mixing and the elastic contributions (eq. 2-22). Calculating the derivative one obtains the final result:

$$\sigma_1 = \frac{RT}{V_f} \left( \ln(1 - v_2) + v_2 + \chi v_2^2 + \frac{G}{RT} v_2 \lambda_1^2 \right) \quad 2-25$$

Analogous equations apply for the other stresses  $\sigma_2, \sigma_3$ ; altogether these three equations express the chemo-mechanical equilibrium of the polymer immersed in pure solvent and subjected to mechanical boundary conditions along the principal directions 1,2,3. Any



combination of three mechanical boundary conditions (among  $\lambda_1, \lambda_2, \lambda_3, \sigma_1, \sigma_2, \sigma_3$ ), corresponds to a specific equilibrium. In this general case the swollen polymer behaves as a compressible solid, since a volumetric strain will be accommodated by a corresponding fluid sorption.

### 2.3.2 Adsorption

When a molecular fluid is adsorbed on a solid surface, there is a transition from a single 3D gas phase to a 2D adsorbed film [79]. Experimentally, adsorption is investigated by measuring an adsorption isotherm, that is the amount of adsorbate (at constant temperature) in a range of gas partial pressures, when the system is at equilibrium. The shape of these isotherms is characteristic of the fluid-solid system and has been classified in the IUPAC classification (see Figure 2-5). Many phenomenological models are able to capture these isotherms but this doesn't mean that they are reproducing all other measurable quantities. Generally speaking, at low partial pressures, some gas molecules absorb on the solid. As the partial pressure increases, more molecules absorb to create a film of fluid molecules in a multilayer fashion. Depending on the kind of substrate and fluid, other phenomena can happen, such as capillary condensation. For instance, type I is typical for monolayer formation, type II corresponds to substrates that undergo a multilayered adsorption, type III corresponds to a low fluid-solid attraction. Types IV and V are typical for porous solids, and are marked by the presence of discontinuities in adsorbate concentration and hysteresis. At this discontinuity points the fluid film on the pore walls is no longer stable, and collapses forming a meniscus, which accelerates liquid phase formation by spontaneous capillary condensation till full saturation. Capillary condensation in porous solids has also a remarkable effect in the generation of substrate strains. Examples in this sense will be provided later in this section, after a basic introduction on thermodynamics of adsorption is provided.

## 2. Basic Concepts

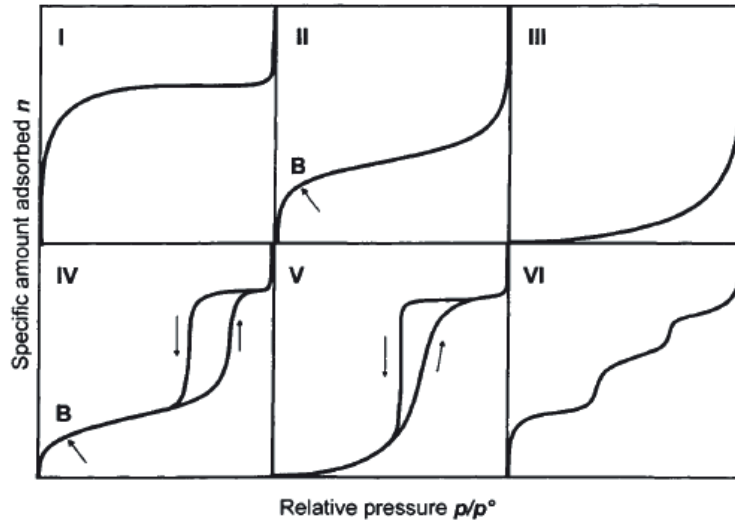


**Figure 2-5 Adsorption isotherms for several types of solids (IUPAC classification).**

Typical adsorption isotherms for: I) Langmuir type or "monolayer" adsorption, also observed in microporous solids ( $r_{\text{pore}} < 2 \text{ nm}$ ); II) multilayer adsorption, with point B indicating the full monolayer coverage; III) adsorption in sorbent-sorbate system with low affinity; IV) typical profile for a mesoporous silicate ( $2 \text{ nm} < r_{\text{pore}} < 50 \text{ nm}$ ) with narrow distribution of porosity: the presence of hysteresis and onset of steep adsorption increase are related to capillary condensation and depend on the capillary radius; V) the hysteresis hints at porous systems (as in IV) but with a weak sorbate-sorbent interaction (as in III); VI) staggered adsorption arises from multiple phase transitions between one adsorbed layer and the other. (Reprinted with permission from [79]).

In its simplest form, any adsorbing system has three compartments - the solid (s), the adsorbed phase (f), and the gaseous phase (g). Similarly to swelling, the equilibrium between the two fluid phases is achieved when the variation of a relevant thermodynamic potential is zero. Under constant temperature and pressure conditions, this potential has to include the effect of surface tension, both of the solid and of the gas-adsorbate interface. Surface tension can be defined for the solid (and will depend on the surface geometry – whether flat, cylindrical or spherical). The adsorption of molecules reduces the surface tension of the solid, increasing the extension of the adsorbate film. A *spreading pressure*  $\Pi$  can be defined as the effective pressure that "wets" the solid :

$$\Pi = \gamma^s - \gamma \quad 2-26$$

Where  $\gamma^s$  is the surface tension of the clean solid and  $\gamma$  is the adsorbate surface tension.

Then the relevant thermodynamic potential is the transformed Gibbs energy [79]:

## 2. Basic Concepts

$$\hat{G} = F + pV - \gamma A \quad 2-27$$

Here  $F$  is the Helmholtz potential and  $A$  is the solid surface. At equilibrium  $\Delta\hat{G} = 0$ .

Breaking down this quantity to the single components:

$$\hat{G} = \hat{G}_f + \hat{G}_s + G_g \quad 2-28$$

Where the Gibbs free energy for the gas obviously doesn't include the surface tension term. If the solid is inert, it will not change its surface or volume during adsorption. Then its only contribution to the balance is included in the spreading pressure  $\Pi$  and the equilibrium condition ( $\mu_f = \mu_g$ ) formally involves only fluid and gas:

$$\Delta\hat{G}_f + \Delta G_g = 0 \quad 2-29$$

Where:

$$\hat{G}_f = F^f + \Pi A = n_f \mu_f$$

$$G_g = n_g \mu_g \quad 2-30$$

$$\mu_g = RT \ln \left( \frac{p}{p_0} \right)$$

In case of mesoporous solids (that is solids with a pore radius of 2-50 nm) condensation happens at lower partial pressures than what is observed for the bulk, and is marked by a steep increase in adsorbate concentration (Figure 2-5). When condensation starts, the adsorbed film collapses and forms a liquid phase with a meniscus due to capillarity. Hence, an additional surface tension enters the energy balance of the system. In this case the physicochemical equilibrium between vapour and liquid is given by the Kelvin equation, which relates the relative vapour pressure in the pore (that is, the vapour pressure with respect to the saturation vapour pressure of the bulk) to the mean radius of curvature of the pore or the meniscus:

$$\ln \left( \frac{p}{p_0} \right) = - \frac{2\gamma_{lv} \cos \theta}{r_p} \frac{V_f}{RT} = - \frac{2\gamma_{lv}}{r_m} \frac{V_f}{RT} \quad 2-31$$

and depends on the liquid-vapour surface energy  $\gamma_{lv}$ , the fluid-solid interaction embodied by the contact angle  $\theta$  (for a perfectly wettable adsorbent  $\theta = 0^\circ$ ). Here,  $1/r_m$  is the mean curvature of the meniscus:

## 2. Basic Concepts

$$\frac{1}{r_m} = \frac{1}{2} \left( \frac{1}{r_1} + \frac{1}{r_2} \right) \quad 2-32$$

Considering also and  $t$  is the thickness of the adsorbed film prior to condensation, for a cylindrical pore, in case of perfectly wettable walls, the meniscus is hemispherical ( $r_1 = r_2 = r_m$ ) with a radius [79]:

$$r_m = r_p - t \quad 2-33$$

while for a flat (“slit”) pore the meniscus is hemicylindrical ( $r_2 = \infty$ ) with a mean radius of:

$$r_m = w_p - 2t \quad 2-34$$

where  $w_p$  is the pore width. The Kelvin equation (2-31) can be rearranged to give the Laplace equation:

$$f_s = \frac{RT}{V_f} \ln \left( \frac{p}{p_0} \right) = - \frac{2\gamma_{lv}}{r_m} \quad 2-35$$

Which gives the pressure difference at the interface between the condensed and vapour phases when condensation has started. For pores it is negative and becomes zero when the partial pressure equals the saturation point (that is the pressure at which bulk condensation occurs). Therefore contraction is expected in porous solids undergoing adsorption. Since the Laplace pressure is proportional to the curvature of the meniscus (and therefore the pore too), its magnitude is expected to increase strongly for pores of small size. In a recent study, Gor *et al.* [19, 20] described the adsorption behaviour in cylindrical mesopores both before and after capillary condensation (see Figure 2-6).

Here the theoretical and simulated absolute solvation pressure upon adsorption is shown for two cylindrical pores of different radius (8.2 nm left; 4 nm right), together with the corresponding adsorption isotherms.

Focusing only on the adsorption branch, two aspects can be noticed. For partial pressures below the capillary condensation the solvation pressure is positive. As said, this is due to the fluid molecules building a film, which decreases the surface tension of the solid (see eq. 2-26) and hence causes a positive mechanical stress on it. When capillary condensation occurs, the solvation pressure decreases abruptly, and increases again for

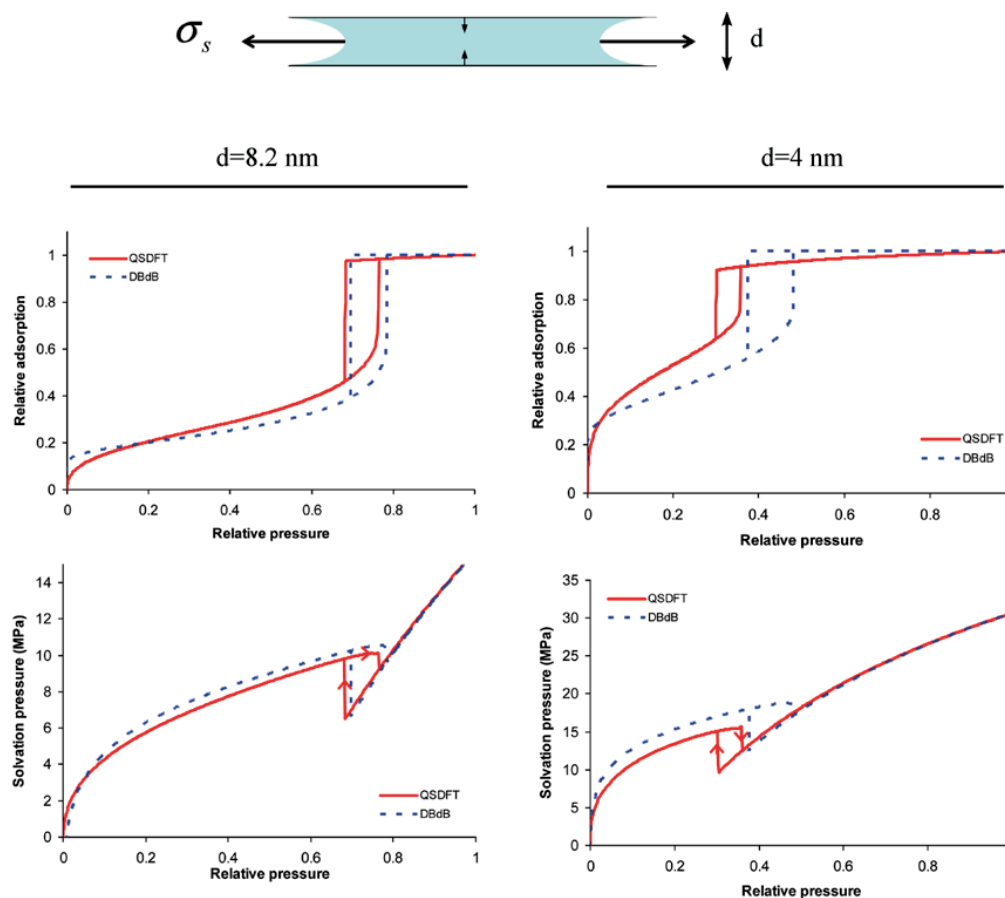


**Figure 2-6** Capillary condensation causes large compression stresses during adsorption in mesoporous solids.

Theoretical (dashed blue lines) and numerical (red solid lines) predictions of adsorption isotherms and solvation pressure for 8.2 nm (left) and 4 nm (right) wide cylindrical pores. The solvation pressure is the difference between the adsorption stress  $\sigma_s$  and the pressure in the bulk, in absolute terms (therefore it is always positive). Condensation of the fluid in the capillary causes a steep increase in adsorbate concentration (upper graphs) and a corresponding fall of on the pore walls (lower graphs). These effects are more pronounced for narrower pores (right). (Reprinted with permission from [20]. Copyright (2011) American Chemical Society).

increasing concentrations of the gas phase, as the Kelvin equation 2-31 predicts. Comparing the curves for the two pores, it can be noticed that the onset of capillary adsorption happens at lower partial pressures for the smaller pore. Also, the slope of the curve is higher, both in the range of film accretion and in the condensed one. In particular the extent of the “fall” in solvation pressure due to capillary condensation is more than double in the smaller pore.

## 2. Basic Concepts

Under these premises, substantial sorption strains are expected to occur when the solid is not infinitely stiff. Experimental evidences of these strains have been reported by Zickler *et al.* [80] by recording adsorption isotherms of SBA-15 mesoporous silicate while detecting in situ synchrotron X-ray diffraction (SAXD), they could observe a marked change in the Bragg peak at the onset of capillary condensation. To better understand the mutual fluid-solid interaction, Schoen and Günther [22] studied the onset of sorption strains in nanoconfinement by means of Monte Carlo simulations. In their model system the adsorption of Lennard-Jones particle in a nanoscopic slit pore with explicit atoms was considered, so that the molecular interaction between solid atoms and fluid particles could be addressed. In particular, pore walls deformations were accounted for, as the solid atoms could depart from their initial position according to a harmonic potential of strength  $\kappa$  representing the stiffness of the walls. Adsorption isotherms were simulated for different values of pore size and the wall stiffness. The dependence of pore strain upon condensation for a moderately soft substrate ( $\kappa = 30$ ) is remarkably similar to the solvation pressure in Gor's results (compare Figure 2-7 a and Figure 2-6). Here too, smaller pores shift the onset of condensation at lower partial pressures (see Figure 2-7 b). A finite wall stiffness instead, causes a shift of capillary condensation at higher values of partial pressure (Figure 2-7 c).

Since the deformation of the substrate is influenced by the magnitude of density changes in the confined fluid [22], these effects could be larger for adsorbing systems in which the fluid is close to a phase transformation.

The theoretical studies cited until now can explain with a high degree of confidence the sorption processes of simple fluids like argon, nitrogen, pentane. The same theories fail to describe the case of a complex fluid like water, which is at the core of our interest, since plants tissues are based on water adsorption at ambient pressure and temperature. Although these conditions are far apart from a phase transformation, it has to be kept in mind that water properties are strongly affected by nanoconfinement [23, 81]. Simulation of water in carbon nanotubes of 1.1 and 7 nm, showed the formation of a water phase in the central core of the pore with properties analogous to that of the bulk phase shifted by +40 °K [23]. Since the hydrophobic confinement results in a diminished density of hydrogen bonds, it was concluded that core water behaves as a higher temperature bulk

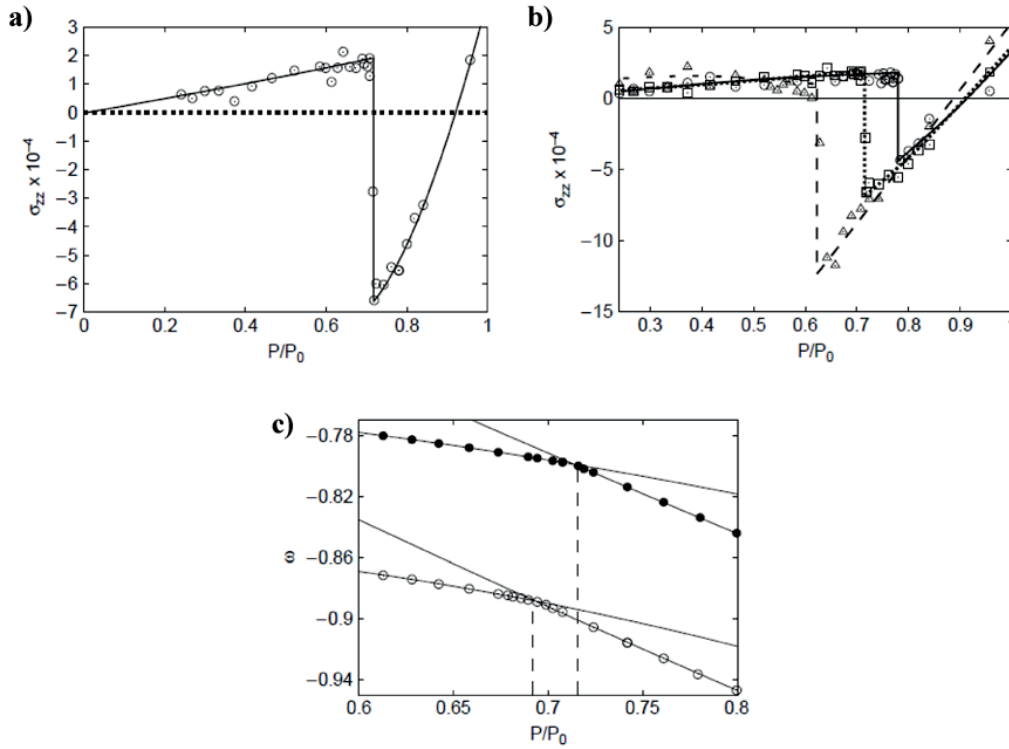


**Figure 2-7 Sorption induced strains in mesoporous solids depend on pore size and solid stiffness.**

The graphs refer to simulated adsorption isotherms in a grand canonical Monte Carlo ensemble considering a slit pore with explicit solid atoms and a Lennard-Jones fluid. a) Adsorption induced contraction of the pore shows the same trend seen for solvation pressure – see Figure 2-6 . b) Pore contractions increase for narrower pores. c) Grand potential density whose slope is function of fluid density. A change in slope individuates a phase change of the fluid. The dashed lines mark the onset of capillary condensation. It is seen that for softer walls ( $\kappa = 30$ ) this point shifts to higher partial pressures than in stiffer walls ( $\kappa = 10^4$ ) (Reprinted with permission from [21]).

water. Experimental studies based on water confined in hydrophilic mesoporous silicas have been conducted by Erko *et al.* [81]. Although they could confirm the presence of two water phases, namely nonfreezable water strongly adsorbed at the pore walls which doesn't form water-water hydrogen bonds, and "core water" which forms a strong HB network, the authors disbelieve that confined water can be assimilated to bulk water. The degree of confinement, regardless of the chemical affinity between walls and water, affects drastically the structure and properties of the core water, even causing a continuous liquid-solid phase transition upon cooling for strong confinement (2 nm), which has no counterpart in the bulk.

In a later study of water adsorption in mesoporous silica powder (porosity of 8.9 nm), Erko *et al.* also demonstrated [82] the occurrence of irreversible adsorption in capillaries,

## 2. Basic Concepts

probably due to generation of exceptional high stresses at this degree of confinement due to high surface tension of water, even exceeding the strength of silica.

Probably the most relevant evidence for the importance of nanoconfined water in plant tissues has been recently provided by Zabler *et al.* [83]. In this study the authors observed that the cellulose nanocrystallites forming the cellulose fibrils in spruce wood cells experience transversal expansions upon dehydration. Since neighbouring nanocrystallites are laterally spaced by few nanometers, the authors suggest that the crystallites expansion might be related to the release of the compressive stresses exerted by water.

Therefore, given that plant tissues are both porous and soft, and that passive plant actuation is based on water sorption, adsorption induced strains in plant tissues could be remarkable. The matter deserves some more attention, and we want to address it with a study on water sorption induced strains due to nanoscopic confinement.



### **3. Materials & Methods**

Since we regarded actuation as a complex mechanical phenomenon we need suitable tools to investigate it. At the same time, passive actuators are based on sorption, which is the interaction at molecular level between a fluid phase and a solid one.

Since we want to investigate the effect of materials architecture on the expansion properties of cellular structures we need a method to “build” materials where we have full control on their composition and structure. For this scope, simulations are best suited: depending on the investigated phenomenon (and on its scale) different simulation techniques can be used; from larger scales to lower ones, material is considered as a continuum, a collection of discrete elements or molecules.

Another useful technique that we could take advantage of is rapid prototyping, where one is able to “print” three dimensional objects with almost any shape. In this way we could manufacture real models which could serve as real counterparts of the simulated materials and check for the significance and validity of our findings based on the simulations.

In our work both the simulation and the prototyping “routes” were considered. In particular we will introduce the reader to the following methods:

### 3. Materials & Methods

- Finite Element simulations and micromechanical modelling to investigate the expansion behaviour of cellular structures. These methods and our implementation of them will be described in section 3.1 and 3.2.
- Real swelling experiments on 3D-printed models. These experiments and the protocol to obtain the models are described in section 3.3.
- Monte Carlo simulations of water in nanosized pores to investigate the water-substrate interactions in strong confinement and possibly occurring deformations. This will be introduced in section 3.4.

#### 3.1 Finite Element analysis of pressurised periodic lattices

In this section we deal with the method used to understand the influence of cellular material structure to its swelling properties. Our modelling strategy is motivated upon the characteristics of the *Delosperma nakurense* seed capsule that we introduced in section 2.1.2 and shortly recall here.

The reversible unfolding of the capsule is based on the constrained swelling of a hygroscopic material (CIL) inside the lignified cells of the keels tissue, which results in mechanical loading of the enclosing cellular structure. Since the CIL is made of a highly hygroscopic material, whereas the cells of the keels tissue are lignified and hence inhibit sorption of water, one can consider, as a first approximation, that the walls don't expand. Therefore the overall anisotropic swelling depends on the geometry of the cellular structure and the uniform volumetric expansion of the enclosed phase.

In the following, we will consider several lattices, characterized by different geometrical designs, subjected to a uniform hydrostatic pressure acting in the cells. Their mechanical behaviour is assessed by means of finite elements simulations (a basic introduction to the method follows).

Each finite element model is divided into a structural domain that coincides with the walls of the lattice, and a fluid domain occupying the cavities of the cells. The mechanical behaviour is then described in terms of “swelling eigenstrains”, which

measure the deformation of the whole cellular structure due to pressurization by the fluid, and the effective elastic properties of the lattice at different degrees of expansion.

### 3.1.1 *Finite Element method*

The finite element method is an approximate method to solve complex systems of partial differential equations for which an analytical solution is not granted.

While we will not enter in the generality of the method that can be found elsewhere [84], we here introduce the formalism of the standard displacement-based finite element analysis for a generic static elastic problem, as it is implemented in the software ABAQUS® 6.12 (Dassault Systèmes Simulia Corp.) which was used in the simulations.

A general static elastic problem aims to search the equilibrium configuration of a mechanical system due to given forces and constraints. The equilibrium statement for such a system can be put in its so-called weak form via the virtual work principle:

$$\int_V \boldsymbol{\sigma} \cdot \delta \boldsymbol{\varepsilon} dV = \int_S \mathbf{t} \cdot \delta \mathbf{v} dS + \int_V \mathbf{b} \cdot \delta \mathbf{v} dV \quad 3-1$$

which states the equality between the work of internal forces ( $\boldsymbol{\sigma}$  and  $\boldsymbol{\varepsilon}$  are any conjugate pairing of material stress and strain measures) and external ones ( $\mathbf{t}$  and  $\mathbf{b}$  are respectively the -known- surface and volume forces;  $\mathbf{v}$  are virtual displacements compatible with all kinematic constraints.) over a certain domain (the volume  $V$  and its boundary surface  $S$ ). Except from very simple cases, an analytical solution to such a problem can't be found. The finite element method considers an approximated version of this problem, where the original domain is subdivided into smaller intervals (a procedure called *meshing*), such that a “piecewise” solution can be found. Each “piece” of solution exists in a finite element “ $e$ ”, which comprises a domain of definition (the interval), shape functions  $N_i$  (whose role will be explained next) and  $n$  nodes which are common vertexes shared by neighbouring elements (with  $n=3$  and  $n=4$  in a triangular and quadrangular mesh respectively).

### 3. Materials & Methods

The bridging between the original and discretized problem is made by the following considerations. Let's consider a material point of coordinates  $(x, y) \in e$ . In matrix notation<sup>\*</sup>, the strain is the gradient of the displacement  $\mathbf{u}$ :

$$\boldsymbol{\varepsilon} = \frac{\partial \mathbf{u}}{\partial \mathbf{x}} \quad 3-2$$

The stress  $\boldsymbol{\sigma}$  results from the constitutive equation of the material, for example, a generalized Hooke's law:

$$\boldsymbol{\sigma} = \mathbf{C} \boldsymbol{\varepsilon} \quad 3-3$$

with  $\mathbf{C}$  being the matrix representation of the fourth-rank stiffness tensor that transforms the strain tensor into the stress tensor.

The formal passage to the finite element problem is done considering that the displacement of the material point  $\mathbf{u}$  can be expressed as a function of the nodal displacements  $\mathbf{a}^e$  by the following:

$$\mathbf{u} \approx \mathbf{u}^e = \sum_{i=1}^n \mathbf{N}_i \mathbf{a}_i^e = [\mathbf{N}_1, \mathbf{N}_2, \dots, \mathbf{N}_n] \left\{ \begin{matrix} \mathbf{a}_1 \\ \mathbf{a}_2 \\ \vdots \\ \mathbf{a}_n \end{matrix} \right\}^e = \mathbf{N} \mathbf{a}^e \quad 3-4$$

The shape functions  $\mathbf{N}$  interpolate the (discrete) nodal displacements  $\mathbf{a}^e$  and result into an (approximated) displacement field  $\mathbf{u}^e$  continuous over the element. The shape functions are formally matrixes of size  $d$ -by- $dn$  where  $d$  is the dimensionality of the problem (2 for planar and 3 for three dimensional), and  $n$  is the number of nodes in the element  $e$ . Usually the shape functions are chosen as simple polynomials, (linear or quadratic) whose integral is easy to calculate numerically.

Substituting equation 3-4 into 3-2 and these into 3-3, the strain and stress state in the element can be expressed as:

---

<sup>\*</sup> It is known that both strain and stress are symmetric second-rank tensors by their transformation properties; however in our notation we will represent tensorial quantities using matrix notation. Strain and stress second-rank tensors become column vectors by the following indices contraction rule: 11→1, 22→2, 33→3, 23=32→4, 13=31→5, 12=21→6). Similarly, the stiffness which is a fourth-rank tensor becomes a 6-by-6 matrix.

$$\begin{aligned}\boldsymbol{\varepsilon} &\approx \boldsymbol{\varepsilon}^e = \frac{\partial \mathbf{N}}{\partial \mathbf{x}} \mathbf{a}^e = \mathbf{B} \mathbf{a}^e \\ \boldsymbol{\sigma} &\approx \boldsymbol{\sigma}^e = \mathbf{C} \boldsymbol{\varepsilon}^e = \mathbf{C} \mathbf{B} \mathbf{a}^e\end{aligned}\tag{3-5}$$

Now, since the virtual displacements  $\mathbf{v}$  at the right hand member of equation 3-1 are arbitrary, we can choose them as the nodal displacements  $\mathbf{a}^e$ . In this way equation 3-1 becomes explicitly function of  $\mathbf{a}^e$ . By rearranging the global integrals into sums of single element integrals, it can be putted in the following form:

$$\mathbf{K} \mathbf{a} = \mathbf{f}\tag{3-6}$$

where  $\mathbf{a}$  is the –unknown- global nodal displacement vector,  $\mathbf{K}$  is the so-called global stiffness matrix and  $\mathbf{f}$  is the vector of the external forces acting on the system:

$$\begin{aligned}\mathbf{a} &= \sum_e \mathbf{a}^e \\ \mathbf{K} &= \sum_e \int_{V_e} \mathbf{B}^T \mathbf{C} \mathbf{B} dV \\ \mathbf{f} &= \sum_e \int_{V_e} \mathbf{N}^T \mathbf{b} dV + \sum_e \int_{A_e} \mathbf{N}^T \mathbf{t} dA + \mathbf{r}\end{aligned}\tag{3-7}$$

Here  $\mathbf{r}$  is the vector of the concentrated nodal forces (for instance a point-load acting on the boundary).

In this form the equilibrium condition 3-6 is a system of algebraic equations and therefore can be solved numerically upon the unknowns  $\mathbf{a}$  by a proper algorithm (like the Newton-Raphson method). All other mechanically relevant quantities (such as the strain and the stress over the entire domain) can be calculated from equations 3-5.

### 3. Materials & Methods

#### *3.1.2 Geometry of the cellular structures*

The cellular structures considered here are two-dimensional, periodic structures. In the most general case they show (at least) the symmetry of a 2D Bravais oblique lattice. Then, the unit cell of the lattice (that is the smallest portion of structure which repeated develops the entire cellular structure) is identified by 2 vectors connecting the lattice points. The “crystallographic” lattice and the cellular structure can coincide in particular cases (see Figure 3-1 a), but this is not the general case. For convenience, in the remainder of the manuscript, we will use the term lattice to refer to the cellular structures. Since our aim is to understand the influence of lattice architecture onto its swelling behaviour, we have to firstly define some parameters upon which we can compare architecture. In particular we restrict our investigation to lattices that differ in terms of anisotropy, connectivity and cell convexity (see equations 2-1 and 2-5). Each of these lattices is composed of only one tile. Three types of tiles have been used: a convex diamond shaped tile, and two non-convex tiles, named “L” and “T” tiles (see Figure 2-1). The diamond tile has  $l=38$  mm,  $t=2.9$  mm and  $\alpha=23^\circ$ . The “L” and “T” tiles have both the same area ( $A=100$  mm<sup>2</sup>) and a short beam of length  $l_L=5.7736$  and  $l_T=5$  respectively ( $t$  is chosen such that  $l/t=10$ ), and a convexity of  $C_L=0.589$  and  $C_T=0.503$  respectively.

Each lattice has been modelled in ABAQUS 6.12 by arraying one or more tiles along the two lattice vectors.

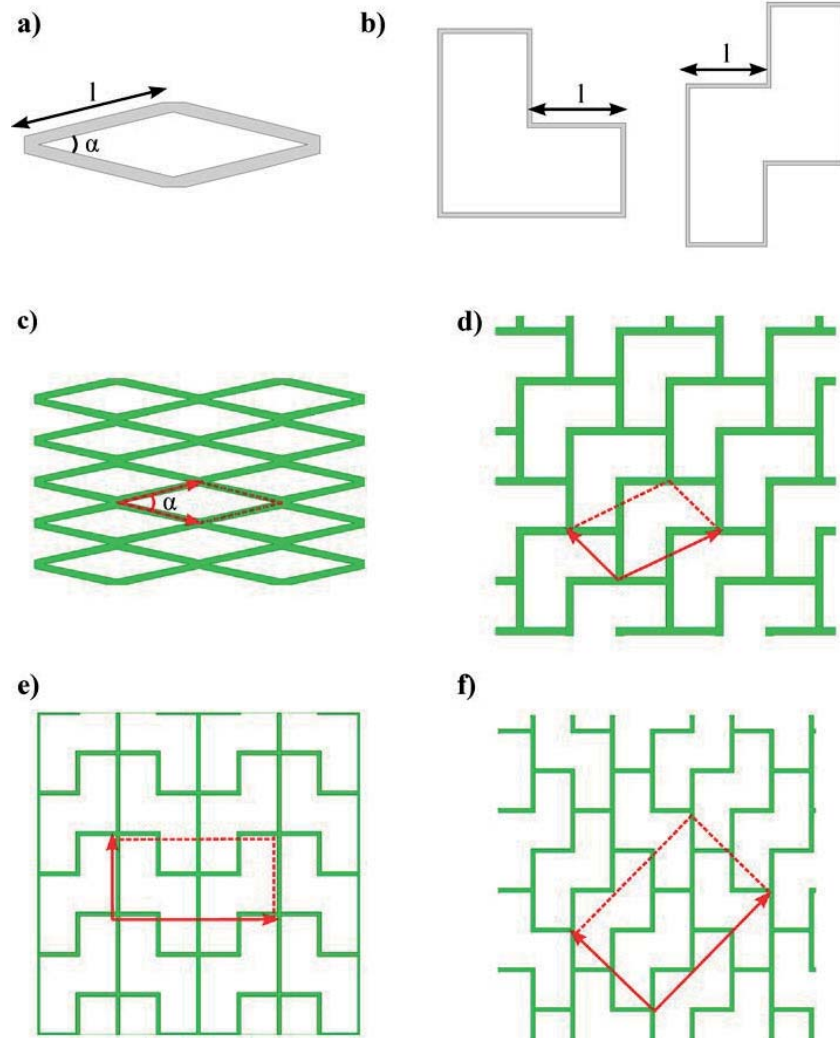


**Figure 3-1** Some of the cellular structures implemented in the FE simulations.

Each lattice is composed by one single type of tile: a) diamond; or b) “L” and “T” tiles. These two share same area ( $A=100$ ) and same wall aspect ratio ( $l/t=10$ ), but have a different convexity (0.589 and 0.503 respectively). Non-convex tile can generate many different lattices (c to f): these will differ in terms of anisotropy, nodal connectivity and cell convexity. All lattices, despite their geometrical complexity, show at least the symmetries of an oblique 2D Bravais lattice, whose repetitive unit cell is drawn in each example in black.

### 3.1.3 Simulation details: prescribed conditions

In all FE simulations, the structural domain (lattice walls) has been discretized by means of a structured mesh, using bidimensional planar stress continuum elements with reduced integration (CPS4R elements of ABAQUS element library); the fluid domain is modelled

### 3. Materials & Methods

by fluid cavities based on the walls' surfaces and linear fluid cavity elements (F2D2 elements of ABAQUS element library) for those cavities lying across a periodic boundary.

External forces and kinematic constraints will appear as elements of, respectively,  $\mathbf{F}$  and  $\mathbf{U}$  in equation 3-6. In the lattices considered, the external forces are hydrostatic pressures acting on the surface of each cell (see Figure 3-2). The lattices walls are considered to be linear elastic with a Young modulus  $E=1\text{GPa}$  (if not otherwise stated) and Poisson's ratio  $\nu=0.3$ . These values are typical for cell wall transverse modulus of spruce wood in moist conditions [85]. In particular, the diamond honeycomb was used as a test case; here a preliminary simulation with  $E=1\text{GPa}$  and pressure  $p=0\text{-}13\text{ MPa}$  was performed to assess the deformation behaviour. Then, pressure relaxation and subsequent homogenization were repeated in a parametric study spanning several values of pressure  $p=0\text{-}9\text{ MPa}$  and  $E=1\text{-}9\text{ GPa}$ . All remaining lattices were studied with fixed  $E=1\text{GPa}$  in a range of pressures  $p=0\text{-}3\text{ MPa}$ .

Since the deformations upon pressurization reach large values, the FE simulations assume finite strains (that is, the strain definition includes higher order derivatives of the deformation) and true stresses (as the ratio between the force and the actual area of the element surface).

In our case, kinematic constraints corresponding to the periodicity of boundaries (eq. 2-16) have to be applied. This is enforced by a condition of the kind:

$$\mathbf{u}(\mathbf{x}^+) - \mathbf{u}(\mathbf{x}^-) = \mathbf{u}^{moving} - \mathbf{u}^{fixed} \quad 3-8$$

Where the symbols “+” and “-” refer to opposite boundary nodes (that is, top and bottom or right and left) and “moving” and “fixed” refer to standalone nodes that are not part of the structural domain. Equation 3-8 ensures that the relative displacement between opposite boundary nodes equals the displacement of the moving standalone nodes (fixed ones act as a reference so that  $\mathbf{u}^{fixed} = 0$ , see Figure 3-2). The average strain imposed to the lattice follows from the displacement of the moving standalone nodes (where  $R$ ,  $L$ ,  $T$ ,  $B$  refer respectively to right, left, top, bottom nodes):



$$\tilde{\mathbf{E}} = \begin{pmatrix} \varepsilon_x & \varepsilon_{xy} \\ \varepsilon_{xy} & \varepsilon_y \end{pmatrix} = \begin{pmatrix} \frac{u_x^{RL}}{X_0} & \frac{u_y^{RL}}{X_0} \\ \frac{u_y^{RL}}{X_0} & \frac{u_y^{TB}}{Y_0} \end{pmatrix} \quad 3-9$$

For example, to stretch the lattice along the y direction, the top-bottom moving standalone nodes are displaced upwards. Analogously, a shearing deformation is obtained by displacing the right-left moving standalone nodes up- or downwards.

The lattice area strain then is calculated as:

$$\frac{dA}{A_0} = (1 + \varepsilon_x)(1 + \varepsilon_y) - 1 \quad 3-10$$

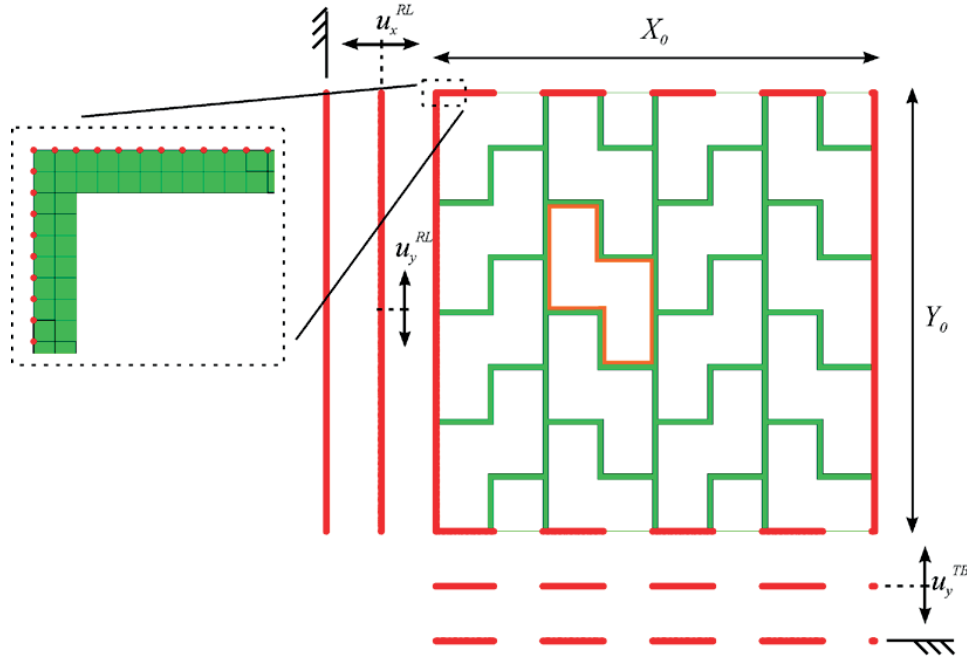


**Figure 3-2 Details of the FE simulation on a typical lattice.**

The structural domain is discretized by linear two-dimensional continuum elements (CPS4R elements of ABAQUS 6.12 element library). The inset shows an enlarged view of the mesh with boundary nodes highlighted in red. Every lattice is subjected to a hydrostatic pressure applied to the inner surface of each cell (highlighted in orange for one cell). Periodicity conditions are prescribed to the boundary nodes (outer red contour of the lattice) by enforcing equation 3-8. Average principal strains  $\varepsilon_x$ ,  $\varepsilon_y$  are applied to the lattice by displacing, respectively, right-left standalone nodes horizontally and top-bottom standalone nodes vertically. Shear strains  $\varepsilon_{xy}$  are applied by a vertical displacement of right-left standalone nodes.

### 3. Materials & Methods

#### 3.1.4 Estimation of swelling eigenstrains and elastic properties

In the lattice systems considered here, two mechanical contributions are present: a hydrostatic pressure in the fluid cells, and the elastic stresses developed in the lattice walls. The lattice will be in mechanical equilibrium when these two contributions are balanced. From equation 2-14 (which states the equivalence between surface and volume forces), the equilibrium condition implies that the resultant of the forces on the boundary is zero. Operationally, the equilibrium state is calculated with an iterative search: at each iteration tentative boundary displacements  $u_x^{RL}$ ,  $u_y^{TB}$  and  $u_y^{RL}$  are prescribed to the lattice (see Figure 3-2) and the residual forces on the boundaries are calculated with a FE simulation. At the next iteration the boundary displacements are adjusted depending on the sign and magnitude of the residual forces. The iterative search ends successfully when these forces are lower than a given threshold (10E-04). Then, the corresponding average strains  $\tilde{\mathbf{E}}_0$  (see equation 3-6) are the swelling eigenstrains searched for, and the lattice is “relaxed”. Different relaxed configurations are found depending on the value of pressure, that is,  $\tilde{\mathbf{E}}_0$  is function of  $p$ .

The estimation of the effective elastic properties follows the method presented in paragraph 2.2.3. In our case equation 2-13 takes the form:

$$\tilde{\mathbf{C}}_{eff} = (\tilde{\mathbf{E}} - \tilde{\mathbf{E}}_0)^{-1} : \tilde{\mathbf{\Sigma}} \quad 3-11$$

This means that the starting configuration to perform the homogenization of the elastic properties is  $\tilde{\mathbf{E}}_0$ . Then the problem reduces to the calculation of the global stress  $\tilde{\mathbf{\Sigma}}$  due to an incremental imposed average strain  $(\tilde{\mathbf{E}} - \tilde{\mathbf{E}}_0)$  by means of a FE simulation (in our simulations we used a probing strain of 1% and 5% respectively for the diamond honeycombs and non-convex lattices). Again,  $\tilde{\mathbf{\Sigma}}$  is calculated as the resultant of the forces on the boundary nodes (equation 2-14) by applying on the relaxed system basic loading cases like uniaxial stretching/shrinking in direction  $x$  and  $y$  and  $xy$  shearing, as detailed in the former paragraph.

Since our lattices are planar, the out of plane components of the effective stiffness tensor are neglected and  $\tilde{\mathbf{C}}_{eff}$  becomes:

$$\tilde{\mathbf{C}}_{eff} = \begin{bmatrix} C_{11} & C_{12} & C_{16} \\ C_{12} & C_{22} & C_{26} \\ C_{16} & C_{26} & C_{66} \end{bmatrix} \quad 3-12$$

(here the contracted tensorial notation applies: 11→1, 12→6, 22→2)

In case of lattices with mirror symmetries (Figure 3-1 c, d, e), the effective stiffness tensor simplifies even more since the shear-direct cross terms ( $C_{16}$ ,  $C_{26}$ ) are also null.

### 3.1.5 Finite-size, periodic system comparison

To check the validity of our modelling approach based on periodic boundary conditions we compared the swelling eigenstrains estimation obtained via the homogenization technique (see paragraphs 3.1.3 - 3.1.4) with that of a finite size diamond honeycomb composed of n-by-n cells. In Figure 3-3 it can be seen that the finite size system prediction converges to the periodic estimation with increasing system size, confirming the correctness of the homogenization.

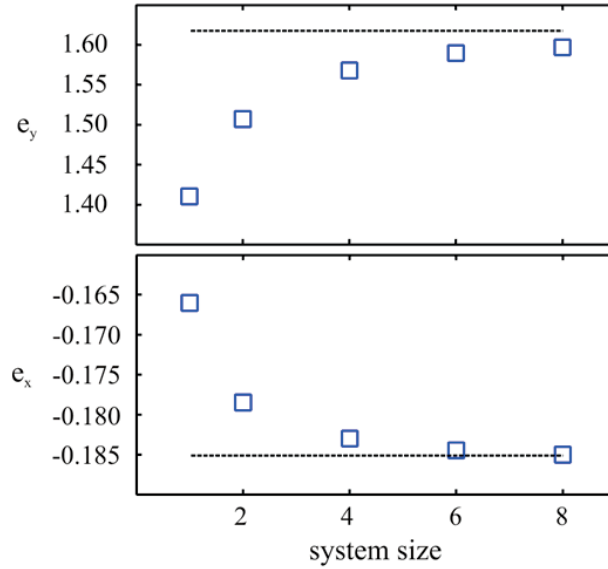


**Figure 3-3 Comparison between finite size and periodic FE models.**

*Estimation of the swelling eigenstrains through a n-by-n cells finite size honeycomb (blue squares) and a periodic one (black dotted line). The value calculated for the finite system depends on the honeycomb size and reaches an asymptotic value at about 8 cells. The periodic system instead is size independent and coincides with the asymptotic value.*

### 3. Materials & Methods

#### 3.2 Micromechanical analysis of pressurised lattices

The aim of this section is to present an analytical model that is able to describe the actuation behaviour of pressurized lattices both in terms of swelling eigenstrains and effective stiffness, using simple geometrical information related to the lattices' microstructure. In simple cases such as the diamond honeycomb, lattice points and structural joints coincide (see Figure 3-1 c) and the parallel between the micromechanical and finite element models can be easily traced. In the following, we will present our modelling strategy applied to the case of the diamond honeycomb: nonetheless, the method is general enough to be transferred to more complex 2D geometries.

##### 3.2.1 *A fluid-structure model*

As seen in paragraph 3.1.2, all cellular structures presented here show at least the symmetry of a 2D Bravais oblique lattice. The purpose of our micromechanical analysis is to obtain an analytical form for the internal energy of a pressurized lattice, starting from the knowledge of the oblique unit cell, which is drawn in black in Figure 3-1. As for the FE simulations, two contributions are present: an elastic term related to the structural domain, and a field related to the effect of the fluid. Therefore the lattice is described by a fluid-structure potential that will depend on two kinematic variables: the lattice angle  $\alpha$  and the point-to-point strain  $\epsilon$ . Then, the lattice strains  $\epsilon_x$ ,  $\epsilon_y$  along two principal directions are obtained by projection.

The elastic response of the lattices can be described by means of the Born model [86, 87]. In this model each lattice point is connected to its nearest neighbours by two kind of springs: a longitudinal spring  $K_l$  and a transverse one  $K_t$ . The non-zero transverse stiffness  $K_t$  is needed to avoid the so called uniconstant elasticity theory governed by 'Cauchy relations'. For an isotropic medium, the Cauchy relations imply a Poisson's ratio of 1/4 for all materials described by the model [88]. As already pointed out by Fratzl and Penrose [89] this is a consequence of considering just central forces for a crystal, which clearly doesn't hold for real crystals or lattice materials.

### 3. Materials & Methods

The fluid phase acts as an external field on the cellular structure; its contribution is written as the work done by the fluid from the undeformed normalized volume  $V_0 = \sin(\alpha_0)$  to a generic deformed one  $V = (1 + 2\varepsilon)\sin(\alpha)$ .

The pressure term in general is not restricted to a specific form, but as in the FE study, we choose a constant value (isobaric) which is independent of the volume of the single cell. In passing we also note that different forms of pressure terms could also be implemented in the model to capture its potentially different physical origins. For example, an osmotic pressure could be included, and will be in general dependent on the volume of the solute-solvent mixture, while a fluid confined to the cells will undergo an isothermal transformation.

Then the fluid-structure potential is:

$$W = W_{stretching} + W_{bending} + W_{pressure} \quad 3-13$$

Where:

$$\begin{aligned} W_{stretching} &= K_t \frac{(\varepsilon - \varepsilon_r)^2}{\sin(\alpha_r)} \\ W_{bending} &= K_t \frac{\sin\left(\frac{\alpha - \alpha_r}{2}\right)^2}{\sin(\alpha_r)} \\ W_{pressure} &= -p \frac{V - V_r}{V_r} \end{aligned} \quad 3-14$$

where the lattice angle  $\alpha_r$ , wall strain  $\varepsilon_r$  and lumen volume  $V_r$  refer to a reference configuration. The physical meaning of the fluid-structure potential is that of a strain energy function of the cellular structure with the fluid being considered internal to the system. Again, the geometrical parameters  $\alpha$  and  $\varepsilon$  refer in this particular case to the honeycomb's angle and walls' strain, but in general they are not related to the material structure as they refer to the "crystallographic" lattice (see Figure 3-1).

The swelling eigenstrains are the coordinates of the energy minimum when the reference is set to the undeformed configuration ( $\alpha_r = \alpha_0$ ,  $\varepsilon_r = 0$ ), and can be calculated analytically by minimizing equation 3-13 with respect to the kinematic variables ( $\alpha$ ,  $\varepsilon$ ):

### 3. Materials & Methods

$$\begin{cases} \frac{\partial W}{\partial \alpha} = 0 \\ \frac{\partial W}{\partial \varepsilon} = 0 \end{cases} \rightarrow \begin{matrix} \alpha(p, E) \\ \varepsilon(p, E) \end{matrix} \rightarrow \begin{matrix} \varepsilon_x = (1 + \varepsilon) \frac{\cos\left(\frac{\alpha}{2}\right)}{\cos\left(\frac{\alpha_0}{2}\right)} - 1 \\ \varepsilon_y = (1 + \varepsilon) \frac{\sin\left(\frac{\alpha}{2}\right)}{\sin\left(\frac{\alpha_0}{2}\right)} - 1 \end{matrix} \quad 3-15$$

The calculation of the effective stiffness tensor components (remember equation 3-12) necessitate taking the pressurised state as the reference ( $\alpha_r = \alpha_p$ ,  $\varepsilon_r = \varepsilon_p$ ) and are found via the following:

$$C_{11} = \frac{\partial^2 W}{\partial \varepsilon_x^2}, \quad C_{22} = \frac{\partial^2 W}{\partial \varepsilon_y^2}, \quad C_{12} = \frac{\partial^2 W}{\partial \varepsilon_x \partial \varepsilon_y}, \quad C_{66} = \frac{\partial^2 W}{\partial \varepsilon_{xy}^2} \quad 3-16$$

#### 3.2.2 Parameterization of the fluid-structure potential

Since the diamond-shaped honeycomb coincides with “crystallographic” lattice, we assign to the longitudinal and transverse spring constants  $K_l$  and  $K_t$  a value reflecting the axial and bending rigidity of a single wall. When the walls undergo severe distortion (that is deviate sensitively from their original shape) the rigidity of the walls can change. This is not accounted in the original Born model which was developed for small strain elasticity of crystals. Therefore we introduce two weight functions (cubic polynomials  $c_1$ ,  $c_2$ ) to better model the actual wall rigidity at different states of deformation and obtain:

$$\begin{aligned} K_l &= E \frac{t}{l} c_1(\alpha) \\ K_t &= E \left(\frac{t}{l}\right)^3 c_2(\alpha) \end{aligned} \quad 3-17$$

The weight functions fit two datasets obtained by two separate sets of FE simulations. These two sets are conceived to decouple the longitudinal and transversal loading of the wall, while mimicking the actual deformation of the wall observed in the simulations of the pressurized honeycomb. In both simulations, a single “arm” of the unit cell is considered with its extremities constrained to disable local rotations (fig. 7a). In the first set the arm is subjected to pure transversal loading: one end of the arm is displaced along

### 3. Materials & Methods

an arc trajectory around the other end, so that the “net” longitudinal wall strain  $\varepsilon$  stays constantly equal to zero, whereas the wall angle to the horizontal ( $\alpha/2$ ) spans the whole range of expanded states (from  $\alpha_0/2=14^\circ$  to  $\alpha/2=45^\circ$ ). For each intermediate deformed configuration at  $\alpha_i/2$ , a data point for polynomial  $c_2$  is calculated as the ratio between the  $i$ -th strain energy increment  $\Delta\psi_i=\psi(\alpha_{i+1}/2)-\psi(\alpha_i/2)$  and the initial strain energy increment  $\Delta\psi_0=\psi(\alpha_0/2+\Delta\alpha)-\psi(\alpha_0/2)$ . In the second simulations set, S shaped configurations of the arm  $\alpha_i/2$  are taken as the reference, on which pure longitudinal (end-to-end), small strain  $\varepsilon$  is applied. Data points for polynomial  $c_1$  are calculated as the ratio between the longitudinal strain energy  $\Delta\psi_{\text{axial}}(\alpha_i/2)$  in the  $i$ -th S shaped configuration, and the longitudinal strain energy in the straight wall ( $\alpha/2 = \alpha_0/2$ ). Compared to the straight wall, in the S shaped configuration the wall resists more softly to an axial load (Figure 3-4 -b, blue line), just as an Euler column resists less and less as buckling proceeds. At the same time, the wall shows initially a lower tangential stiffness that increases rapidly at more severe deformations (Figure 3-4 -b, red line), due to severe curvature localized near the extremities.

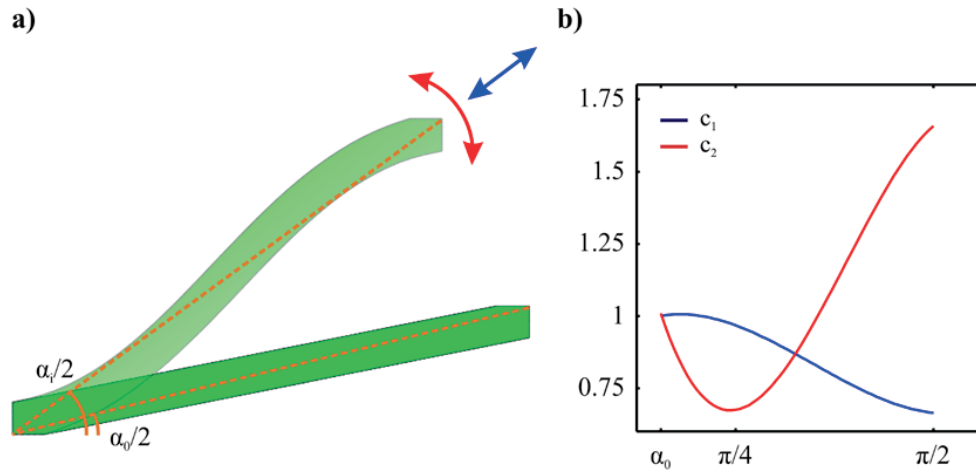


**Figure 3-4 Fitting of the Born springs constants**

*Typical deformed S-shaped configuration of a honeycomb wall under internal pressure (a). Deformation modes can be decoupled in a transversal (red) and longitudinal (blue) component. Born spring stiffness constants ( $K_t$ ,  $K_l$ ) were fitted to the effective rigidities of the wall at different values of lattice angle  $\alpha_i$  (b).*

In the general case when the structural lattice doesn't coincide with the crystallographic one, one should find a proper estimation of the unit cell rigidity; this can be done analytically by “solving the framework” in the crystallographic unit cell or

### 3. Materials & Methods

parameterizing (by means of FE) the mechanical response of the unit cell for a range of direct and shear deformations (this means getting  $K_l = K_l(\alpha, \varepsilon)$  and  $K_t = K_t(\alpha, \varepsilon)$ ).

### 3.3 Swelling experiments of honeycombs

The work done on modelling has the technical advantage that many different configurations of pressurised lattices could be readily tested (in terms of internal pressure, material stiffness and geometry). Nonetheless these represent idealized models where the sorption process taking place in the material forming the cellular structure is on purpose neglected. With the swelling experiments that we are about to introduce in this section, we wanted to create an artificial actuating system based on constrained swelling in cellular structure that is closer to the inspiring example of the *Delosperma nakurense*. For this purpose, we created three dimensional models of cellular structures similar to those we introduced in the FE simulations, made of two materials: a stiff, low-swelling material for the walls and a soft, high-swelling material for the inclusions. This could be achieved with the aid of a multimaterial rapid prototyper and chemical synthesis of hydrogel. The materials available for printing were a mixture of polyacrylates and polyurethanes (see paragraph 3.3.2) that can swell in organic solvents. The geometries of the printed models were a diamond honeycomb with round inclusions in each cell, and models of the lattices T1, T4, T6 and T8 with a layer of soft material lining the cells. These were swollen in isopropanol at ambient conditions ( $T=22^\circ$ ) for a variable period of 4 to 10 days until an equilibrium shape was reached. Also, a hybrid version of swelling diamond honeycomb was created, with rapid prototyped walls and cells filled with a hydrogel. Differently from the others, this model was able to swell in water.

This section covers all the necessary steps that were needed to create these models, characterize their basic constituents and the protocol used for the swelling experiments.

#### 3.3.1 Generation of 3D models

Three dimensional models were created starting from the lattice geometries used in the finite element simulations (see paragraph 3.1.2), by means of a 3D modelling software



(Rhinoceros® 4, Robert McNeel & Associates). The models are created starting from a two-dimensional geometry which then is extruded along the perpendicular direction. The actual samples' geometry differs from the finite element ones for what concerns lattice walls aspect ratio (length/thickness) and the presence of a second phase inside the cells. In particular the walls had a lower aspect ratio. The second phase was shaped as an inclusion in the cellular spaces, or modelled as a layer (of variable thickness) lining the cells' internal surface. These differences were necessary in order to avoid as much as possible sample breakage due to differential swelling of the single components. Also, single-material diamond honeycombs were printed and then filled with an in-house synthesized hydrogel (see next paragraph), in order to get a system that would swell in water.

The lattices had a size of 5-by-10 cells for the diamond-shaped honeycombs, and 6-by-6 cells for the non-convex lattices (80-by-20 mm and 60-by-60 mm respectively). The absolute size of the models doesn't influence the shape change upon swelling but obviously larger models take longer to swell since swelling is related to diffusion. Therefore the absolute sizes were chosen as a trade-off between accuracy of the printer and speed of swelling. Finally, the 3D models were exported in stereolithography (STL) format to be inputted into the rapid prototyper.

#### ***3.3.2 Materials synthesis and swelling protocol***

All samples were built with an Objet® Connex 500 multimaterial 3D printer<sup>†</sup>. The mechanical properties of the printed materials range from the stiffest one (VeroWhite®), which simulates conventional thermoplastics to the softest one which is a rubber-like material (TangoPlus®). The "3D ink" precursor is a mixture of acrylate and urethane monomers and oligomers, cross-linkers, and photoinitiators in a liquid form. Immediately after these inks are ejected from the print heads, they are polymerized with UV light. The inks are deposited in a voxel-by-voxel fashion, so that fine shape control is achieved, with a spatial resolution of ca. 30 microns in the z-dimension. Materials with

---

<sup>†</sup> we are indebted to Dr. James Weaver from Wyss Institute, Boston for his work

### 3. Materials & Methods

eight different intermediate levels of stiffness are obtained by printing juxtaposed voxels of the two “plastic” and “rubber” extremes in different ratios (see next paragraph).

The samples were soaked in isopropanol (iso-propan-2-ol) in glass Petri dishes, covered with a glass lid and sealed with an O-ring. The swelling process was recorded with a camera by taking snapshots every 20 minutes until a stable configuration was obtained (4 to 5 days). Swelling deformations were measured in the central field of the sample with the aid of an image analysis software (ImageJ [90]). As the diamond-shaped honeycombs would break before reaching the equilibrium, the swelling deformations were measured at the last snapshot prior to breakage.

Water swelling samples were built from rapid prototyped diamond-shaped honeycombs filled with superporous poly-acryl-co-acrylamide that was synthesized in-house. The macroscopic porosity enables higher swelling and shrinking rates since diffusion is enhanced by capillary forces driving water in the hydrogel [55]. For the hydrogel synthesis we followed the protocol for the radical polymerization reaction presented by Gemeinhart *et al.* in [55] and reported here briefly.

The monomeric precursors were acrylic acid (AA) and acrylamide (AM) with N,N'-methylene-bis-acrylamide (BIS) as the cross-linker in concentrations of 15% (volume), 10% (weight) and 0.25% (weight). Once the stock monomer solution was made, the pH was adjusted to 5.1 using 50% (weight) sodium hydroxide (NaOH). A surfactant (PLURONIC® F127) was added at 0.5% weight concentration to stabilize the bubbles forming the porosity. Pure water was added to reach an overall volume of solution of 20 ml. The redox initiator pair (2% to the monomer solution weight) was N,N,N',N'-tetramethylene diamine (TEMED) added to the monomer solution and ammonium persulfate (APS) added at the time of polymerization. After 210 seconds from APS addition, 50 mg of sodium bicarbonate (powder) were added and manual stirring was performed with a spatula in order to obtain even dispersion. At this point a rapid prototyped honeycomb (T+ material) was inserted in the reaction glass. Slight foaming would occur and be visible by whitening of the solution, such that the porosity could be “frozen” by the ongoing polymerization, which was allowed to proceed for the next 4 hours. Eventually, parts of hydrogel not enclosed in the honeycomb's cells were

manually removed. The “hybrid” model so obtained was left swelling in water until an equilibrium shape was reached.

#### ***3.3.3 Assessment of mechanical and swelling properties***

The Young modulus for all materials available for 3D printing were obtained with the following protocol and are reported in Table 4-1.

Tensile tests were performed on a Zwick/Roell® testing machine, equipped with a 500 N load cell according to standard test method for tensile properties of plastics ASTM D 638. All tests were conducted at a crosshead speed of 1 mm/min at room temperature (22°C). For the tests, dog bone shaped tensile samples with a neck cross section of 3.0 by 3.4 mm and 6.0 by 3.4 mm were used. Strain was measured as the ratio between crosshead travel distance and effective grip-to-grip separation and it resulted within 5% error to the effective strain, measured manually with a gauge in the neck portion. A preload of about 0.5–1.0 N was applied to the samples before commencing. Young modulus was extrapolated as the linear regression of the stress-strain curve in a given  $\sigma_{\text{low}}-\sigma_{\text{high}}$  stress interval (which was individually chosen for each material in the stress linear range).

The materials used by the 3D printer are impermeable to water but can swell in organic solvents. The strains upon free swelling in isopropanol for each material were measured on bar-shaped samples when the final shape was reached – see Table 4-1.

#### **3.4 Monte-Carlo simulations of water in nanosized pores**

As seen in paragraph 2.3.2 sorption in a nanoporous material can exert dramatic effects in terms of mechanical pressures on the pore walls and hence material deformation, especially in the case of water.

In this section we want to introduce the modelling technique to study water sorption in a nanoscopic pore. The aim is to understand which are the relevant parameters (pore wall stiffness, pore size, external conditions) for the generation and extent of pore-wall stresses and eigenstrains. To do this, we chose to use the Monte Carlo method together

### 3. Materials & Methods

with an atomistic model for water. In reality, since our implementation of the Monte Carlo simulations of bulk water wasn't successful, simulations in nanoconfinement were not even performed.

Since the average reader should be quite familiar with the matter, we present here only the basics of the Metropolis Monte Carlo method applied to molecular systems, with a special focus on the peculiarities related to multiatomic particles like water. This treatment is in all respects non exhaustive; more details can be found in the excellent books by Allen and Tildesley [91], Frenkel and Smith [92], Klapp and Schoen [93].

#### ***3.4.1 Monte Carlo simulations of molecular systems***

The main idea of statistical mechanics is that macroscopic properties of a thermodynamical system (macrostate:  $N$ ,  $V$ ,  $T$ ,  $p$ ,  $\mu$ ,  $T...$ ) can be derived from its ensemble average. By ensemble it is intended a collection of identical copies of the system in different microstates corresponding to the same macrostate. A microstate is a point in the multidimensional phase space ( $6N$  dimensions: 3 coordinates and 3 momenta for each of the  $N$  particles), that is a single realization, a snapshot, of the system. The macroscopic properties are correctly estimated if the phase space is adequately sampled. Now, not all microstates are equally probable. Therefore the ensemble average depends on the probability distribution of these states. The more close to this average is a microscopic state, the more “important” is it for the calculation of the average itself. Importance sampling is at the core of the Metropolis Monte Carlo method. This is a customary method to generate a trajectory in phase space which samples from a chosen statistical ensemble [91]. Here a Markov chain of microstates is generated by random moves that operate the transition from one microstate  $m$  to the next  $n$  (this is the Monte Carlo “move”). The move is always accepted if it lowers the energy of the system. Otherwise, the move is accepted depending on the ratio between the probabilities of the two states  $\rho_n/\rho_m$ . At this point a random number on  $(0, 1)$  is generated: if it is higher than  $\rho_n/\rho_m$  the move is rejected, otherwise it is accepted.

The Monte Carlo move and the limiting distribution  $\rho_n/\rho_m$  (that is the probability of move acceptance) depend on the statistical ensemble chosen for the simulations. Moreover, for

rigid pluriatomic molecules as in our case, some specific schemes are needed (see paragraph 3.4.3).

In the canonical ensemble (constant NVT), the move consists of randomly displacing (and rotating in our case) a molecule, and the limiting distribution is:

$$\frac{\rho_n}{\rho_m} = \exp[-\beta \Delta U] \quad 3-18$$

where  $\Delta U$  is the change in energy due to the Monte Carlo move.

In case of isothermal-isobaric ensemble (constant NPT), an additional volume move is implemented as a change in the simulation box volume  $\Delta V$ ; then the limiting distribution becomes:

$$\frac{\rho_n}{\rho_m} = \exp \left[ N \ln \left( \frac{V_n}{V_m} \right) - \beta (\Delta U + P \Delta V) \right] \quad 3-19$$

### 3.4.2 The TIP4P/2005 water model

Molecular simulations of water suffer the limitation that no single potential can reproduce the entire phase diagram. Water is a complex fluid, many of its properties derive from its ability to build up a hydrogen bond (HB) network, and HB are formed and broken depending on the distance and orientation of neighbouring molecules. Nonetheless, many water potentials have been developed in order to replicate at least partially some of water's properties.

Since our aim is to simulate typical scenarios of swelling in plant actuators, the water model has to model faithfully ambient conditions ( $T \approx 300 \text{ K}^\circ$ ,  $p \approx 1 \text{ atm}$ ). Therefore we have chosen the TIP4P/2005 model [94] which, as stated by the authors, works surprisingly well for the condensed states of water<sup>†</sup>.

This model is a reparameterization of the original TIP4P model that fits the maximum of density at ambient pressure. It is based on the Bernal-Fowler geometry and has four

---

<sup>†</sup> We also conducted simulations using the original TIP4P water model 95. Jorgensen, W.L., et al., *Comparison of Simple Potential Functions for Simulating Liquid Water*. Journal of Chemical Physics, 1983. **79**(2): p. 926-935. given the larger amount of available literature data, in order to check the correctness of our implementation of the Metropolis algorithm.

### 3. Materials & Methods

centres, two hydrogens carrying a positive charge, a Lennard-Jones centre located at the oxygen site, and a double negative charge at the M centre located 0.1546 Å below the oxygen on the molecule bisector.

$\epsilon$ [kJ/mol]	$\sigma$ [Å]	$q_H$ [q*]	$d_{OH}$ [Å]	$d_{OM}$ [Å]	$\hat{H\ddot{O}H}$ [°]
0.7749	3.1589	6.55817	0.9572	0.1546	104.52

**Table 3-1 Parameters of the TIP4P/2005 water model.**

The molecule-molecule interaction accounts for both the Lennard-Jones and the Coulombic potential. The latter are long-ranged, meaning that a simple truncation would cause the correction tail to diverge [92]. The Ewald summation has been implemented to properly manage the Coulombic interactions.

Rigorous derivations of the Ewald Sum for single point (ion) charges can be found in the texts the reader was already referred to [91-93]. Here we provide the less common formulas that apply in the case of rigid molecules with multiple charges. The fluid-fluid potential is therefore:

$$U = U^{LJ} + U^{Coulomb} \quad 3-20$$

where the Lennard-Jones contribution depends on the oxygen-oxygen distances:

$$U^{LJ} = 4\epsilon \left[ \left( \frac{\sigma}{r_{OO}} \right)^{12} - \left( \frac{\sigma}{r_{OO}} \right)^6 \right] \quad 3-21$$

and:

$$\begin{aligned}
U^{Coulomb} = & \frac{1}{2} \sum_{i=1}^N \sum_{j=1}^N \sum_{\mathbf{n}} q_i q_j \frac{\text{erfc}(\alpha |\mathbf{x}_{ij} + \mathbf{n}|)}{|\mathbf{x}_{ij} + \mathbf{n}|} + \\
& + \frac{2\pi}{V} \sum_{\mathbf{k} \neq 0} \frac{1}{k^2} \exp \left[ -\frac{k^2}{4\alpha^2} \right] a(\mathbf{k}) a^*(\mathbf{k}) + \\
& - \sum_{n=1}^{N_{mol}} \sum_{i=1}^3 \sum_{j=i+1}^3 q_{n_i} q_{n_j} \frac{\text{erf}(\alpha |\mathbf{x}_{n_i n_j} + \mathbf{n}|)}{|\mathbf{x}_{n_i n_j} + \mathbf{n}|} - \frac{\alpha}{\sqrt{\pi}} \sum_{i=1}^N q_i^2 + \frac{2\pi}{V} \frac{1}{(2\epsilon' + 1)} \left| \sum_{i=1}^N q_i \mathbf{x}_i \right|^2
\end{aligned} \quad 3-22$$

where  $\text{erf}$  and  $\text{erfc}$  are the error function and its complementary.

In equation 3-22, the first term is the real space contribution:  $N$  is the total number of charges (that is:  $N=3N_{mol}$ ),  $\mathbf{x}_{ij}$  is the distance between two charges  $q_i$  and  $q_j$  belonging to distinct water molecules. The second term is the reciprocal space contribution: here,  $V$  is the simulation box volume,  $\mathbf{k}$  is a wavevector of the reciprocal space and  $k^2$  is its squared modulus,  $\alpha$  is the Ewald sum screening parameter, and:

$$a(\mathbf{k}) = \sum_{i=1}^N \sum_{j=1}^N q_i \exp[-i\mathbf{k} \cdot \mathbf{x}_i] \quad 3-23$$

Since the reciprocal space term considers all charges as if they were isolated (like ions), the potential has to be corrected by the so-called exclusion term (the third one), which depends only on the intramolecular distances. The fourth term compensates for the unphysical self interaction of a charge implicitly included in the reciprocal space term. The fifth term is the long range contribution and is due to the total dipole moment of the system which is thought immersed in a continuum of dielectric constant  $\epsilon'$ . In passing we note that both the exclusion and the self term need to be computed just once at the beginning of the simulations, since the water molecules are considered rigid and non polarisable.

### 3.4.3 Simulation details for bulk water system

The simulations were run using a home written program (FORTRAN 95) on a Quad-Core 3 GHz AMD Opteron™ Processor computing cluster at the *Stranski Laboratorium für Theoretische und Physikalische Chemie, TU Berlin*<sup>§</sup>.

The code implements the minimum image convention, with periodic boundary conditions and neighbour list to speed up the execution. All quantities have physical units according to the International System: [nm] for length, [K] for temperature, [kJ][mol]<sup>-1</sup> for energy, [MPa] for pressure; charges are expressed as:

---

<sup>§</sup> The program was written starting from a code by M. Schoen and G. Günther originally developed for monoatomic particles with a Lennard-Jones like short-ranged potential.

### 3. Materials & Methods

$$q^* = q \sqrt{\frac{N_A}{4\pi\epsilon_0}} \quad 3-24$$

and have dimension  $[\text{kJ}]^{0.5}[\text{mol}]^{-0.5}[\text{nm}]^{0.5}$ , so to deal with float numbers close to unity.

A real space cutoff of 8.5 [Å] was applied both to the Lennard-Jones and the Coulomb potentials. The Ewald sum screening parameter was set at  $\alpha=3.5 [\text{nm}]^{-1}$ . The reciprocal space cutoff was set at  $|\mathbf{k}_{\text{max}}|=8$ ; moreover, exploiting the spherical symmetry of the wavevectors and the invariance of the dot product in equation 3-24, we were able to half their number, so to obtain a total of 1024 wavevectors (thereby a factor 2 has been added to the reciprocal space contribution in equation 3-22). Due to the intensive computational power required for the calculation of the Coulombic potential, we considered systems with a size of  $N=360$  water molecules. Typical runs lasted from a minimum of 2 hours (NVT,  $N=360$ ,  $\tau=10^5$ ) to a maximum of 5 days (NpT,  $N=1024$ ,  $\tau=10^6$ ).

A typical simulation proceeds as in the following. Initial configurations of the system are generated by random seeding of the simulation box, whereby a random molecule orientation is obtained using the Marsaglia algorithm (see appendix G4 in [91]). Then the system is relaxed for  $\tau=5000$  Monte Carlo “sweeps”, a sweep being a set of  $N$  moves.

At each iteration a canonical move is attempted; this can be either a random displacement or a random rotation of a single water molecule. The maximum amplitude of the move is adjusted in both cases, so to obtain an average acceptance ratio of 50%. In case of simulations in the NPT ensemble, a volume move is added after a canonical sweep. This implies a rescaling of the particles positions. Since we consider rigid polyatomic molecules, only the coordinates of one centre shall be rescaled, penalty the unphysical distortion of the molecule geometry. Usually, for large molecules, the centre of gravity is rescaled; in our case, we take the oxygen as the rescaling centre in order to avoid calculating the coordinates for an additional centre, so to reduce the computational time (check has been made that the system evolution is equivalent to the case when the centre of gravity acts as rescaling centre).



### 3.4.4 *Preliminary results of the simulations of bulk water*

In order to check for the correctness of our program, we firstly simulated a bulk water system (that is, without confinement) at gaseous and liquid states.

Simulations in the NVT ensemble using the TIP4P/2005 model were run to replicate a pressure-density curve available in the model's original publication [94], whereby the pressure was calculated by the virial theorem. The results predict high pressures that overestimate the literature data (see Figure 3-5). We also simulated the same points in the NPT ensemble and observed a mismatch between the input pressure and the value of pressure calculated by the virial. Also, simulations in the NPT ensemble at standard conditions ( $T=298$  °C,  $p=1$  atm) predict a gaseous state of water. Again, much higher pressures are needed to get a liquid state.

This hinted to an error in the formula used to calculate the virial or in the implementation of the Metropolis scheme in general.

To tackle this issue, we looked at the structure of the liquid at standard conditions (the TIP4P model [95] was used in this case) calculated both in NVT and NPT ensembles. The oxygen-oxygen correlation function obtained in the NVT simulations was in good agreement with experimental and numerical results [94, 96], whereas in the NPT simulations the fluid was overstructured with the second peak shifted at higher distances (see Figure 3-6). This meant that the error had to be searched in the isothermal-isobaric branch. Therefore, we repeated these simulations avoiding Ewald sum calculation and using a simple cut-off of the Coulombic potential instead ( $N=1024$  molecules,  $r_{cut}=1.4$  nm). Despite the rather crude treatment of the Coulombic interaction, in these simulations, the fluid structures in the NVT and NPT ensembles coincide and are closer to the correct one (see Figure 3-6). We conclude that the error lies in the isothermal-isobaric branch of the code, due to erroneous implementation of the Ewald sum. Despite our efforts, this issue has not been overcome.

To explore the effect of water sorption in nanoconfinement with soft deformable walls, we would have needed to implement a scheme to sample in the semi- grand canonical Monte Carlo ensemble as detailed in [21]. In this case the chemical potential, temperature, and number of wall molecules is fixed, while the number of fluid molecules

### 3. Materials & Methods

and the box volume fluctuate. Given that our implementation of the Ewald sum was erroneous, and that a simple, real-space cut-off would also produce unphysical results by neglecting the long range interactions, we decided to discontinue the investigation on nanoconfined water, although we stay certain that the topic is scientifically of greatest interest.

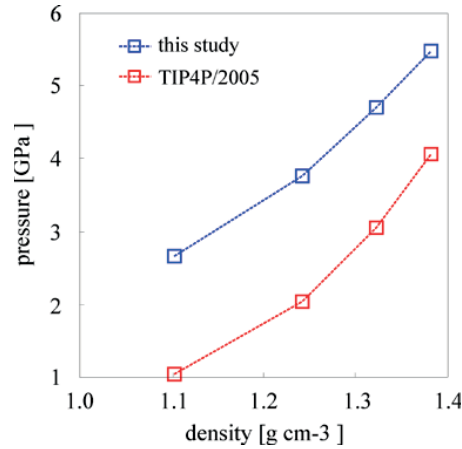


**Figure 3-5 Comparison between the original TIP4P/2005 (red) model [94] and our implementation (blue).**

*Equation of state at  $T=573$  K shows that our implementation of the TIP4P/2005 model overestimates the pressure. The values of pressure at each density were calculated with the virial theorem in the NVT ensemble.*

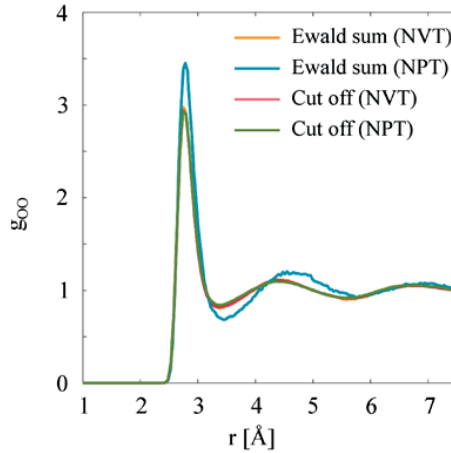


**Figure 3-6 Comparison of TIP4P liquid structure at standard conditions ( $T=298$  K,  $p=1$  atm) simulated in the NVT and NPT ensembles, with the Ewald sum and simple cut off.**

*The lack of agreement between the liquid structure calculated with NPT (blue) and NVT (yellow) simulations evidences an error in the implementation of the NPT Monte Carlo scheme with Ewald treatment of the Coulombic potential. Simulations considering a simple cut-off of the Coulombic potential (red and green) instead converge to the same (correct) structure as in the NVT Monte Carlo simulations with Ewald sum.*

## 4. Results

### 4.1 Finite Element analysis of pressurised anisotropic honeycombs

The FE simulations that have been introduced in paragraph 3.1 make possible to study the effect of internal pressure on the actuation of a cellular material. This actuation will be quantified in terms of *eigenstrains*, since they depict the “spontaneous” deformation state of the honeycomb resulting from internal pressurization. Here we remark that these strains refer to the undeformed dimensions of the whole honeycomb: they describe how the *structure* deforms rather than the *material* forming the walls of the honeycomb. These are presented as small strains (according to equations 3-9 and 3-10), although –as we will see– they are not at all small. Since the honeycomb experiences such large deformations, the FE simulations assume finite strains (that is, the strain definition includes higher order derivatives of the deformation) and true stresses (as the ratio between the force and the actual area of the element surface).

#### ***4.1.1 Microscopic deformation and macroscopic behaviour upon pressurization***

In this paragraph we analyze the diamond honeycomb’s swelling eigenstrains resulting from the preliminary diamond honeycomb simulation (with  $E=1\text{ GPa}$  and  $p=0\text{--}13\text{ MPa}$ ).

#### 4. Results

It is enough to consider only the principal strains  $e_x$  and  $e_y$  since no shearing arises given the mirror symmetries of the honeycomb.

Upon pressurization, the honeycomb undergoes an anisotropic deformation (Figure 4-1). At low pressure ( $p < 1$  MPa) the honeycomb walls deform mostly in bending: they deform into a sigmoid, with localized rotation at the joints that causes an increase of the honeycomb angle and a net increase of the cells volume. At higher pressure ( $p > 1$  MPa) the cells acquire almost a square shape ( $\alpha = 90^\circ$ ) and their volume increases by stretching the walls. These large deformations of the microstructure correspond to a well defined macroscopic behaviour characterized by two stages: a bending dominated regime at low pressures, where the system expands by 300% along the  $y$  direction and shrinks in the  $x$  direction; a stretching dominated regime at high pressures, where the system expands in both directions although with a smaller rate.

The effective bulk modulus of the honeycomb can be extracted by plotting the internal pressure as a function of the strain of the honeycomb volume (Figure 4-1): the bulk modulus (this is the slope of the curve) is very low at low strains, when it deforms by bending, and increases abruptly at higher strains, where the beams resist by stretching. The mode in which the honeycomb resists the pressure load (either bending or stretching) is determined by the geometry of its deformed configuration: therefore the honeycomb rigidity in the first two regimes is a structural property.

Also, at very high pressures ( $p > 10$  MPa) the structure becomes softer, while the eigenstrains increase more than linearly and diverge. The reason for this behaviour is material rather than structure related as we will explain now with a simplified example.

In the stretching dominated regime all cells are fully expanded and have a square shape (Figure 4-2). Since the cells are all equal and the internal pressure is the same, we can study only one cell with side length  $l$  and wall thickness  $t/2$  (where  $l$  and  $t$  are the length and thickness of the honeycomb beams). This cell is a pressure vessel; for a cylindrical pressure vessel, the longitudinal stress in the wall is given by the Laplace law:

$$\sigma_L = p \frac{R}{T} \tag{4-1}$$

Here  $R$  is the radius of the vessel and  $T$  is the wall thickness. In our case, as the pressure increases, the cells' volume increases while the walls become thinner according to our

choice of material Poisson's ratio ( $\nu=0.3$ ). In particular, we consider the stress state in the wall to be planar and that realistically  $\sigma_T = p \ll \sigma_L$ ; also, given the square geometry of the cell, we assume  $R = l/\sqrt{2}$  and  $T = t/2$ . With these assumptions the Laplace law gives:

$$E\varepsilon_L = p\sqrt{2} \frac{l(1+\varepsilon_L)}{t(1-\nu\varepsilon_L)} \quad 4-2$$

Which states that the walls extension in the pressurised state depends on the walls' aspect ratio, the material properties and on the internal pressure. Since in our honeycomb  $l/t \approx 10$ , we can solve the former equation as a function of the pressure. It is straightforward to verify that the wall strain increases linearly at low pressures and diverges at a finite value of pressure (Figure 4-2). This is exactly what we observe in our FE simulations at the transition from the stretching dominated regime to even higher pressures: in that case we could not find a stable equilibrium configuration past a certain value of pressure. Also, a material with  $\nu=0$  doesn't experience this instability (at least for reasonable walls strains). This means that the third regime is material (rather than structure) dependent and has to be considered in real applications.

Hence we can describe the swelling or actuation behaviour of the structure as being characterized by a bending dominated regime where the structure expands more sensitively to fluid pressure and a stretching dominated regime, where the structure is less sensitive (structural locking). When the honeycomb is fully expanded the structure is practically locked. The maximum achievable expansion depends on the geometry of the honeycomb: the more "sheared" is the initial cell shape (that is, the smaller is the honeycomb angle), the larger is the maximum expansion. Conversely, a regular lattice or a lattice with fully expanded angles (such as a rectangular one) would show no bending deformations upon pressurization, and therefore would not actuate. Therefore the relevant geometrical parameter to obtain actuation by internal pressure is the cell anisotropy and not lattice anisotropy (see equation 2-4). By cell anisotropy we refer to the property of the cell to be inscribed into a circle and is related to how "sheared" it is with respect to its topologically equivalent polygon: if the cell's corners lie on (or are close to) a circumference, the corresponding lattice won't expand upon pressurization. In the

#### 4. Results

diamond honeycomb the cell is a rhombus (which is a sheared version of a square), therefore it expands upon pressurization.

Any honeycomb, regardless of its geometry would swell isotropically if its walls do so. The importance of cell anisotropy onto the anisotropy of swelling in honeycombs has been highlighted in a recent study by Rafsanjani *et al.* [97]. They showed that in non regular hexagonal honeycombs having walls that swell anisotropically, the macroscopic swelling will be isotropic or anisotropic depending on two geometrical parameter of the cell (shape angle, and length ratio between vertical and inclined walls).

While their study confirms the same trend observed in our results (in few words, anisotropy of swelling by geometrical anisotropy of the honeycomb), the magnitude of the honeycomb swelling strains is much lower than those predicted here. Therefore, to obtain expansions that are both large and anisotropic (which is needed to consider these materials as actuators), both the honeycomb's cells shape and the swelling pressure of the phase internal to the cells are to be considered.

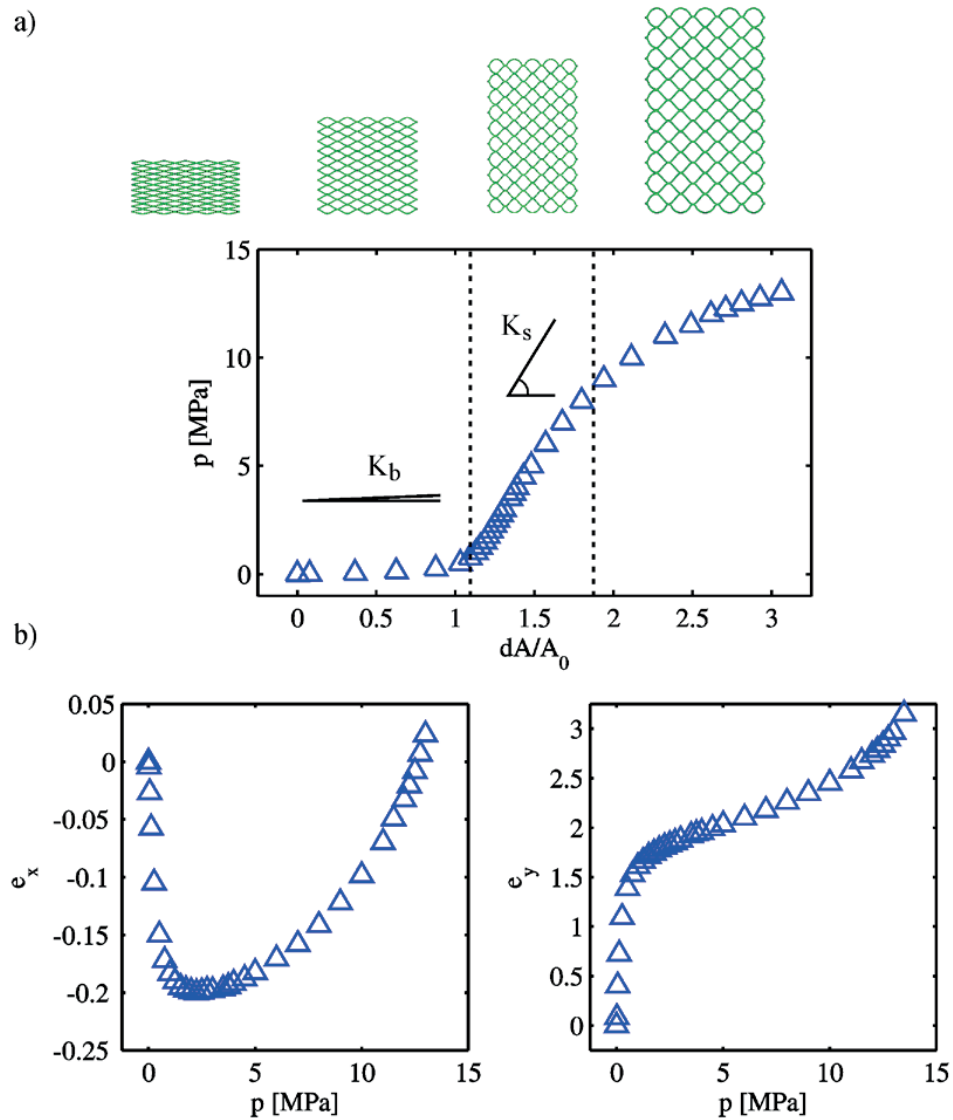


**Figure 4-1 Deformation of a diamond-shaped honeycomb with isotropic linear elastic walls ( $E=1$  GPa,  $\nu=0.3$ ) under internal pressure.**

a) Plotting the inner pressure against the area expansion three regimes are clearly visible: for low pressures, the honeycomb is characterized by a low effective bulk modulus  $K_b$  (this is the slope of the curve) dictated by walls bending and joints distortion (bending regime); at high pressures the structure is much stiffer because any further volume increase can be accommodated only by stretching the walls (stretching regime). At even higher pressures structure becomes softer again as a result of material failure (see next figure). b) These behaviours are clearly visible in the principal swelling eigenstrains: at low pressures the honeycomb shrinks in the  $x$  direction while it expands by 400% along the  $y$  direction. For  $p > 3$  both eigenstrains increase as for a stretching regime, while both strains diverge for higher pressures.

## 4. Results

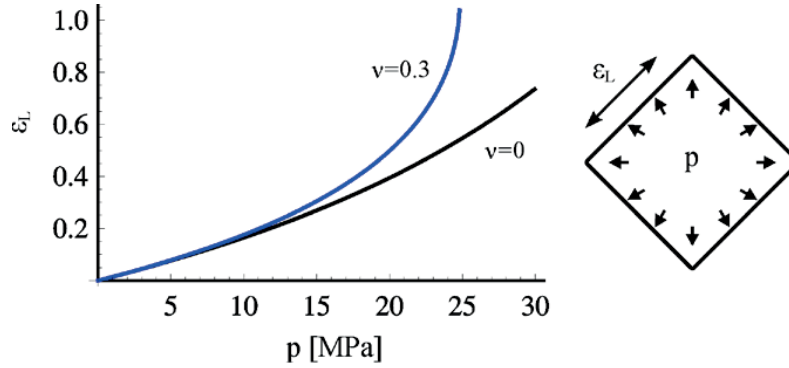


**Figure 4-2 Internal pressurization is unstable in cellular materials with material Poisson's ratio  $\nu > 0$ .** The plot shows the influence of internal pressure on walls stretching in a square vessel using a modified Laplace law that includes the effect of material Poisson's ratio. At low pressures the walls stretch linearly with the pressure. As the pressure increases, the cell volume increases while the walls get thinner due to material Poisson's ratio  $\nu > 0$ . The pressure has a positive feedback on the walls strain, which grows more than linearly. At a certain (finite) pressure the load is unbalanced and the strain diverges. As a comparison, a material with zero Poisson's ratio doesn't experience this type of unbalanced loading at least for reasonable values of strains.

### 4.1.2 Influence of fluid pressure and wall stiffness on swelling eigenstrains

The results from the parametric study are summarized in Figure 4-3 in the form of swelling eigenstrains and effective stiffness maps along the stiff ( $e_x$ ,  $C_{11}$ ) and soft axes ( $e_y$ ,  $C_{22}$ ) of the honeycomb as a function of pressure ( $p=0-9$  MPa) and wall Young modulus ( $E=1-9$  GPa). The starting geometry of the model is preserved (walls aspect ratio and honeycomb angle  $\alpha_0$  stay constant). At this level of pressure,  $e_x$  is always negative and small (some percentage shrinkage) while  $e_y$  is everywhere positive and very large (up to three-fold expansion). Both the  $e_x$  and  $e_y$  maps (Figure 4-3, top row) show a similar distribution across the parameter space: their absolute value increases from the top-left corner (stiff honeycomb walls, low internal pressure) to the bottom-right corner (high pressure and soft walls). Nonetheless, while the  $e_y$  is monotonic throughout the whole parameter space, the  $e_x$  map shows a peak that doesn't coincide with the bottom-right corner. Here, at low wall stiffness ( $\sim 1$  GPa) and high inner pressures ( $p=5$  to  $9$  MPa)  $e_x$  increases again. This behaviour derives from the deformation mechanism of the walls which is a combination of large bending at low pressures and smaller amounts of stretching at high pressures. Shifting from soft to stiffer walls allows the effect of the



inner pressure to be tuned: at low wall stiffness ( $E=1-2$  GPa), only a small pressure jump (from 0 to 2 MPa) suffices to increase the eigenstrains abruptly, whereas for higher walls moduli, this effect is much more gradual.

### ***4.1.3 Influence of fluid pressure and material stiffness on apparent honeycomb stiffness***

With apparent stiffness we intend the effective elastic modulus of the honeycomb when subjected to a load. Here we report the components of the apparent stiffness along the principal directions of loading (where subscripts 1, 2 refers to directions  $x$ ,  $y$ ). There is a monotonic (although non-linear) proportionality between the walls modulus and  $C_{11}$ ,  $C_{22}$ . Somewhat counterintuitively, a pressure increase stiffens the weak direction ( $C_{22}$  increases towards the right) but also softens the strong one ( $C_{11}$  increases towards the left). Generally, a pressure acting inside the cells would be expected to stiffen the structure, in contrast to what is observed here for  $C_{11}$ .

In reality the apparent stiffness is a structural property: it doesn't depend on the material properties

It is possible that this is geometry-related: the effect of the pressure is to deform the honeycomb, thus rotating almost axially oriented walls away from the  $x$ -axis, which would have the effect that the walls are loaded more in bending than axially.

The idea that the apparent stiffness changes in accordance to the structural modifications will be investigated more thoroughly in the next section (4.2) by means of the micromechanical model.

## 4. Results

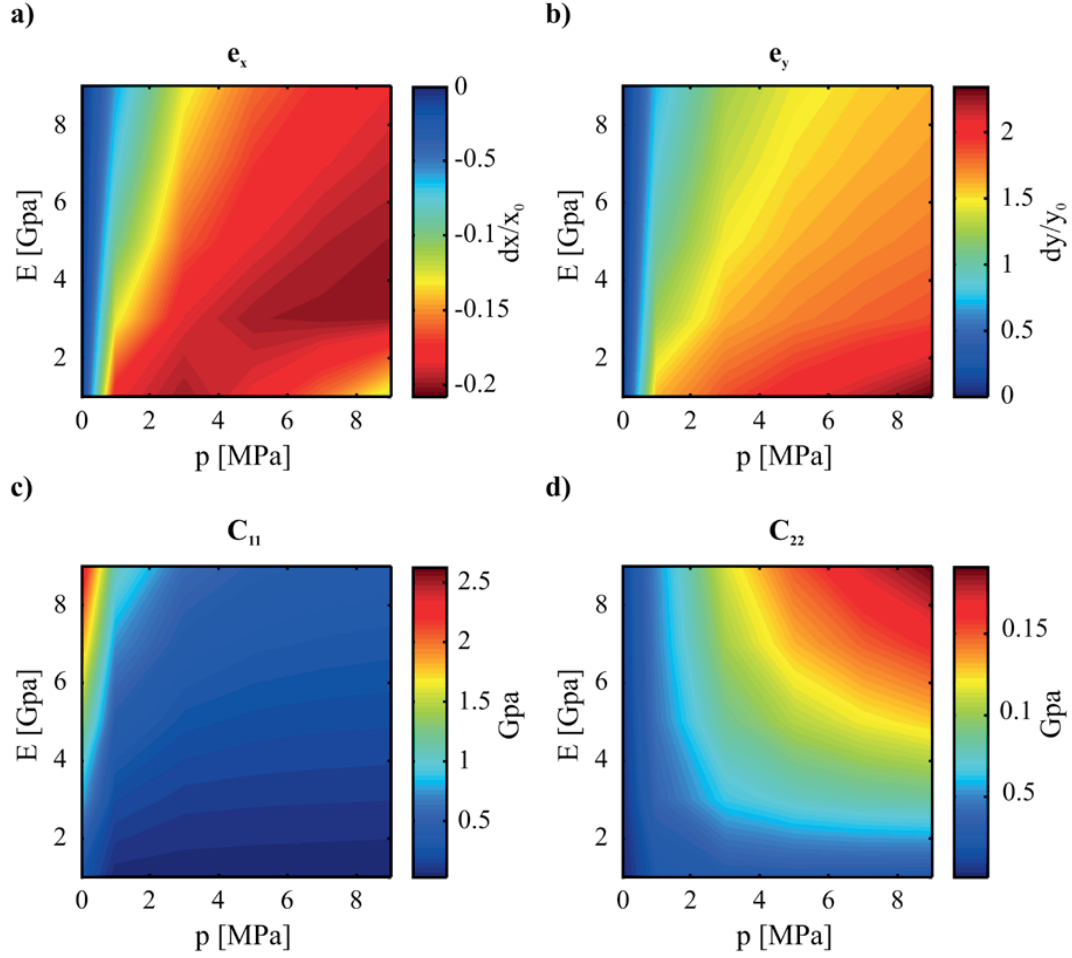


**Figure 4-3 Eigenstrains and effective stiffness maps.**

Swelling eigenstrains (top) and principal stiffness (bottom) along the honeycomb weak (right) and strong (left) directions, as function of internal pressure (in MPa) and wall's Young modulus (in GPa). Stiffness colour bar in GPa. Swelling eigenstrains generally increase going from stiff honeycomb walls and low internal pressure to high pressure and soft walls. The effect of pressure on stiffness is twofold, since it stiffens the weak direction and softens the strong direction, as a possible consequence of the pressure-related shape change of the honeycomb.

### 4.2 Micromechanical analysis of diamond honeycombs

In order to understand in more detail the fundamental deformation mechanisms of the swellable honeycombs, we now analyze the simpler micromechanical model presented in section 3.1.5. Therefore the micromechanical model predictions of the swelling eigenstrains and effective stiffness will be compared with those from the FE simulations shown in the section 4.1

#### 4. Results

The aim of this section is to present an analytical model that is able to describe the actuation behaviour of pressurized lattices both in terms of swelling eigenstrains and effective stiffness, using simple geometrical information related to the lattices' microstructure. In simple cases such as the diamond honeycomb, lattice points and structural joints coincide (see Figure 3-1 c) and the parallel between the micromechanical and finite element models can be easily traced. In the following, we will present our modelling strategy applied to the case of the diamond honeycomb: nonetheless, the method is general enough to be transferred to more complex 2D geometries.

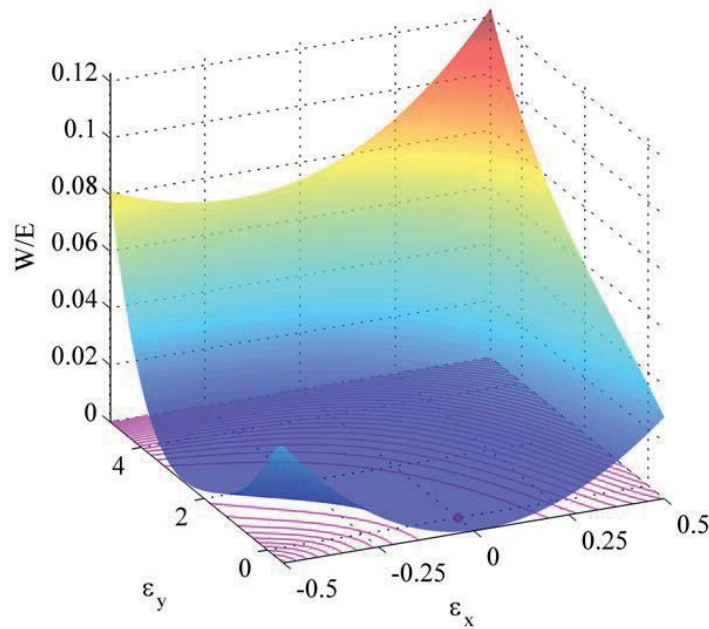


**Figure 4-4 Lattice energy landscape under biaxial deformation and unpressurised condition.**

*The strain energy density is normalized by the value of the wall stiffness  $E$ . The isoclines (in magenta) are spaced by  $4 \cdot E \cdot 10^{-3}$ . Input strains  $\epsilon_x$  spans the range  $[-0.5, 0.5]$ , whereas  $\epsilon_y$   $[-0.5, 5]$ . The steepest direction corresponds to a volumetric deformation of the lattice, while the shallowest (narrow valley) to a deviatoric one (this is when pure shearing of the diamond cell happens).*

The internal fluid-structure potential (or strain energy density) is plotted in Figure 4-4 as a function of the principal strains  $\epsilon_x, \epsilon_y$ , (mapping  $(\alpha, \epsilon) \rightarrow (\epsilon_x, \epsilon_y)$ ). Here the internal

## 4. Results

pressure is set to zero. For convenience, the strain energy density is normalized by the value of wall stiffness  $E$  and  $\epsilon_y \in [-0.5, 5]$  spans a broader range than  $\epsilon_x \in [-0.5, 0.5]$  since this is the weaker direction. As expected, the steepest path runs across the first and third quadrant where a biaxial deformation ( $(\epsilon_x > 0, \epsilon_y > 0)$  and  $(\epsilon_x < 0, \epsilon_y < 0)$ ) causes the lattice beams to deform axially, corresponding to a volumetric deformation of the lattice. Conversely, the lowest isoclines are found for  $(\epsilon_x < 0, \epsilon_y > 0)$  a pure deviatoric deformation of the lattice is expected. In the narrow valley the energy minimum is found (for  $\epsilon_x = 0, \epsilon_y = 0$ ).

### 4.2.1 Strain energy density and swelling eigenstrains

Upon pressurizing the system the strain energy density “landscape” changes considerably. In Figure 4-5 the strain energy contours are reported for increasing values of the normalized internal pressure  $p^*$  (where, again, the fluid pressure is normalized by the wall Young modulus:  $p^* = p/E \cdot 10^3$ ).

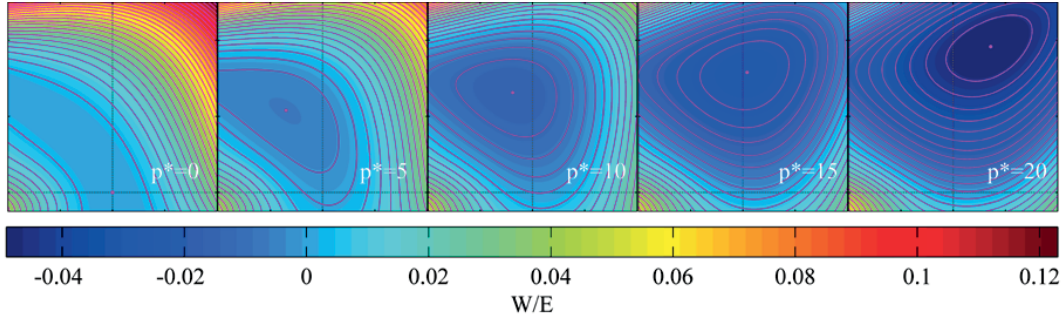


**Figure 4-5 Lattice energy evolution for increasing pressure.**

Colour maps of the lattice strain energy density normalized by the walls modulus  $E$  for input strains  $\epsilon_x \in [-0.5, 0.5]$ ,  $\epsilon_y \in [-0.5, 5]$ , as the pressure increases (left to right). In each box, neighbouring isoclines are spaced by a value  $4 \cdot E^{-3}$ .

There are two effects that can be observed. Firstly, the energy minimum migrates from the left area ( $\epsilon_x < 0, \epsilon_y > 0$ ) to the upper right area ( $\epsilon_x > 0, \epsilon_y > 0$ ) of the deformation space. The minimum coordinates in each plot are the swelling eigenstrains as the lattice goes from the unloaded (leftmost panel) to increasingly pressurised states (to the right). These eigenstrains compare well with the swelling eigenstrains calculated in the finite element

simulations (Figure 4-7). Secondly, the shape of the isoclines changes from an arc to a closed rounded one, which is a hint for a structural transformation of the system. This is confirmed by the angular deformation of the lattice for increasing normalized pressures (Figure 4-6), where the lattice angle approaches  $90^\circ$ .

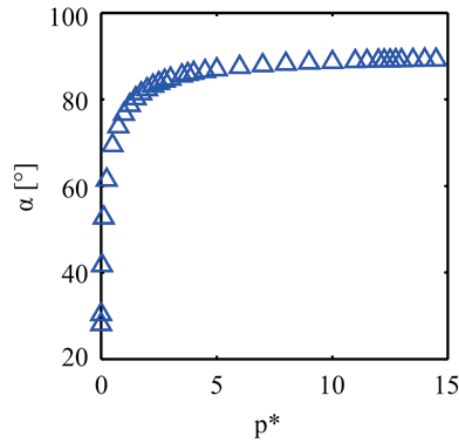


**Figure 4-6 Lattice angle  $\alpha$  for increasing normalized pressure  $p^*$ .**

*Normalized parameters describing deformation ( $\alpha$ ) and loading ( $p^*$ ) of the pressurised lattice clearly show the bending dominated ( $p^* < 2$ ) and stretching dominated ( $p^* > 3$ ) regimes observed in the FE model.*

#### 4.2.2 Lattice apparent stiffness

Considering several values of fluid pressure and walls' Young modulus, maps similar to those of Figure 4-3 can be created. For clarity, each tensor component is normalized by the material stiffness  $E$  ( $C_{aa}^* = C_{aa} / E$ ) and presented as function of normalized pressure  $p^*$  (Figure 4-7): by doing this, all data collapse onto a single master curve.

Tensorial quantities in Figure 4-7 are calculated by evaluating equation 3-16 with finite differences. Their "true" value is found for an infinitesimal probing strain ( $\epsilon_x, \epsilon_y, \gamma_{xy}$ ). Given the non linearity of  $W$ , a finite probing strain will influence the stiffness components. Moreover, in the case of  $p \neq 0$ , the sign of a direct probing strain  $\epsilon_x, \epsilon_y$  is expected to influence the value of the stiffness, since the pressure term will give a positive or negative volumetric contribution to  $W$  when  $\epsilon_x, \epsilon_y$  are respectively negative or positive (that is, decreasing or increasing the volume). Hence, the stiffness tensor components reported in Figure 4-7 are evaluated at the pressurised state ( $\alpha_p, \epsilon_p$ ) of the

#### 4. Results

Born lattice applying the same probing strain  $\varepsilon_x=\varepsilon_y=1\%$  used for the FE parametric study. This is important to emphasize, since the strain energy density  $W$  depends on the configuration chosen as the reference. As a side remark, we imagine to probe the pressurised lattice in the undeformed configuration ( $\alpha=\alpha_0$ ,  $\varepsilon=0$ ). In this case, since the undeformed state is not the equilibrium state, an extensional (positive) probing strain could produce a negative stress, and hence give rise to an unphysical negative stiffness. This virtual experiment is not consistent with the definition of stiffness, which requires that the stiffness be calculated from the equilibrium reference state. On the contrary, such a situation will be considered in the assessment of the stress generated by a pressurised lattice producing mechanical work against an external load (paragraph 4.2.3).

From the master curves, there is a good qualitative agreement between the FE and Born model for the whole extent of the parametric space considered. The  $C_{11}$  component experiences a rapid decay for a slight increase of  $p^*$ . At the same time the  $C_{22}$  component increases many fold. This is due to the process already described: as the pressure increases, the lattice switches rapidly to a more isotropic geometry (Figure 4-6), strengthening the soft direction  $y$  at the expense of the  $x$  direction. Nonetheless this effect is not uniform: at  $p/E=2$ ,  $C_{11}$  decreases to one tenth of its unpressurised value, while  $C_{22}$  becomes as high as 25 times its original value. At higher pressures ( $p>5$  MPa), when the lattice approaches a square geometry, all components of the stiffness tensor show a slight decrease for increasing pressure. Since the lattice geometry doesn't change sensitively under higher pressures, we conclude that the observed softening effect is due to the fluid pressure. Indeed, as the probing strain is extensional, the volume available to the fluid phase increases and the fluid expands more easily. The  $C_{66}$  component evidences a poor agreement between the two models. This is not too surprising, since the parameterization of the polynomials  $c_1$  and  $c_2$  implies only relative displacement between the joints (paragraph 3.2.2). To improve the prediction for the  $C_{66}$  component one could introduce a localized joint rotation as an additional microstructural parameter.

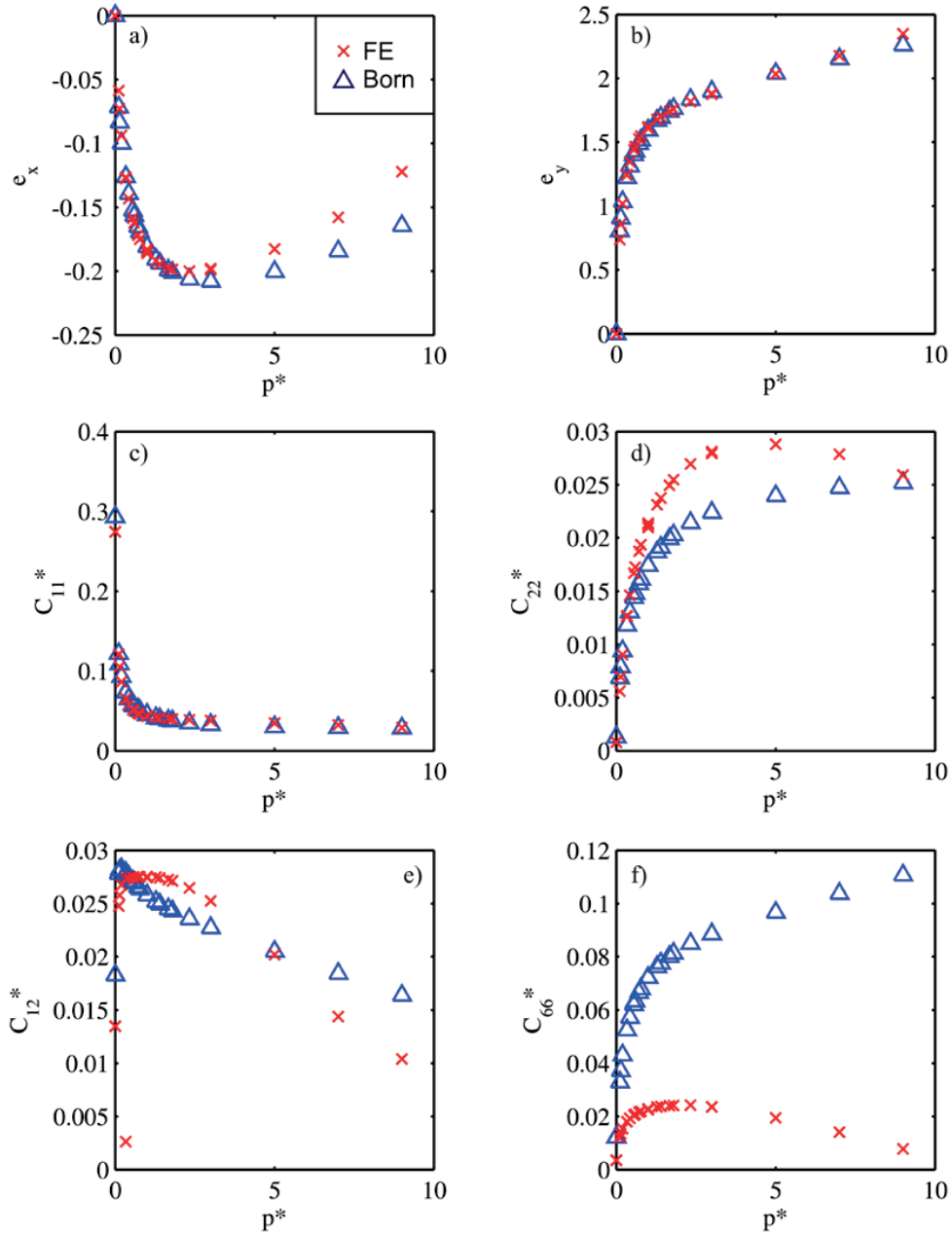


**Figure 4-7 Eigenstrains and stiffness master curves: comparison between FE and Born lattice model.** Swelling eigenstrains and effective stiffness as a function of reduced pressure  $p^*$ . Stiffness components are normalized by modulus  $E$ . The components of the apparent stiffness tensor vary according to the two stage behaviour. In particular the honeycomb becomes softer along the  $x$  direction and stiffer along the  $y$  direction as a result to the change in geometry occurring upon pressurization. Also, it can be seen that Born model follows very well the FE simulations, with a major exception in the case of  $C_{66}$  where localised joint rotations become more important.

## 4. Results

This is equivalent to move from a classical continuum mechanics theory (where the strain state depends only on the displacement from the reference to the deformed configuration) to a Cosserat continuum theory (where the strain state depends also on microscopic rotations) [26]. This is beyond the scope of the present analysis as we wanted to investigate the swelling and elastic properties of the lattice by introducing only parameters that are directly related to its geometry or material properties, but has to be kept in mind if one wants to obtain more accurate results.

### 4.2.3 Honeycomb based actuator

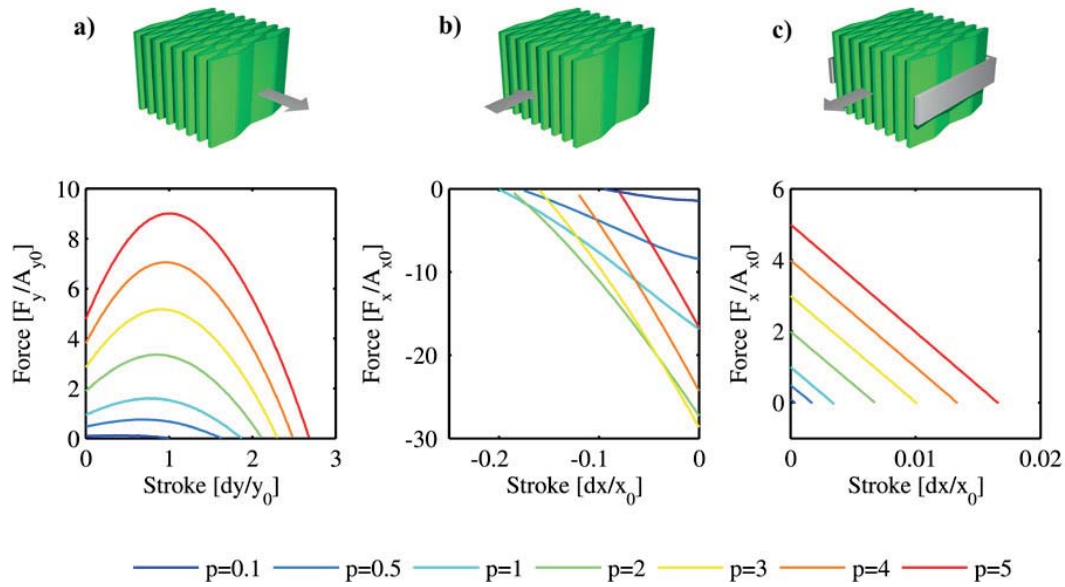


**Figure 4-8 Working configurations and force developed by a honeycomb actuator.**

A pressurised honeycomb can be used as a linear actuator to displace an external load. At least three configurations can be thought of: a) applying a moderate pushing force at high strokes; b) applying a high pulling force at low strokes; c) applying a low pushing force at very low strokes. Three graphs (bottom) show the working characteristics for different pressures fed in the honeycomb.

Figure 4-8 shows the performance characteristics of the pressurized honeycomb described earlier ( $\alpha_0=28^\circ$ ,  $l/t>10$ ,  $E=1\text{GPa}$ ) when used as an actuator. Reported is the force exerted as function of the stroke (i.e. actuation stress versus strains) for several



#### 4. Results

values of the pressure fed in the system. Following Zupan [98] we describe the actuator performance in terms of two complementary normalized attributes. The maximum stroke divided by the actuator length parallel to this stroke is the actuator strain (or normalized stroke), and the maximum generated force divided by its cross section perpendicular to the stroke is the actuator stress (or normalized force). In this honeycomb actuator the energy required to produce mechanical work is stored in the fluid. An external compressor is ideally connected to the volume enclosed by the honeycomb walls and a flexible membrane sealing the top and bottom surfaces (not shown). In Figure 4-8a, b two working configurations of the honeycomb actuator are depicted, where it is respectively used to produce force along the y and the x direction. In both cases the transversal direction is free to deform. In the third configuration (Figure 4-8c), the actuator is generating force along the x direction, being constrained along the y direction. Each graph represents a family of curves depicting the output stress at different pressure input: the actuator performance changes drastically at different levels of energy source. As expected, the maximum stroke (where the performance curve meets the zero stress output) coincides with the actuation eigenstrains.

Interestingly, the force output along the weak direction y is non monotonic with the stroke. Obviously it starts from a zero-stroke value close to the set value of the pressure (which measures the amount of energy fed in the system) but, as the stroke increases, it firstly increases to an upper limit and then decreases till eventually it reaches zero. The stress produced is bigger than the pressure input into the system. This is not contradictory in itself, but is a sign that the actuator works in different configurations as the stroke changes. At low strokes ( $dy/y_0 < 1$ ) the expanding fluid has to overcome just a small energy barrier (walls bending). The fluid volume increases but since the pressure is constant, the total energy available to produce mechanical work increases with the stroke. At higher strokes the honeycomb walls start deforming in stretching, hence the energy cost is higher and the force generated lower, till it eventually reaches zero. In this configuration the system capitalizes on the big angular deformation of the walls to produce high strains at moderate stresses.

Conversely, when the actuator is used to produce force along the strong direction x (Figure 4-8, b), the stress output is high and the strokes are low. More importantly the

## 4. Results

stress generated is negative: the actuator “pulls”. Moreover, unlikely the force output along the weak direction  $y$ , increasing the input pressure doesn’t always mean a higher tensile stress. At a certain pressure ( $p > 2$  here) the stretching of the walls becomes significant and partially compensates the contraction along  $x$  due to angle opening. Hence the actuator can be fine tuned, to produce different tensile stresses at several strokes.

Constraining the  $y$  direction (fig 12, c), causes the actuator to produce a compressive stress, which is smaller, in absolute terms, than in the unconstrained case: since the honeycomb angle cannot open, the only possible deformation mechanism is due to walls stretching, which is rather energetically costly. Here the actuator works in a low strain - low stress fashion. Such a behaviour is reminiscent of the lever-arm principle used by wood cells to generate tensile or compressive stresses [43]: if the microfibril angle (equivalent to half of the honeycomb angle here) is less than  $45^\circ$  the only way to swell the cell is to shorten it along the longitudinal direction (the strong direction here).

### 4.2.4 Tuneable Poisson’s ratio material

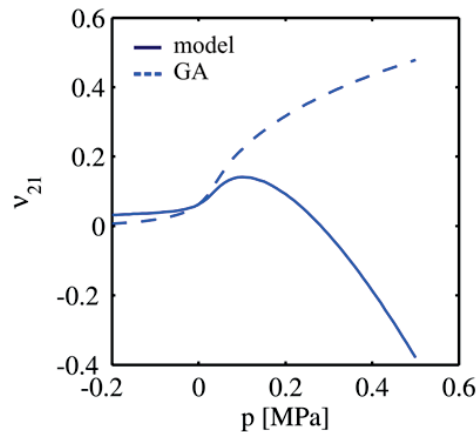


**Figure 4-9 Poisson’s ratio as function of inner pressure for walls with  $E=1\text{GPa}$ .**

*The effect of the pressure on the honeycomb Poisson’s ratio is twofold: a pure structural effect due to a varying honeycomb angle (Gibson-Ashby prediction, dotted line) would give  $v$  tending to unity for increasing pressures, whereas a transverse expansion caused by the pressurising fluid soon causes  $v$  to diverge to negative values.*

As seen, the material properties of an anisotropic cellular material vary strongly with the internal pressure it is subjected to. In particular the pressure has two separate effects: the substantial change in material's geometry (structural effect) and the intrinsic pressure contribution to the load-bearing capacity of the material (fluid-related effect).

Figure 4-9 shows the dependency of the Poisson's ratio  $\nu_{21}$  at several values of inner pressure. The value predicted by the Gibson-Ashby model [68] (Figure 4-9, dotted line) depends only on the actual geometry ( $\alpha_p$  is honeycomb angle in the pressurised state) and acts as a reference to disentangle the pure structural from the fluid-related contribution:

$$\nu_{21} = \frac{\sin^2\left(\frac{\alpha_p}{2}\right)}{\cos^2\left(\frac{\alpha_p}{2}\right)} \quad 4-3$$

As the pressure increases  $\alpha_p$  becomes larger (see fig 10) and  $\nu_{21}$  quickly tends to unity. The full line shows the prediction given by the pressurised honeycomb model subjected to a strain  $\varepsilon_2=1\%$ . Obviously the two curves coincide at  $p=0$ , and are close for small values of pressure. Our model predicts larger values at negative pressures. At positive pressures however, it diverges to even negative values. As the applied probing deformation is positive, the available volume in the honeycomb increases and the fluid (which is kept at constant pressure) expands also in the transverse direction. As a result the sign of the Poisson's ratio becomes negative. This effect is qualitatively similar to the positive cross-sectional strains that a polymer immersed in a fluid experiences when it gets axially stretched [99].

At all effects a pressurizing fluid put in the honeycomb can act as a free parameter to drastically change its effective Poisson's ratio. This might be a rather convenient way to get materials with very high shear modulus (ideally infinite for  $\nu=-1$ ).

### 4.3 Role of architecture in the expansion of non-convex lattices

In the former two sections we have shown that the actuation behaviour of a diamond-shaped honeycomb subjected to internal pressure depends on its geometrical anisotropy (represented by the lattice angle  $\alpha$ ). Anisotropic cells undergo large expansions upon

## 4. Results

pressurization because they deform like a freely jointed mechanism so that a corresponding isotropic shape is obtained (squares in the case of a diamond honeycomb). Similarly, a non-convex polygon too will experience large expansions when pressurized. Therefore, a natural question arises whether and under which conditions lattices based on non-convex cells will also experience large expansions upon pressurization. Since these cells are non-convex, there are many ways to pack them together to obtain a planar lattice: the resulting lattices will differ in terms of their architecture. In this section our aim is to present the expansion behaviour of several designs of lattices, based on two non-convex cells, in order to identify the geometrical and topological criteria that characterize their actuation.

### ***4.3.1 Two-scale deformation of non-convex lattices***

In this section we present the typical deformation patterns of the non-convex lattices. A detailed description will only be given of the expansion one prototypical lattice; these observations apply (with some due differences) also to the other lattices investigated, as can be seen in the corresponding figures in paragraph 4.3.2. Like the diamond shaped honeycomb, all lattices considered here are bending dominated and therefore they can undergo large deformations upon pressurization.

In Figure 4-10, four snapshots of the L1 lattice are presented as it expands. At the microscopic level (the cells level), the lattice deforms by the same mechanisms acting in the diamond honeycomb. At low pressures the lattice deforms by walls bending and joints distortion. At higher pressures, when the internal angles meeting in a vertex reach a final value, the lattice expands only by walls stretching. In the fully stretched state the originally non-convex L-shaped cells have transformed into hexagons; this is in accordance with one's intuition that a convex polygon maximizes its area compared with a non-convex one with the same perimeter.

At the macroscopic level instead, the deformation is quite different. In the diamond honeycomb, the macroscopic deformation was simply undistinguishable from the microscopic one; apparently, this is not the case here: deformations at the cell level and

those of the whole lattice are not affine (a simple prove of this is found by looking at the lattice contour: from straight lines it changes to a wavy pattern).

In random cellular materials microscopic deformations are averaged out by the random structure and the material is isotropic. This is also the reason why, the apparent stiffness of a random cellular material depends on “global” quantity such as relative density (equation 2-6), and it is not necessary to resolve the deformation of each single cell to estimate it. In the non-convex lattices presented here however the regularity of the architecture ensures that microscopic deformations are preserved throughout the macroscopic scale. Therefore the different lattice architectures will produce different microscopic patterns and macroscopic deformations which will be in general anisotropic (unlikely to random lattices): these aspects will be tackled in paragraphs 4.3.2 and 4.3.3. In particular, since all lattices are based on the same cell, the different expansion behaviours will depend only on the architecture that is on cell convexity and lattice connectivity (see equations 2-5 and 2-1): the physical mechanisms responsible for these trends are given in paragraphs 4.3.4 and 4.3.5. Finally, as the microstructure changes upon pressurization, also the apparent stiffness will change (see paragraph 4.3.6).

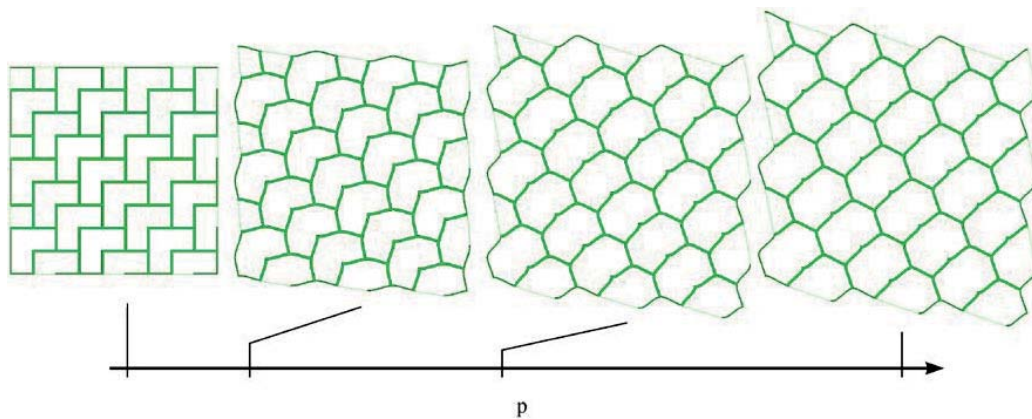


**Figure 4-10 Two levels of deformation in a non-convex lattice upon pressurization (lattice L1).**

*At the microscopic level, the L1 lattice expands similarly to what observed in the diamond honeycomb, that is, by walls bending and joints distortion at low pressures and by walls stretching at higher pressures. At the macroscopic level the lattice can undergo principal deformations and shearing. Also, microscopic and macroscopic deformations are not affine (the lattice contour changes from straight lines to a wavy pattern). In general the macroscopic deformation is an “average” of the deformation of the single cells: in the case of these periodic non-convex lattices the microscopic strain translates to the macro level in many ways creating a number of different strain patterns that depend on the lattice architecture.*

## 4. Results

### ***4.3.2 Microscopic patterns and macroscopic deformations of non-convex lattices***

As for lattice L1, also the remaining non-convex lattices show both microscopic and macroscopic deformations which are peculiar for each architecture: we now introduce them with the help of figures that show the undeformed and fully pressurised configurations of each lattice.

First of all, lattices L2, L3, L4 (Figure 4-12) show only minor deformation upon pressurization although they are non rigid in the definition provided in paragraph 2.2.2 (see also Figure 2-4). Here the bending deformation and joint distortion needed to expand the cells are prevented because these mechanisms are impeded by the lattice periodicity: so, while still being bending dominated structures, (that is they non-rigid in terms of the Maxwell criteria) they expand only by stretching of the beams. Since they don't undergo any significant deformation, these lattices will be discarded in the remainder of the discussion.

In lattice T5 (Figure 4-13) instead the walls are free to bend and individual cells maximize their area assuming a convex shape; at the macroscopic level, this corresponds to a huge extension in the horizontal direction and almost no deformation along the vertical one.

Lattices T1 and T3 (Figure 4-11) undergo the same biaxial macroscopic expansion, which is more pronounced in direction  $x$  than  $y$ . Remarkably, at the microscopic level, there is a well defined alternated motion of the vertical walls, which confers a sort of microscopic zigzag pattern: moreover, while in lattice T1 the vertical walls move downwards, in lattice T3 the vertical walls move both downwards and upwards, which increases the amplitude of the zigzag pattern. Also, since in its pressurised state some walls align horizontally we expect that the lattice becomes stiffer along the horizontal direction (structural locking).

Lattices T2, T4, T5, T7 (Figure 4-15) show as well a microscopic zigzag pattern with biaxial macroscopic expansion. In these cases the relative stiffness of the lattices along the vertical direction will be lower than in the previous case as rows of vertical walls become inclined in the pressurised configuration (hence resisting by bending instead of

compression). Lattice T4 assumes a hexagonal structure in the pressurised state which confers even lower rigidity to the lattice in the pressurised configuration.

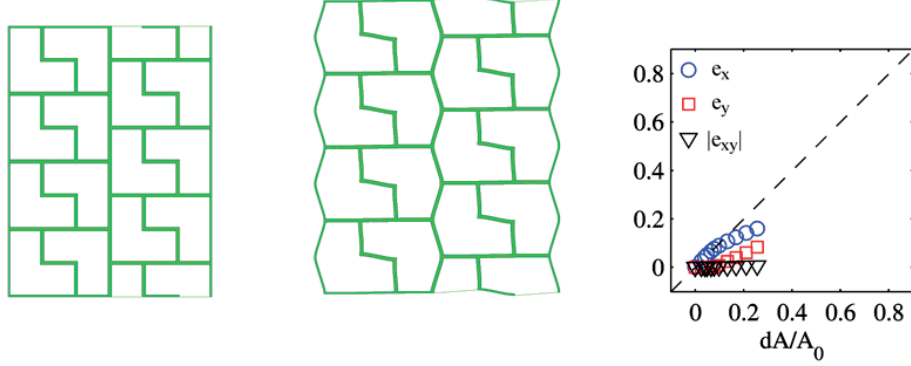
Upon pressurization lattices T8, T9, T10 (Figure 4-16) show a similar macroscopic shearing deformation: in the pressurised configuration though, the mechanical properties will be different as the walls align in different directions.

Lattices L6 and L7 experience an isotropic macroscopic deformation despite the uneven transformation of the individual cells.

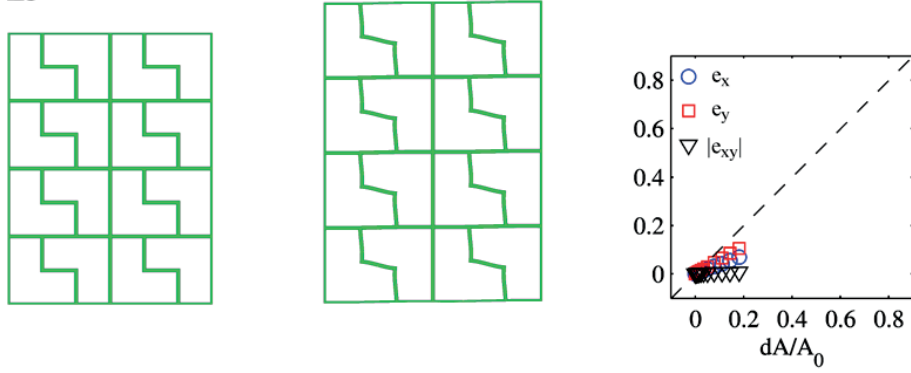
In all these lattices (L6, L7, T6 and T11) the drastic change in microstructure geometry could be exploited for purposes other than mechanical actuation: depending on their size one could think of sieves for sorting objects or filters that create tuneable interference patterns.

## 4. Results

### L2



### L3



### L4

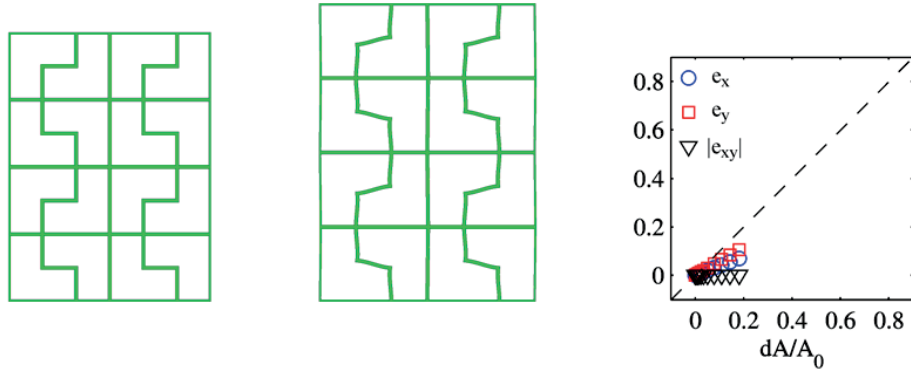


**Figure 4-11 Lattices without periodic mechanisms don't experience major deformations (L2, L3, L4).** In these lattices, substantial joint distortion upon pressurization is impeded because this would cause an expansion of a cell at the expense of the neighbouring ones. Since all cells have equal area, this doesn't happen: instead a minor expansion due to beams stretching is observed. The plots at the right show the "trajectories" of principal ( $e_x$  and  $e_y$ ) and shear ( $e_{xy}$ ) strains with respect to the total area strain at each level of pressure. The sum of the principal strains equals the area strain. A principal strain close to the bisector line individuates lattices that deform mainly along that direction (see Figure 4-13), whereas lattices that deform isotropically have almost coincident points for  $e_x$  and  $e_y$  (see Figure 4-17).



L5

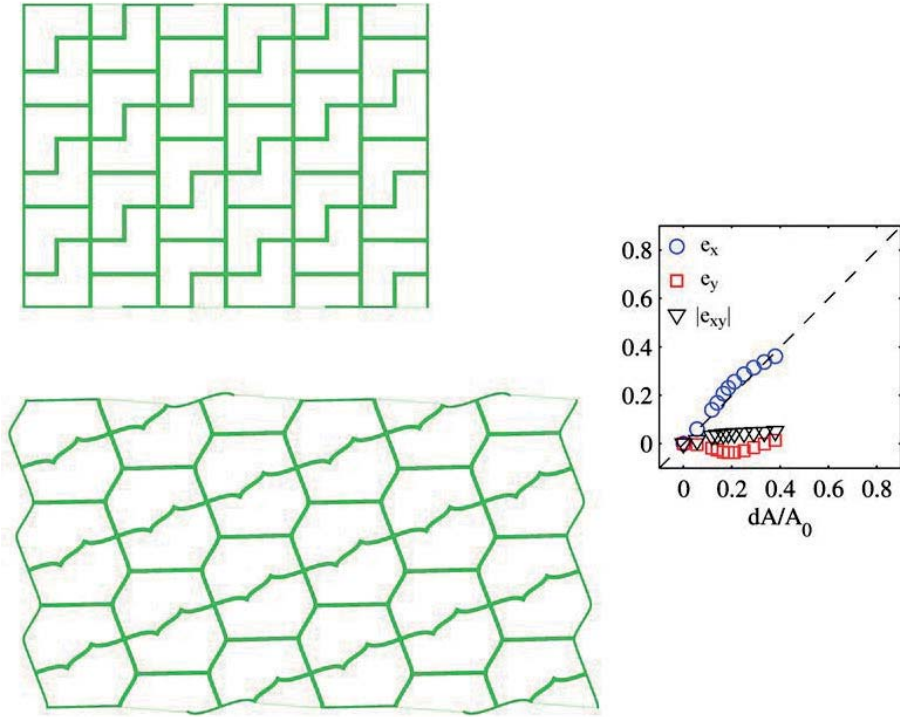


**Figure 4-12 Macroscopic uniaxial “thruster” deforms along direction x with almost no vertical deformation (L5).**

*This design maximizes the macroscopic deformation of the lattice along one direction, while keeping the structure flexible (no structural locking by horizontal or vertical struts).*

## 4. Results

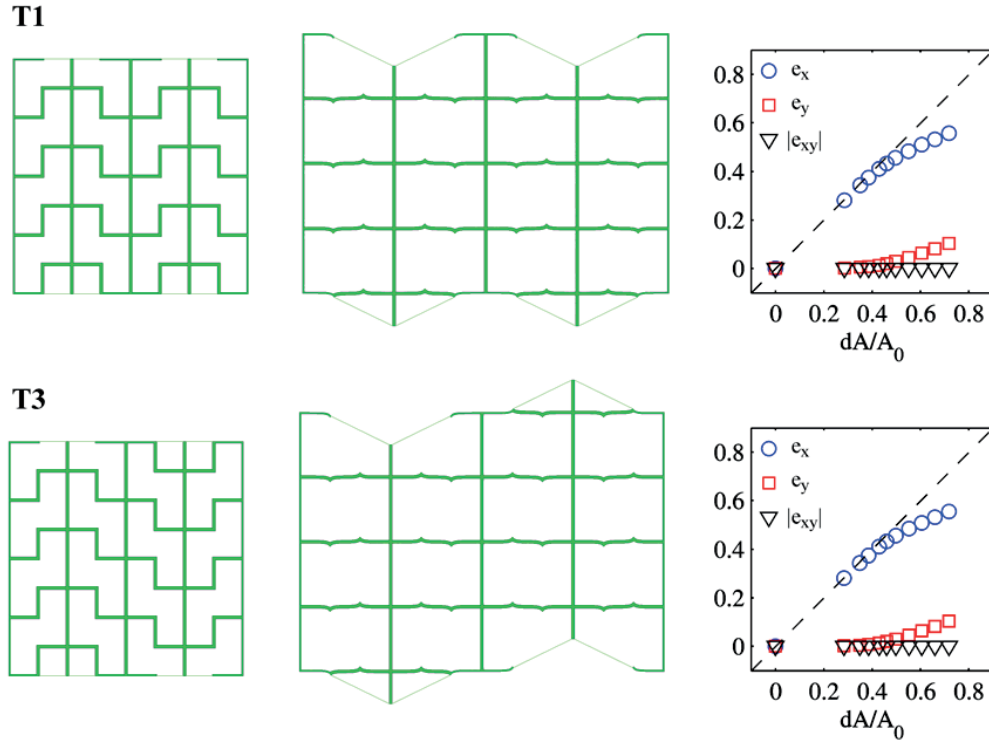


**Figure 4-13 Microscopic one way (T1) and two ways (T3) “zigzagger” with macroscopic extension and structural locking.**

*Although the single cells shear upon pressurization there is no macroscopic shearing of the whole lattice due to the presence of reflection (T2) or glide (T4, T5) symmetries, or both (T7) so that the local shearing is balanced. This gives rise to a type of lattice that we dub “zigzagger”. In these lattices an alternated vertical motion is observed at the microscopic level, together with a macroscopic horizontal expansion. The vertical motion can point upwards or downwards depending on the cells arrangement. In its pressurised state the lattice is very stiff due to vertical and horizontal alignment of the beams (structural locking).*

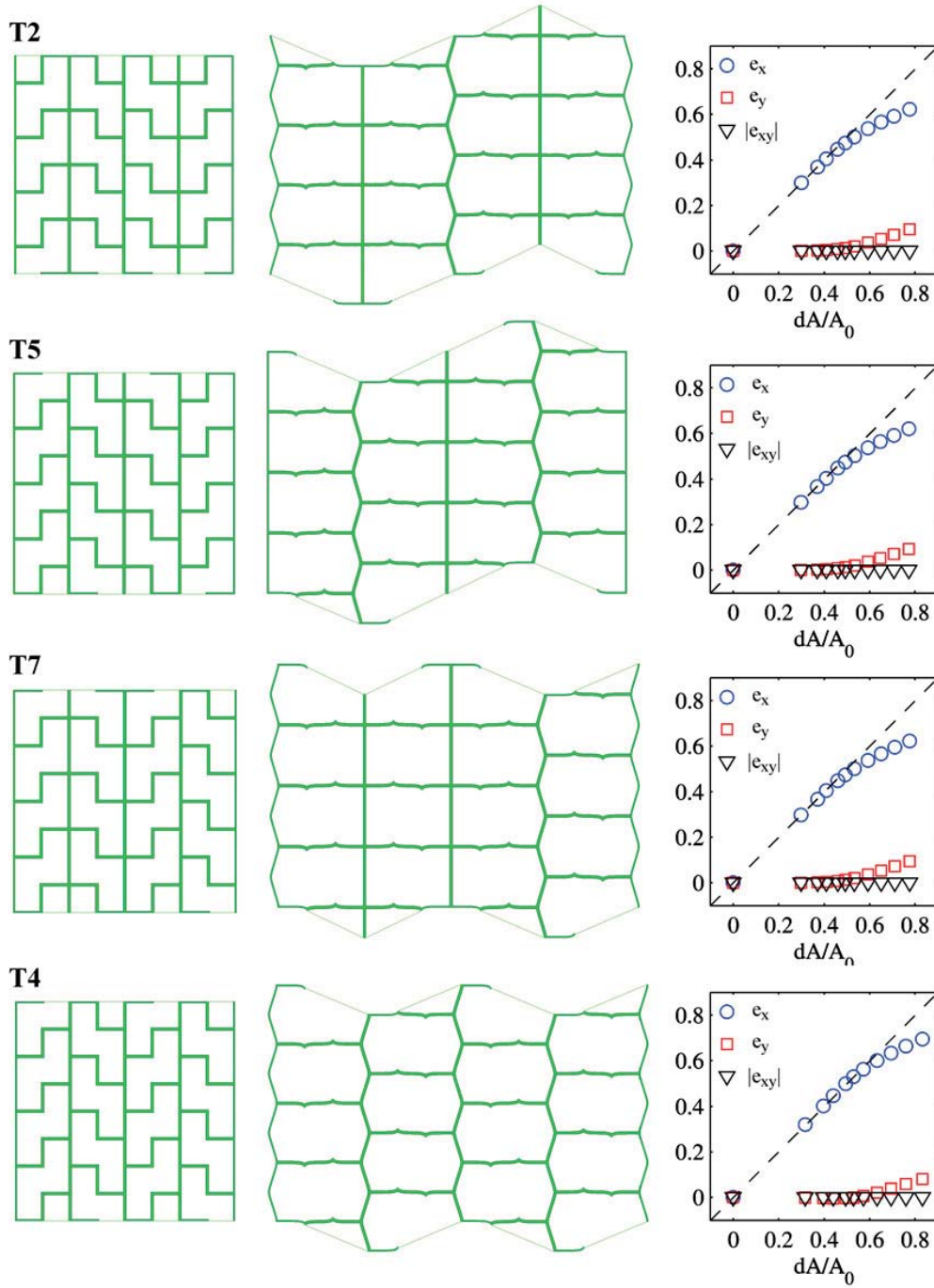


**Figure 4-14** Several implementations of “zigzagger” with stiff (T2, T5, T7) and “soft” structures (T4). These “zigzagger” will be less rigid along the principal directions than the previous ones (Figure 4-11) as the beams are inclined.

#### 4. Results

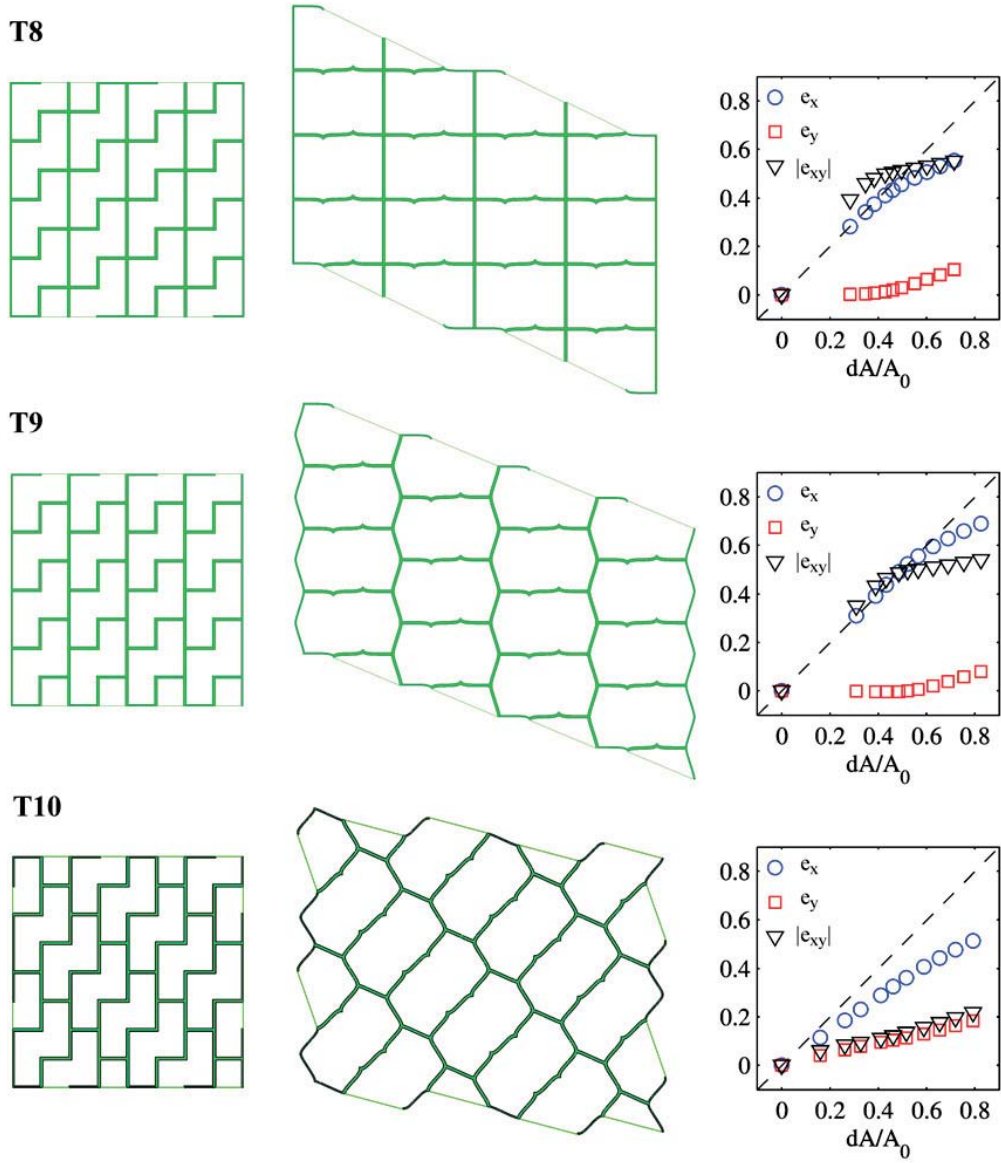


**Figure 4-15 Lattices actuating by shearing with variable stiffness.**

*These lattices show macroscopic shearing upon pressurization because they lack reflection symmetries. From above, lattices T8 and T9 deform almost identically but they show very different stiffness: T8 is always rigid along  $y$  and stiffens along  $x$ ; T9 becomes more isotropic and less rigid along  $y$ ; lattice T10 instead becomes more rigid along the  $45^\circ$  direction along which the beams align.*

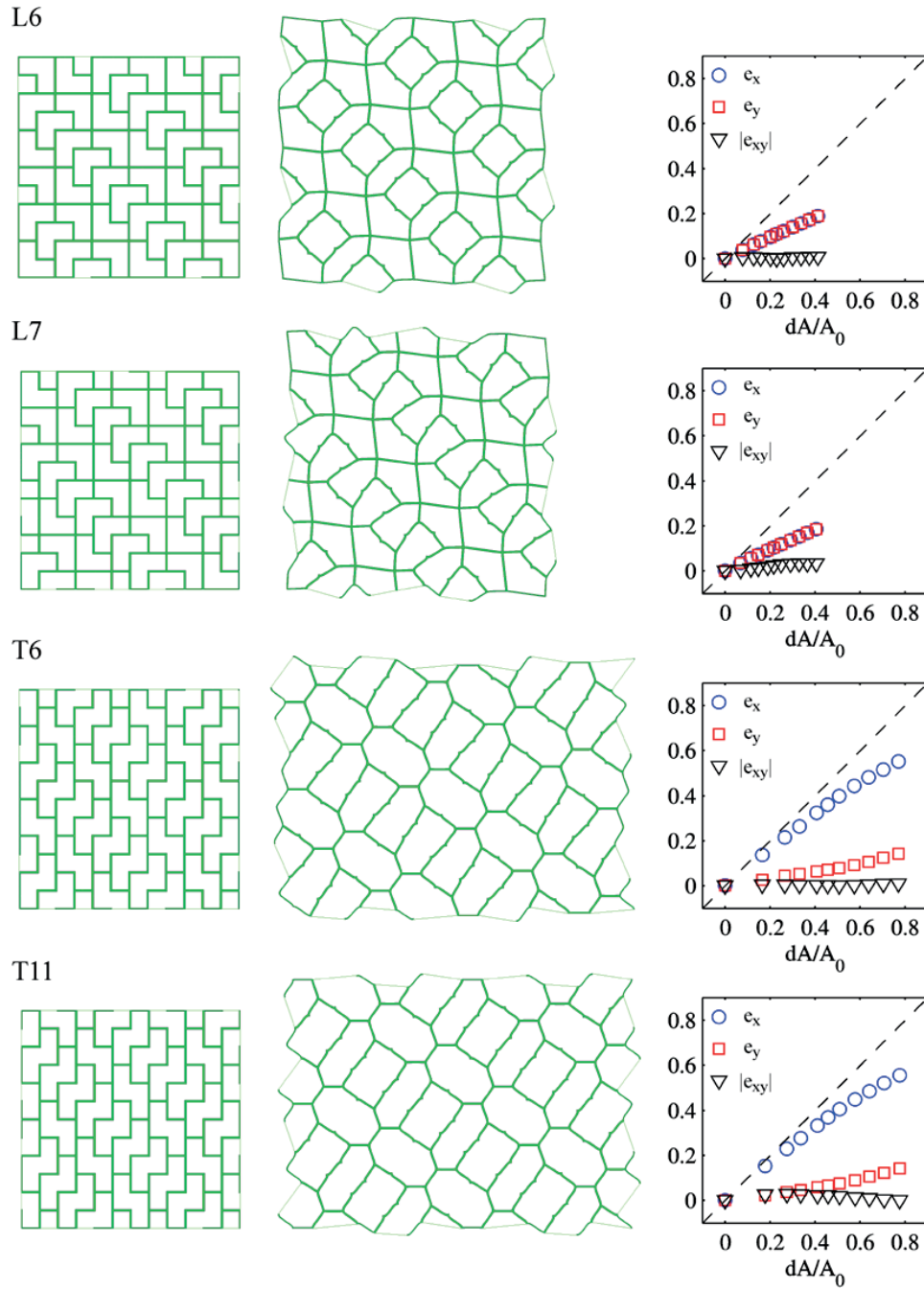


**Figure 4-16 Non-convex lattices with multiple-cell periodic unit (L6, L7, T6, T11).**

Even if based on a single cell, some non-convex lattices acquire a more complex microstructure in the inflated state, where the cells assume several polygonal shapes. The drastic change in microstructure geometry could be exploited for purposes other than mechanical actuation: one could think of sieves for sorting objects or tuneable light filters that create several interference patterns. Moreover the macroscopic expansion behaviour can be intrinsically isotropic (as in L6 and L7) or anisotropic (as in T6 and T11).

## 4. Results

### ***4.3.3 Generation of macroscopic anisotropy and shearing expansions***

As we have qualitatively shown in the former paragraph, the expansion eigenstrains of most of the lattices are anisotropic: these are plotted as function of internal pressure in Figure 4-18 and the ratio between the two principal deformations are given as function of pressure in Figure 4-19. Similarly to the diamond honeycombs, almost all lattices expand preferentially in one direction (direction  $x$ ) while in the other direction the expansion is only marginal. This doesn't apply, again, to "locked" lattices with any periodic mechanisms (L2, L3, L4) which deform by stretching and hence experience isotropic deformations.

Major shearing upon pressurisation is present only in few cases (L1, T8, T9, T10). This is quite remarkable, since microscopic shearing of the individual cells is expected for such irregular cells. Therefore the absence of macroscopic shearing is due to the architecture of these lattices. To be more precise, "balanced", non shearing, lattices have reflection symmetry planes coinciding with the lattice principal directions ( $y$  in our case). For instance, lattices T1, T2, T3 have reflection symmetries, T4 and T5 have a glide symmetry and T7 has both. In lattices L1, T8, T9, T10 these symmetries are absent and therefore the microscopic shearing builds up and appears also at the macroscopic level.

Remarkably in some lattices (L6, L7) there is an intrinsic isotropic expansion although the single cells don't deform isotropically. With intrinsic we intend that the expansion is isotropic for any internal pressure, which means that isotropy is only related to the architecture of the lattice. In these cases again symmetry planes determine the isotropic behaviour. At a closer inspection indeed, lattice L6 shows two perpendicular reflection planes at  $\pm 45^\circ$  to the horizontal, while lattice L7 has two glide planes along the same directions: the only compatible deformation with double mirror symmetry is an isotropic one.

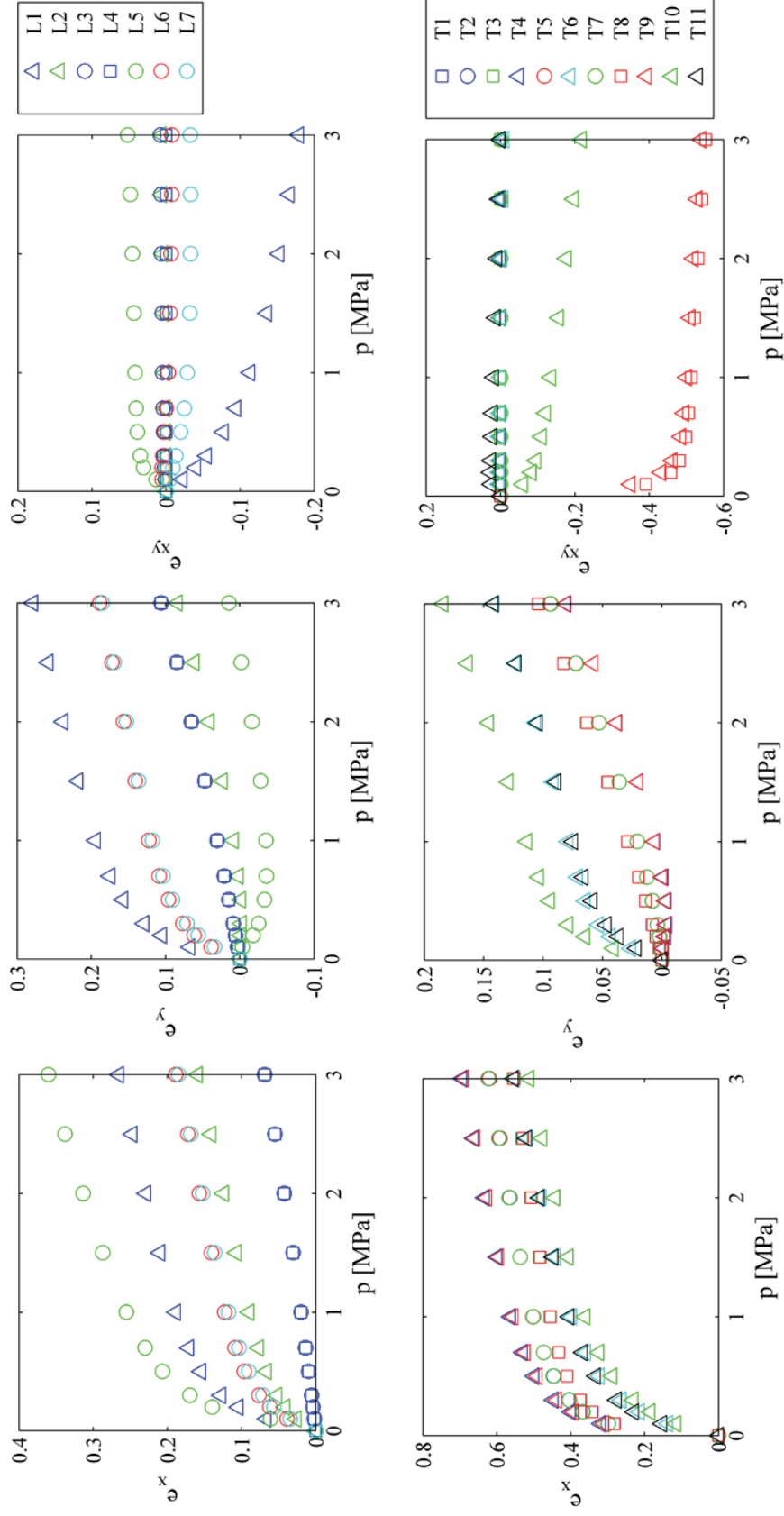


**Figure 4-17 Swelling eigenstrains in non-convex lattices.**

Here the swelling eigenstrains of L-lattices (first row) and T-lattices (second row) are presented. Almost all lattices show anisotropy of swelling – see also next figure- with higher expansions along the x direction and minor along the y direction. Also, both strains increase with a similar slope in the stretching dominated regime ( $p > 1$ ). Shearing instead is present only in few cases (L1, T8, T9, T10): the presence of mirror symmetries -with or without a glide plane- in the lattices balances the shearing of the individual cells so to avoid macroscopic shearing.



## 4. Results

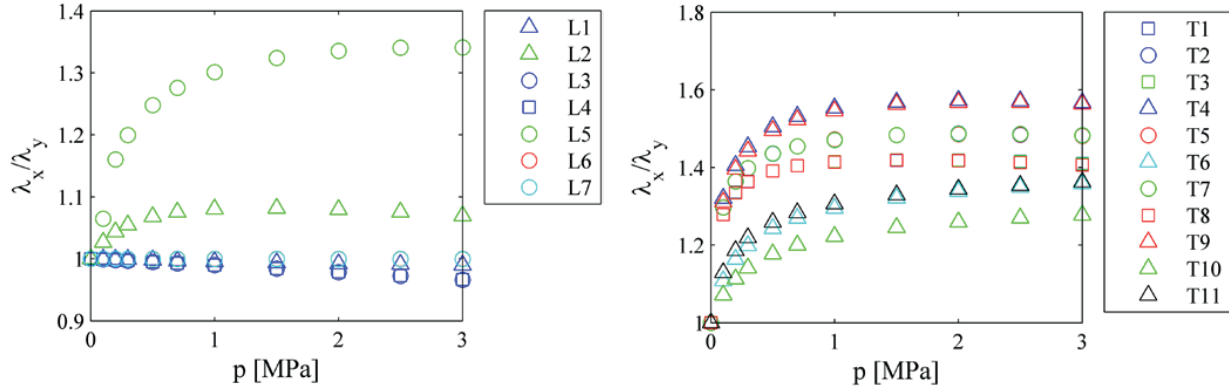


**Figure 4-18 Anisotropy of expansion in non-convex lattices**

*Non-convex lattices show generally an anisotropic expansion. Remarkably lattices L6 and L7 have intrinsically isotropic expansion behaviour (that is, the expansion is isotropic regardless of the internal pressure): this is due to the presence of double mirror symmetries at  $\pm 45^\circ$  to the horizontal.*

### 4.3.4 Influence of cell convexity on swelling eigenstrains

Figure 4-20 shows the area strain as a function of pressure in all lattices. For comparison, also the area strain relative to regular triangular, square and hexagonal honeycombs based on cells with same area as the “L” and “T” tiles are plotted.

In most of the lattices a two stage increase of the area strain can be observed, which relates to the bending and stretching regimes already discussed for the diamond-shaped honeycomb. The biggest area increase is achieved in the first stage, whereas in the stretching regime the area strain increases clearly with a smaller slope. Flat curves correspond to lattices which deform only by stretching: this is clearly the case of regular triangular, square and hexagonal honeycombs.

Also “T” lattices exhibit higher expansion than “L” lattices, which suggests that the maximum expansion is achieved for the least convex cells .

Still the data referring to each macrogroup appears scattered (especially in the case of “L” lattices), so we try to give an explanation for this in the next paragraph.



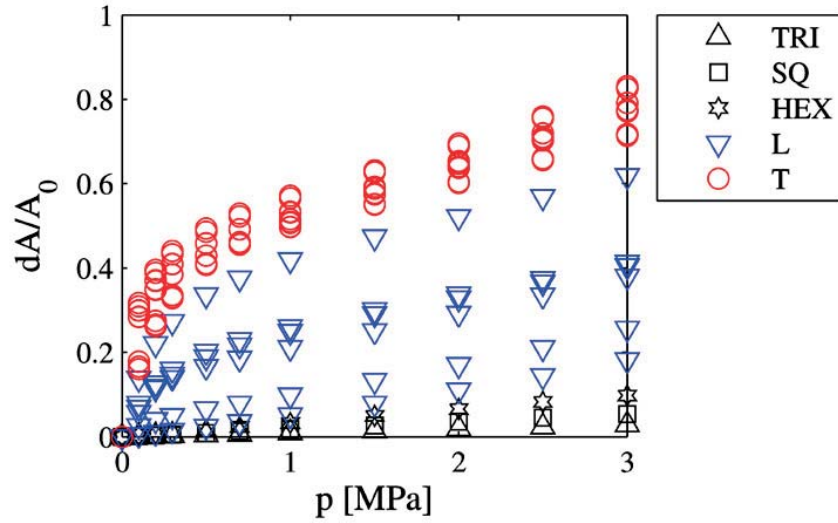


**Figure 4-19 Area strain comparison among lattices with different cell convexity.**

*L*-lattices which are based on more convex tiles expand less than *T*-lattices which are based on less convex ones. Still the evident data scattering hints that other parameters influence the lattice expansion.

#### 4.3.5 Influence of lattice connectivity on swelling eigenstrains

In the former paragraph we could hint that cell's convexity influences the expansion properties of a pressurised lattice. To be clearer, in Figure 4-21 the area strain for “L” and “T” lattices is reported in two separated plots.

As in the former paragraphs, each curve refers to a lattice (a snapshot of their geometry in the original and fully pressurised state as calculated by FE simulations can be found in paragraph 4.3.2). The symbol used to mark each lattice depends on its connectivity  $Z_e$  (see equation 2-1). Lattices with threefold connectivity are marked by a triangle; those with  $Z_e=3.333$  are marked by circles; and fourfold connected lattices are marked by squares.

In the case of *L*-lattices the highest expanding one is L1, for which  $Z_e=3$ . The second most expanding lattices are L5, L6, L7 ( $Z_e=3.333$ ). The least expanding lattices (L2, L3, L4) show a single rate area expansion: here the bending deformation and joint distortion are prevented because these mechanisms would be impeded by lattice periodicity, so the structure expands only by stretching (these will be discarded in the remainder of the discussion, as they don't undergo any significant deformation).

The same kind of clustering is observed in *T*-lattices, although here the difference between curves is more subtle (see enlarged inset). Lattices with  $Z_e=4$  (T1, T3, T8) show

#### 4. Results

the least expansion; those with  $Z_e=3.333$  (T2, T5, T7) form the second most expanding group, whereas lattices with  $Z_e=3$  separate in two: T4 and T9 experience the highest area strain, whereas lattices T6, T10 and T11 show a mixed behaviour, with low expansion in the bending regime while the slope in the stretching regime is comparable to T4 and T9.

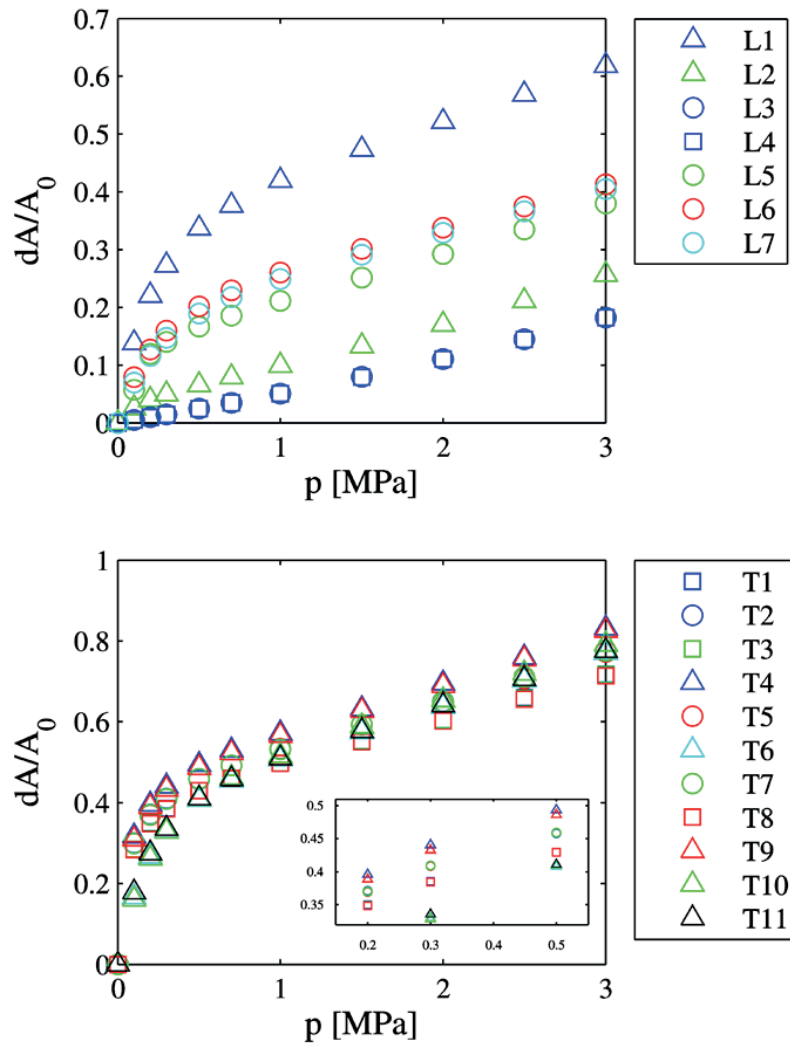


**Figure 4-20 Area strain comparison among “L” and “T” lattices.**

*As pressure increases, each non-convex lattice evolves to a convex one: this evolution is marked by a two stage area increase (excepted lattices L2, L3, L4 which are structurally locked -see paragraph 4.3.2). The area strain is proportional to the convexity of the cell in its pressurised state: the more convex this is, the bigger will be the area strain. The pressurized cell convexity depends on its local connectivity. in the inset in the lower graph it is shown that hexagonal lattices (triangles) expand more than pentagonal lattices (circles) which expand more than rectangular ones (marked by squares). T10 and T11 escape this rule since their joints undergo a higher joint distortion, so that the expansion is more energetically costly.*

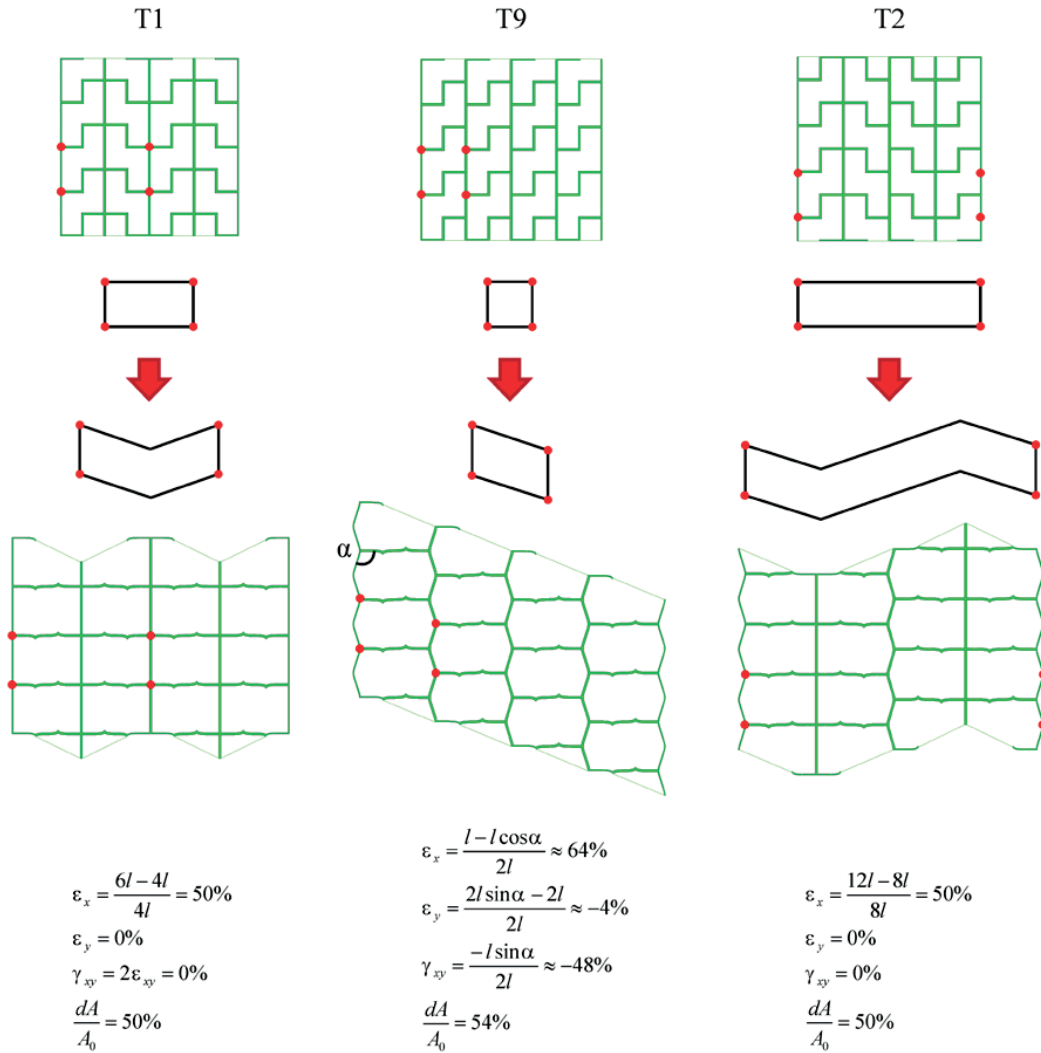


**Figure 4-21 Micro- and macrostrains in non-convex lattices.**

Macrostrains can be estimated from the geometrical transformation of the repetitive unit (delimited by red dots), considering rigid beams and freely rotating joints: the predicted values are close to those obtained by FE simulations (see Figure 4-18). When stretching of the beams is crucial (as in pentagonal lattice T2) the geometrical argument fails: in this case it predicts the same 50% horizontal strain as in quadrangular lattice T1, but the FE simulations show that it should have consistently higher strain due to reduced connectivity. Microstrains (black solid lines) are peculiar of each lattice architecture and create patterns that are preserved throughout the structure.

It is interesting that in some cases lattices belonging to the same group show perfectly matching curves (for instance T1, T3, T8). The reason for such behaviour becomes evident by comparing their pressurised configurations (Figure 4-14 and Figure 4-15): these lattices show an identical rectangular microstructure.

#### 4. Results

As pressure increases, each non-convex lattice evolves to a convex one as dictated by its topological class: in the pressurised state lattices with  $Z_e=3$ ,  $Z_e=3.333$ ,  $Z_e=4$  are respectively formed by hexagons, pentagons and rectangles. This is true on *average*: in reality, more than one convex polygon can appear in the pressurized lattice (see for example lattices L6, T6, T7, T10, T11) but the average number of sides per cell is fixed according to equation 2-3.

Now, since all lattices are formed by the same cell, the area strain is proportional to the convexity of the cell in its pressurised state: the more convex this is, the bigger will be the area strain. This is the reason why lattice L1 experiences by far the highest expansion among all “L” lattices: comparing lattices L1 and L5 it can be clearly seen (Figure 4-10 and Figure 4-13) that cells in L1 deform to a more convex polygon (a hexagon with 4 sides of length  $l$  and 2 sides of length  $2l$ ) than those in L5 (a pentagon with 3 sides of length  $l$ , one side of length  $2l$  and one side of length  $3l$ ).

The same conclusion could be drawn by a purely geometrical argument: if one assumes the beams to be infinitely rigid but freely joined together (as in a mechanism), the shape of the cells depends only on the angles between two adjacent beams. Then the pressurised configuration can be predicted maximizing the cell’s area by changing the internal angles: this gives a rough estimate of how much one lattice could expand with respect to another (see Figure 4-22). With this argument we can predict that hexagonal lattice T9 expands 4% more than T1 which is very close to the difference in area strain calculated in the FE simulations.

This geometrical argument fails to predict the expansion of pentagonal lattices like T2: if the beams are considered infinitely rigid, the cells can only adopt a rectangular shape (T2 becomes a degenerate rectangular lattice, while maintaining  $Z_e=3.333$ ) and therefore these lattices should expand equally to the rectangular ones. In reality this does not happen: in the inset of Figure 4-21 we clearly see that pentagonal lattices (marked by circles) consistently expand more than rectangular one (marked by squares): if the connectivity number expresses the average number of joints in each cell, and if the lattice expansion is mainly due to joints distortion, it is then reasonable that lattices with lower connectivity expand more than those with larger one. Obviously this is not a strict rule in itself since the actual deformation depends mostly (as we have already mentioned) on the

shape and convexity of the cells in the pressurised state. Also, the actual area strain resulting from the FE simulations depends on a number of factors that are not simply geometrical: for instance lattice T10 which in the pressurized state has the same microstructure of lattices T4 and T9 expands quite differently from those, probably because in lattice T10 the joints experience a more severe distortion.

#### 4.3.6 *Apparent stiffness*

Figure 4-23 shows the components of the stiffness tensor of the L-lattices normalized by the walls' Young modulus ( $E$ ). For clarity, markers have been replaced by lines: dotted lines refer to lattices with  $Z_e=3$ , dashed lines to lattices with  $Z_e=3.333$ , and solid lines to lattices with  $Z_e=4$ . Here, the calculation of the apparent stiffness is performed by applying a positive 5% strain to the pressurized configuration.

In general, as the pressure increases their mechanical properties improve. More than to the load bearing capacity of pressure (indeed we probe the lattices rigidity with an extensional strain), this is rather due to the geometrical changes of the microstructure, as observed in the diamond honeycombs. In our non-convex lattices the original low mechanical properties are related to the presence of many T-shaped connection points: these are weak points where deformations concentrate. The local effect of the fluid pressure on the microstructure is twofold; on one hand it deforms these junctions to a Y shape, on the other hand, kinked beams connecting two nodes straighten up. If these mechanisms take place (this is the case for all L- and T-lattices besides L3 and L4 which are “locked”) the microstructure switches from re-entrant to convex. A clear signature of this change is found in the two-stage dependency of the stiffness components with the pressure (Figure 4-23 and Figure 4-24). As all lattices have different microstructure, this switch can be more or less gradual and take place at different levels of pressure.

When, upon pressurization, the beams align along the principal directions, a corresponding “fast” increase of the  $C_{11}$  and  $C_{22}$  components is observed. This applies to all L-lattices excepted lattices L2 and L5: here beams that in the undeformed configuration were vertical become inclined in the pressurised one, therefore the  $C_{22}$  component decreases. In particular, the  $C_{66}$  component increases with pressure because a

#### 4. Results

pure shearing deformation of the lattice involves stretching the beams, whereas, at low pressures this deformation translates into joint rotations and beam bending and the lattice is more compliant to shearing.

When there is no major change in microstructure (as for the “locked” lattices L3 and L4) the stiffness components are characterized by a single stage decrease, which is due to the “relaxation” of the structure due to the copresence of an extensional probing strain and positive internal pressure (as explained in paragraph 4.2.2). This slow decrease is also observed in the  $C_{12}$  component of all lattices at higher pressures, where the lattices’ microstructure doesn’t change further as it is completely expanded.

The apparent stiffness in the T-lattices shows a well defined clustering into groups. Fourfold connected lattices (T1, T3, T8) have perfectly matching curves, since in the pressurised state they converge to the same geometry. They show the stiffest response to loading along principal directions because they converge to a rectangular lattice with continuous rows of vertical and horizontal struts (that is also the reason why they show the least rigidity to shearing deformations). The  $C_{22}$  component decreases with pressure since the vertical struts rows get more spaced in the pressurised state, reducing the apparent density of the lattice

In the pressurised state, pentagonal lattices (T2, T5, T7) show alternating rows of vertical struts and inclined beams and discontinuous horizontal struts (therefore  $C_{11}$  and  $C_{22}$  are lower than in quadrangular lattices).

The same reasoning applies to lattices with threefold connectivity, although in this case two subgroups can be seen: lattices T4 and T9 expand keeping their principal axes aligned with the loading directions; in lattices T6, T10, T11 these axes are inclined at about  $\pm 45^\circ$  with respect to the vertical direction. Therefore the former ones will be stiffer along the principal axes and soft in shearing, while the opposite can be said for the latter ones

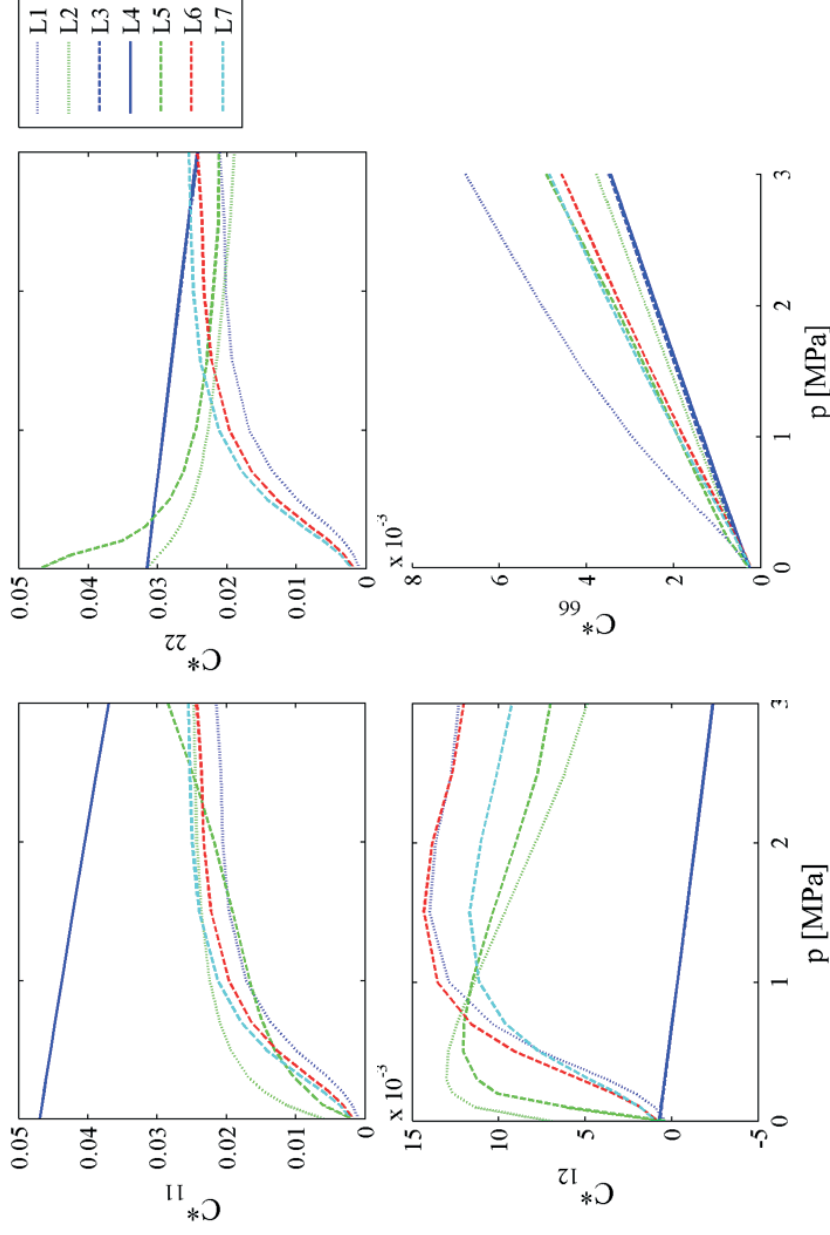


**Figure 4-22 Evolution of apparent stiffness of L-lattices upon pressurization (dotted:  $Z_e=3$ ; dashed:  $Z_e=3.33$ ; solid:  $Z_e=4$ ).**

*A two-stage dependency of the stiffness components is the signature of a switch from re-entrant to convex microstructure upon pressurization (all components and lattices excepted “locked” lattices L3 and L4). A steady slow decrease not correlated to microstructural changes is caused by the adoption of an extensional probing strain together with positive internal pressure (this applies to components C11, C22, C12 in lattices L3 and L4; and to component C12 in all other lattices at higher pressures). Increase/decrease in apparent stiffness is caused by beams alignment/misalignment (C22 in lattices L2, L5) to the principal directions. A steady increase of the C66 component results from the translation of macroscopic shearing into beams stretching, while this can be accommodated by joint rotations and beam bending at lower pressures.*

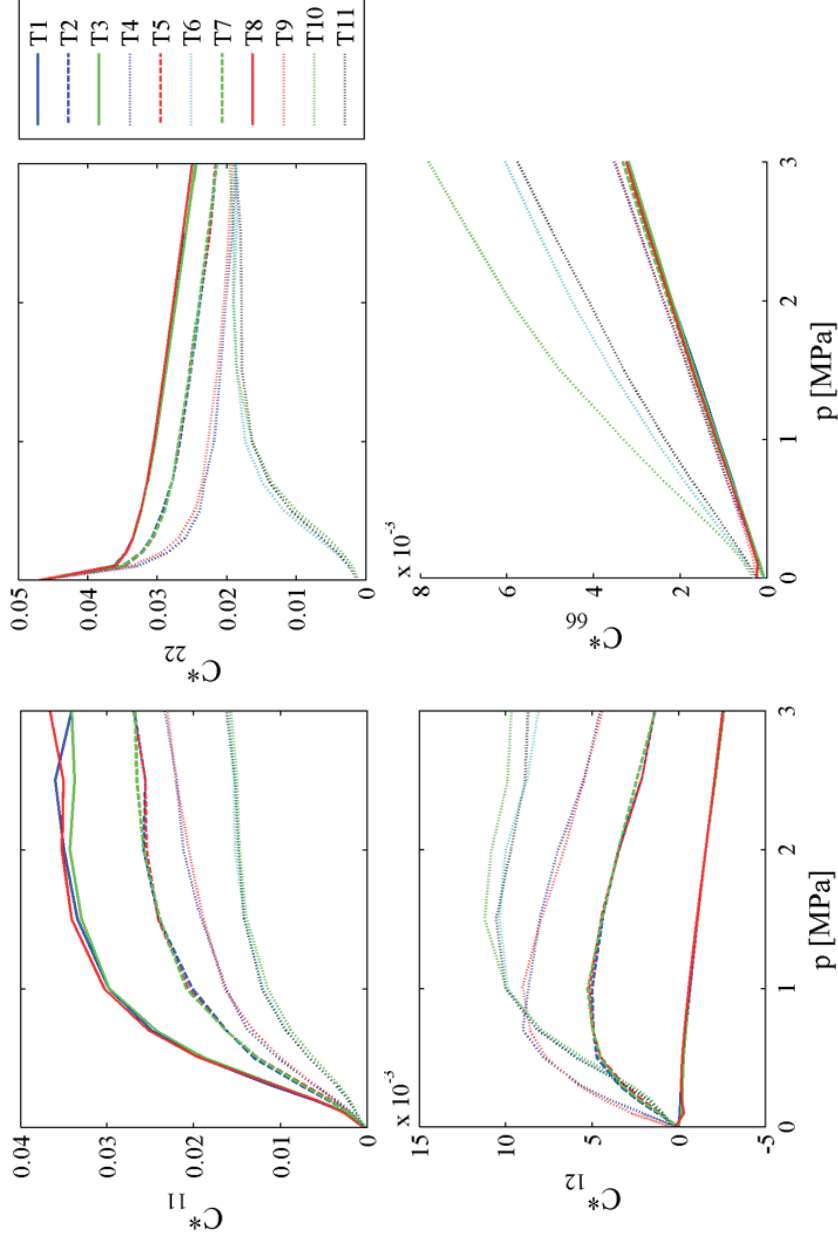


**Figure 4-23 Evolution of apparent stiffness of T-lattices upon pressurization (dotted:  $Z_c=3$ ; dashed:  $Z_c=3.33$ ; solid:  $Z_c=4$ ).** Essentially the same mechanisms observed for L-lattices apply to T-lattices. Here though the curves cluster according to the common microstructural evolution of the lattices upon pressurization: T1, T3, T8 evolve to the same rectangular lattice having principal axes aligned with the 11 and 22 loading directions; T2, T5, T7 and T4, T9 evolve respectively to pentagonal and hexagonal lattices again aligned with loading directions 1 and 2; T6, T10, T11 have principal axes are inclined at about  $\pm 45^\circ$  with respect to the direction 2 (therefore they show the lowest C11, C22 and highest C66 stiffness components). The C22 component in all but T6, T10, T11 lattices decreases because vertical beams get more spaced laterally.



### 4.3.7 Conclusions

In this section we showed that lattices based on non-convex cells can exhibit large expansions upon pressurization. The extent of expansion that can be achieved by pressurization relates to the initial convexity of the cells, but it is also influenced by the lattice topology. Instead, the anisotropy of expansion and the lattice apparent stiffness depend mostly on the lattice topology.

In our treatment, the number of lattices that we have analyzed was limited. Instead the number of possible lattices that can be designed from convex cells is infinite. Nonetheless, we still are able to trace a rationale for designing lattices that expand upon pressurization. In this respect, lattice topology is crucial. The Maxwell criterion sets the necessary topological condition for rigidity: if  $Z_e > 4$  no expansion is possible, since the lattice is rigid for *any* deformation. Actually this is a stronger criterion: it says that those lattices are rigid for *all* possible types of loading (therefore also for pressure). If  $Z_e \leq 4$  the Maxwell criterion states that expansion upon pressurization is possible, but is not giving any hint whether a specific lattice with  $Z_e \leq 4$  will expand. Lattices that expand upon pressurization must satisfy additional conditions: they must have periodic mechanisms that enable joint deformations; but they should also be built on cells whose area can be maximized by bending mechanisms rather than stretching of their perimeter. This is the case of anisotropic cells, as we have previously seen for the diamond shaped honeycomb; interestingly the definition of cell anisotropy given in paragraph 4.1.1 also applies to the non-convex cells presented in this section: non-convex polygons too cannot be inscribed into a circle.

Therefore cell anisotropy and convexity are both relevant parameters to design lattices that can expand by pressurization.

Besides their macroscopic expansion and stiffness properties, these non-convex lattices show definite patterns of microscopic deformations which are preserved throughout the entire lattice in virtue of the lattice regularity.

Considering these aspects all together, the variety of effects that can be obtained is truly vast. If one thinks that all these phenomena arise in response to a rather trivial internal pressurization of the lattice, even more so this can be regarded as complex actuation by

## 4. Results

material architecture. The immediate consequence is that, by arbitrarily designing the lattice architecture, one is able to obtain a desired actuation. Actuation can reach beyond the concept of mechanical work. Provided a suitable manufacturing technique, one can take advantage of the morphological change in microstructure to create different “devices“. One possibility (already illustrated in paragraph 4.2.3) is to obtain a mechanical actuator to push or pull a load, or to relatively displace objects at the microscopic level. Miniaturized lattices instead could form a layer with tuneable optical properties, which then could be used to create interference patterns.

### 4.4 Swelling in composite bidimensional cellular solids

Up until this point we have demonstrated, by means of theoretical predictions and numerical simulations, that cellular materials can actuate upon pressurization and that a variety of different effects can be achieved by simply tuning the lattice architecture. Nonetheless the assumptions that we made (namely, considering the effect of the swelling phase as a hydraulic pressure acting onto the walls, and that the walls themselves don't swell) are a strong departure from real systems occurring in Nature (as the *Delosperma nakurense* seed capsule). The main aim of this experimental part is to understand if those findings are still valid for an artificial actuating system based on constrained swelling in which both phases –the one filling the cells and the one forming the walls- can swell depending on the individual properties of each of the two components.

#### 4.4.1 Hydrogel filled honeycomb

The hydrogel filled honeycombs are characterized by a large anisotropic swelling: the measured strain along the honeycomb soft direction is 65%, while it is negligible along the transverse direction (Figure 4-25). Qualitatively the structure deforms very much likely to a pressurised honeycomb, although to a smaller extent. This system is a proof-of-concept for an actuating system based on constrained swelling in a closed cellular structure.

To be able to draw any conclusion from these experiments though, more extensive experiments are required where one is able to control the mechanical and swelling

#### 4. Results

properties of both materials used, which was not the case here. This system was not ideal for many reasons. First of all, the hydrogel synthesis was hard to be reliably controlled. Hydrogel porosity and stiffness were not always consistent from one batch of synthesis to the other. This was due to too many passages relying on the operator skills; for instance, manual stirring after addition of sodium bicarbonate powder resulted in uncontrolled and sparse porosity. Another operative issue was to keep the hydrogel inside the honeycomb cells while swelling. Since the honeycomb material is hydrophobic, the hydrogel precursors wouldn't diffuse in the honeycomb material and the newly formed hydrogel wouldn't stick to the walls. As a result the hydrogel escapes from the cells upon swelling (see Figure 4-25).

Finally, it was impossible to estimate the amount of hydrogel and its dilution state in the cells without destructing the sample: at the end of the polymerization, the hydrogel is in a wet state; drying of the sample (which was necessary to weigh the hydrogel) caused a detachment of the hydrogel from the walls, thus impairing the sample for subsequent swelling experiments.

For all these reasons we decided to focus on rapid prototyped samples made of two materials and the results of those experiments are presented in the next paragraph.



**Figure 4-24 Hydrogel filled honeycomb in its unswollen and swollen state.**

*Hydrogel-filled honeycomb could swell up to a 65% strain along the honeycomb's soft direction, but the poor control of the synthesis protocol, the variability of the hydrogel properties and the general difficulties in constraining the hydrogel inside the cells made this system inconvenient to carry on more systematic exploration.*

#### 4. Results

##### 4.4.2 Mechanical and free swelling properties of rapid prototyped materials

Here we report the mechanical (Young modulus  $E$ ) and swelling (extension ratio  $\lambda$ ) properties of the materials used by the 3D printer as obtained by the procedure described in chapter 3.3.3.

Material	T+	40	50	60	70	85	95	DM25	DM30	VW
$E$ [MPa]	0.4045	0.5644	0.8974	1.377	2.253	3.215	6.268	289.5	387.3	530
$G$ [MPa]	0.135	0.188	0.299	0.459	0.751	1.072	2.089	96.5	129.1	176.7
$\lambda$ [ $l/l_0$ ]	1.363	1.31	1.265	1.23	1.19	1.172	1.135	1.0044	1.0038	1.0033
$\chi$ (fitting eq. 2-22)	0.67	0.70	0.74	0.77	0.80	0.83	0.88	0.39	-0.49	-1.84

**Table 4-1 Dry Young modulus and linear expansion upon swelling in isopropanol for all materials available for 3D printing.**

*The material's shear modulus  $G$  (second row) was calculated considering a linear elastic isotropic behaviour and incompressibility (Poisson's ratio  $\nu=0.5$ ). In the third row we report the  $\chi$  parameter which best fits the experimentally measured shear modulus  $G$  and expansion  $\lambda$ , although, in the analytical model developed to interpret the experiments a fixed value of  $\chi=0.7$  was used for all materials.*

Following the Flory-Huggins theory (presented in paragraph 2.3.1) the swelling expansion in pure solvent and shear modulus of a polymer are linked together by equation eq. 2-22. Therefore, by knowing one of the two properties and the solvent-polymer interaction parameter  $\chi$ , it is possible to calculate the other. Since we independently measured both the Young modulus and the expansion upon swelling, we are able to check if the theory gives reasonable predictions for these systems. Assuming (as for rubber-like materials) incompressibility of the material in dry conditions (Poisson's ratio  $\nu=0.5$ ), the shear modulus  $G$  has been estimated via the following:

$$G = \frac{E}{2(1+\nu)} = \frac{1}{3}E \quad 4-4$$

Starting from we derived the value of  $\chi$  that gives the best fit to the theory. The resulting values of  $\chi$  for each material can be found Table 4-1.

It can be seen that  $\chi$  varies with the material composition, as expected for copolymers. For most of the cases,  $\chi$  ranges between 0.67 and 0.88 which is indicative of poor polymer-solvent miscibility. The three most stiff materials (DM25, DM30 and VW) give unrealistic  $\chi$  values, probably because the measured extensions were too small and the error comparatively too big and also because their structural and chemical properties are significantly different from the others.

In reality  $\chi$  is not constant, but it is also concentration-dependent, and should be measured for each solvent-material system by means –for example- of an absorption isotherm.

Therefore, the values of  $\chi$  reported in Table 4-1 don't have a rigorous chemical meaning but are those that best describe the swelling behaviour of the elastomers in a range close to the equilibrium with the pure solvent.

For a stiff material which doesn't experience significant expansion ( $v_2 \rightarrow 1$ ), the quadratic term in eq. 2-22 is negligible, and the predicted equilibrium expansion is not strongly influenced by  $\chi$ . Therefore the effect of  $\chi$  is much more pronounced for softer materials. Since a variable  $\chi$  would complicate our treatment, in the following we considered a fixed value of  $\chi=0.7$ , which is appropriate for our soft materials. In our calculations this doesn't affect too strongly the results (+10%) so that the theoretical predictions are still conclusive.

#### 4.4.3 *Honeycombs with soft inclusions*

In Figure 4-26 we report snapshots from a free swelling experiment of a diamond honeycomb sample build with stiffest (VW) and softest (T+) materials available for walls and cell inclusions respectively ( $G_{\text{walls}} = G_{\text{VW}} = 176.7 \text{ MPa}$ ,  $G_{\text{cells}} = G_{\text{T+}} = 0.135 \text{ MPa}$ ).

Qualitatively, the honeycombs deform similarly to what observed in the FE simulations and micromechanical model: the overall deformation is anisotropic with high swelling along  $y$  direction, and a contraction along  $x$  direction. The deformation is characterized by walls bending, with no evidence of walls stretching even in the last stages of swelling. The extent of deformation appears smaller than in the pressurised honeycomb. This is partly due to the fact that honeycomb samples used for the experiments were produced with thicker walls with respect to the geometry used the FE and micromechanical models:

#### 4. Results

samples with the original geometry were more prone to breaking so that the system couldn't even approach the swelling equilibrium. An increased walls' aspect ratio (from  $l/t=8$  to  $l/t=13$ ) implies a much higher energy spent into bending the walls (bending rigidity of a beam is proportional to the cube of  $l/t$ ), causing overall smaller deformations. Even with this expedient the samples would break after a variable time (3-4 days) depending on the materials used for walls and inclusions. Therefore, the swelling strains were measured right before the onset of the first walls breakage (this was a practical limitation that could not be overcome and has to be kept in mind when comparing these results with the analytical predictions that will be presented later in this paragraph).

While the pressurised honeycombs expand freely depending only on their architecture and the fluid simply "follows" the walls deformation, in these real models, the "source" of expansion relies on the amount of expansion of the softer inclusions. In turn, the swelling of the inclusions depends on their mechanical properties, the physico-chemical characteristics of the system (temperature, molar volume of the solvent, polymer-solvent affinity), and the mechanical constraints that the walls impose on them. The same reasoning holds for the honeycomb walls which are made of a polymeric material too and hence swell (albeit in smaller amounts with respect to the inclusions). This is different from the simulated expansions of the pressurized diamond honeycomb where we considered no swelling of the walls. In the rapid prototyped models that we consider in this section, the anisotropy of swelling will derive by the mismatch between the free swelling of walls and inclusions.

To better understand the mutual influence of walls and inclusions on swelling and to give a valid interpretation of the swelling experiments, in the following we apply and extend the treatment presented in section 2.2, to describe analytically the swelling behaviour of these diamond honeycombs with inclusions. The swelling eigenstrains predicted by this analytical model are then compared to those measured in the experiments.

Some introductory considerations have to be made in order to justify the following treatment. The swelling system comprises three phases: two solid phases for the walls and inclusions and a fluid phase for the solvent. We note that the fluid phase is much more abundant than the solid ones and it is free to migrate from the bulk into the two

solid ones until equilibrium is reached. Therefore we consider the fluid as an infinite reservoir which allows us to neglect it and consider the system as a two-phase one.

Regarding the deformation of the models (see Figure 4-26), it can be observed that all cells in the models deform similarly (the boundary cells deformation deviates only slightly from that in the centre cells), so that the deformation of the whole system can be studied by looking at one repetitive unit cell). Denoting with  $\lambda_i$  the stretching ratio along direction  $i$  (where  $l$  and  $t$  refer to the longitudinal and tangential directions of the wall) and taking superscripts “ $W$ ” and “ $C$ ” for walls and cells’ inclusions respectively, geometrical compatibility requires:

$$\alpha = \arctan\left(\frac{y_0}{x_0} \frac{\lambda_y^C}{\lambda_x^C}\right)$$

$$\lambda_l = \lambda_x^C \cos\left(\frac{\alpha}{2}\right)^2 + \lambda_y^C \sin\left(\frac{\alpha}{2}\right)^2 \quad 4-5$$

Then the stretching ratios  $\lambda_x$ ,  $\lambda_y$ ,  $\lambda_z$  of the unit cell read as:

$$\lambda_x = \frac{x_0}{x_0 + 2s_0} \lambda_x^C + \frac{2s_0}{x_0 + 2s_0} \left[ \sin\left(\frac{\alpha}{2}\right)^2 \lambda_l^W + \cos\left(\frac{\alpha}{2}\right)^2 \lambda_t^W \right]$$

$$\lambda_y = \frac{y_0}{y_0 + 2s_0} \lambda_y^C + \frac{2s_0}{y_0 + 2s_0} \left[ \cos\left(\frac{\alpha}{2}\right)^2 \lambda_t^W + \sin\left(\frac{\alpha}{2}\right)^2 \lambda_l^W \right] \quad 4-6$$

$$\lambda_z = \lambda_z^C = \lambda_z^W$$

With this convention any direct state of deformation (that is without shearing or out of plane buckling) can be determined by a set of 4 unknowns ( $\lambda_x^C, \lambda_y^C, \lambda_z^C, \lambda_l^W$ ). To predict the swollen configuration we set up the chemo-mechanical equilibrium on the inclusions and the walls separately. As seen in paragraph 2.3.1 the chemo-mechanical equilibrium in a one material system requires that the gain in free energy due to swelling (equation 2-20) be equal to the work of deformation of the polymeric network (equation 2-17) plus the work of external forces. Focusing on the cell inclusions, the work of the external forces is due to the walls bending energy and a term that includes the volumetric work of expansion. Then we can write:

#### 4. Results

$$\frac{1}{V_0} \left[ V_0^C \frac{\partial \Delta G^C}{\partial n^C} + V_0^C \frac{\partial W_e^C}{\partial n^C} + V_0^W \frac{\partial W_{ext}^W}{\partial \lambda_i^C} \right] = 0 \quad 4-7$$

The free energy of swelling is (recall equations 2-20 and 2-21):

$$\frac{\partial \Delta G^C}{\partial n^C} = \frac{RT}{v_{iprOH}} \left[ \ln(1 - v_2) + v_2 + \chi v_2^2 \right] \quad 4-8$$

The elastic network term is more conveniently written as:

$$\frac{\partial W_e^C}{\partial n^C} = \frac{\partial W_e^C}{\partial \lambda_i^C} \bigg/ \frac{\partial n^C}{\partial \lambda_i^C} \quad 4-9$$

where  $n^C$  is the volume concentration of solvent molecules in the cell material:

$$n^C = \lambda_x^C \lambda_y^C \lambda_z^C - 1 \quad 4-10$$

and  $W_e^C$  is (recall equation 2-17 and 2-18):

$$W_e^C = \frac{1}{2} G^C \left[ \lambda_x^{C^2} + \lambda_y^{C^2} + \lambda_z^{C^2} - 3 \right] \quad 4-11$$

Finally, for the work of walls deformation, the bending contribution can be modelled by the second of equations 3-14 while the volumetric term has to be calculated with respect to the equivalent isotropic swollen state  $\lambda_0^W$  (that is the isotropic swollen state where the polymer is at the same dilution):

$$W_{ext}^W = \frac{V_0}{V_0^W} K_t \frac{\sin\left(\frac{\alpha - \alpha_0}{2}\right)^2}{\sin(\alpha_0)} + \frac{1}{2} G^W \lambda_0^{W-3} \left[ \lambda_t^{W^2} + \lambda_t^{W^2} + \lambda_z^{W^2} - 3\lambda_0^{W^2} \right] \quad 4-12$$

where:

$$\lambda_0^W = \left( \lambda_t^W \lambda_t^W \lambda_z^W \right)^{\frac{1}{3}} \quad 4-13$$

Substituting subscript  $i$  with  $x, y, z$  in equation 4-7 provides three equations embodying the equilibrium of (generalized) forces along the honeycomb principal directions.

A fourth equation derives from the equilibrium of the walls. Here we make the hypothesis that the walls are free to swell along the tangential direction  $t$ , that is the tangential stress on the walls is equal to zero. This choice is motivated by the evidence that the walls



mainly undergo a shape change due to the swelling inclusions rather than being laterally compressed or stretched by the same. This condition translates in:

$$\frac{V_0^W}{V_0} \left( \frac{\partial \Delta G^W}{\partial n^W} + \frac{\partial W_e^W}{\partial n^W} \right) = 0 \quad 4-14$$

where relations similar to 4-8 to 4-11 apply along the tangential direction.

As stated previously, in these real models the anisotropy of swelling depends on the mismatch between the free swelling of walls and inclusions. In turn, as we know from equation 2-22, the free swelling of a cross-linked polymer depends on its shear modulus  $G$ . Therefore we conveniently report (Figure 4-27) the experimental data and analytical predictions of the honeycomb expansions as function of the ratio  $G_W/G_C$  between walls' and inclusions' shear modulus. In plot a) the walls' shear modulus increases over several orders of magnitude with respect to a fixed inclusions' shear modulus ( $G_C=0.135$  MPa). The solid lines are obtained by iteratively solving equations 4-7 and 4-14, whereas the dots mark the principal extensions  $\lambda_x$ ,  $\lambda_y$ , and the anisotropy ratio  $\lambda_y/\lambda_x$  measured from swelling experiments of honeycombs with walls' of increasingly stiffer materials (60, 95, DM25, VW) having shear modulus of  $G_{60}=0.459$  MPa,  $G_{95}=2.089$  MPa,  $G_{DM25}=96.5$  MPa and  $G_{VW}=176.7$  MPa (see also Table 4-1). When the walls are as stiff as the inclusions, the honeycomb deforms isotropically, as expected. As the walls' rigidity increases, the effect of structural anisotropy arises: a maximum extension (+50%) is achieved along direction  $y$  while a slight horizontal contraction is observed. The mechanical work required to deform the honeycomb increases for even more rigid walls, so that the principal extensions tend to unity. From our prediction, to maximize the expansion along the honeycomb soft axis ( $y$ -direction) the walls material has to be 100 to 1000 times stiffer than the inclusions.

Also, the model's prediction is not too far from the experimental data, although more data points are needed. Unfortunately the materials' available to the 3D printer are limited, so that broad ranges of these curves couldn't be probed experimentally (especially where the  $y$  extension has a maximum)

#### 4. Results

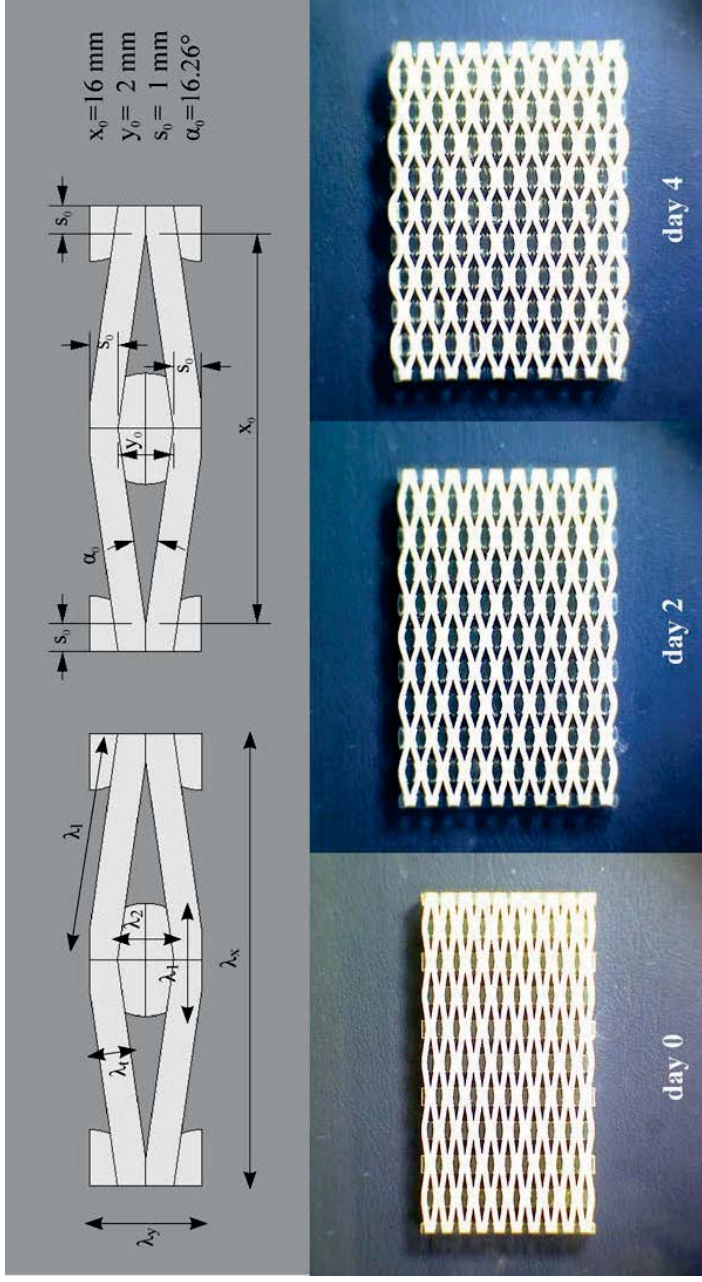


**Figure 4-25 Swelling of a diamond-shaped honeycomb with stiff walls and soft inclusions (VW-T+ materials).**

The honeycomb's unit cell geometry is reported with the kinematic variables (upper left) used in the analytical model and the actual dimensions (upper right). Since walls and inclusions are joined together, only 4 variables are needed to describe the deformation state of the unit cell: the principal stretching ratios of the inclusion ( $\lambda_x^C, \lambda_y^C, \lambda_z^C$ ) and the wall tangential stretching ratio  $\lambda_t$ . The total deformation of the unit cell results from compatibility relations (equations 4-6).

Swelling of a diamond-shaped honeycomb with "stiff" walls ( $G_{walls} = G_{TW} = 176.7$  MPa) and soft cell inclusions ( $G_{cells} = G_{T+} = 0.135$  MPa). Snapshots cover 5 days of swelling in isopropanol at room temperature ( $T = 22^\circ$ ). Time evolution of the deformed configurations resembles qualitatively that of the corresponding FE model, subjected to increasing internal hydrostatic pressure (see paragraph 4.1.1). Here too, the expansion along the honeycomb soft direction is higher than in the other direction ( $\lambda_y > \lambda_x$ ) as a result of geometrical anisotropy; also, an initial contraction along the x direction is observed which is recovered upon further swelling. Eventually, the samples rupture before reaching the swelling equilibrium (last frame).

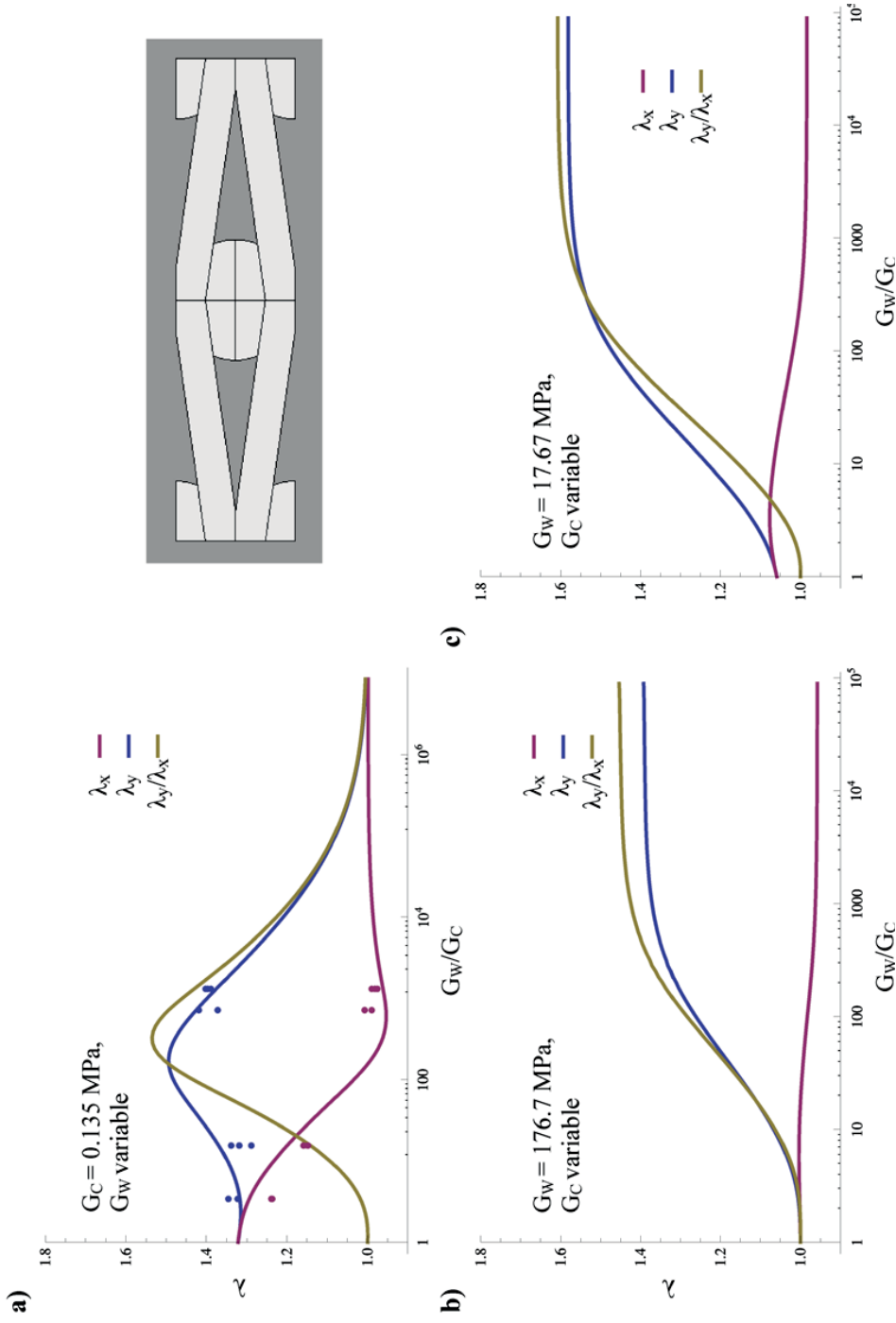


**Figure 4-26 Influence of walls ( $G_W$ ) and inclusions ( $G_C$ ) stiffness on the swelling deformations of a thick walled honeycomb.** Plot a) shows the influence of increasingly rigid walls and constant stiffness inclusions ( $G_C=0.135 \text{ MPa}$ ) on the overall swelling. At low walls-inclusions stiffness ratios, the swelling is isotropic; as the walls become stiffer the structure deforms anisotropically; for very stiff walls the inclusions are blocked and the honeycomb doesn't deform. The dots correspond to measured swelling of 3D printed honeycombs with soft inclusions ( $G_C=0.135 \text{ MPa}$ ) and increasingly stiff walls (respectively,  $G_{60}=0.459$ ,  $G_{95}=2.089$ ,  $G_{DM25}=96.5$  and  $G_{TW}=176.7 \text{ MPa}$ ). The experiments lie close to the analytical prediction. As the inclusions become softer with respect to the walls (plots b) and c), swelling deformations become markedly anisotropic until a plateau is reached. Since the amount of swelling depends non linearly on the material properties of the two materials building up the honeycomb. This is peculiar for actuating systems based on swelling and is different from the pressurised honeycombs where strain-pressure curves could be normalized to a single master curve (see Figure 4-7).

#### 4. Results

Now let's look at how a honeycomb with a given walls' stiffness and increasingly softer inclusions would swell. Softer inclusions undergo higher volume expansions upon swelling, so that they will exert a higher pressure on the walls: this is somehow analogous to the case of a pressurised honeycomb with given wall stiffness subjected to increasing internal pressure (see Figure 4-1), so we can compare between the two systems.

As seen for the pressurised honeycomb case, the swelling is again characterised by the typical anisotropy, arising when the inclusions become softer than the walls (and the ratio  $G_W/G_C$  increases). A major difference is that the absolute deformation in the swelling honeycombs is much smaller: comparing same thin wall geometries, the swelling honeycomb expands by 70% along  $y$  direction instead of 200% to 400% predicted by the FE simulations of the pressurised one (Figure 4-1). When the inclusions shear modulus  $G_C$  is one thousand times smaller than  $G_W$ , a *plateau* is reached (for both  $y$  and  $x$  strains). This is substantially different from what happens in the pressurised diamond honeycomb, where the  $y$ -strain keeps growing with a smaller rate due to the walls stretching at higher internal pressures: here instead the deformations are such that the walls don't experience noticeable stretching and the overall expansions is accommodated by the distortion of the honeycomb joints.

Another interesting feature that can be extracted by comparing plots b) and c) in Figure 4-27 is that the maximum achievable deformations (the *plateau* values) change depending on the walls stiffness ( $G_W$  in b) is ten times  $G_W$  in c). While in the pressurized honeycomb the eigenstrains (but also the apparent elastic properties) would scale with the ratio  $p/E$  between the internal pressure and the walls stiffness (see Figure 4-7), in these real honeycombs instead the swelling state depends strictly on the absolute value of both the walls and inclusions shear moduli.

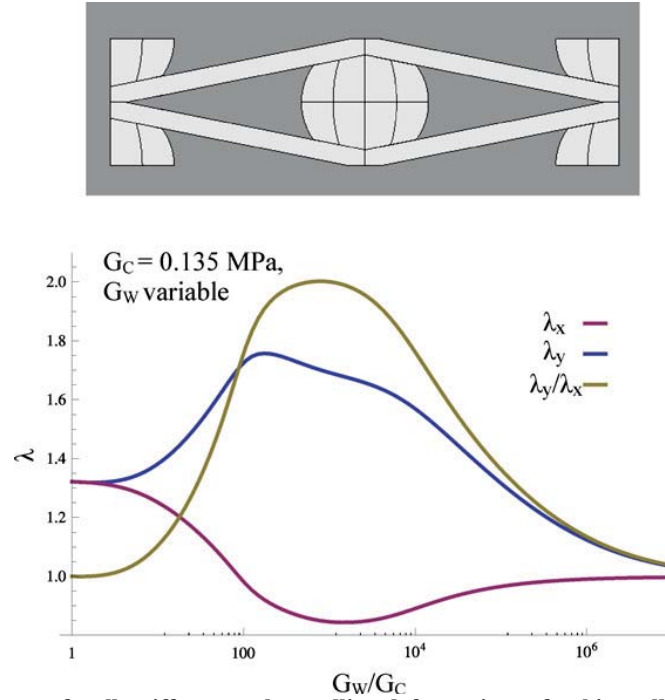


**Figure 4-27 Influence of walls stiffness on the swelling deformations of a thin walled honeycomb.**

Here the honeycomb geometry is the same implemented in the FE and micromechanical models. The absolute value of swelling deformations and anisotropy are higher than in the thick walled honeycomb, although they don't reach the huge strains predicted by the FE simulations on the pressurised diamond honeycombs.

#### 4.4.4 Non-convex lattices

Swelling in the rapid prototyped non-convex lattices is characterized by even lower expansions than that observed in the diamond honeycombs (as seen in the former paragraph). This is possibly due to the higher mechanical constraint acting on the soft material compared to the inclusions in the diamond honeycombs (indeed in these lattices the soft material lines the stiffer walls). Nonetheless the qualitative trend predicted by the FE simulations (see section 4.3) is preserved in these real counterparts. As such, the horizontal swelling strain in lattice T4 is the highest (10%) followed by that of lattice T1 (7.3%) while their vertical strain is negligible; lattice T8 experiences comparatively high spontaneous shearing (7.3%); and lattice T6 expands in both principal directions but more markedly along the horizontal (5.5%).

Despite these evident differences between the experimental system and simulations, the correspondence in the results is still quite remarkable. These experiments strengthen the role of lattice architecture in the determination of their expansion behaviour.



#### 4. Results

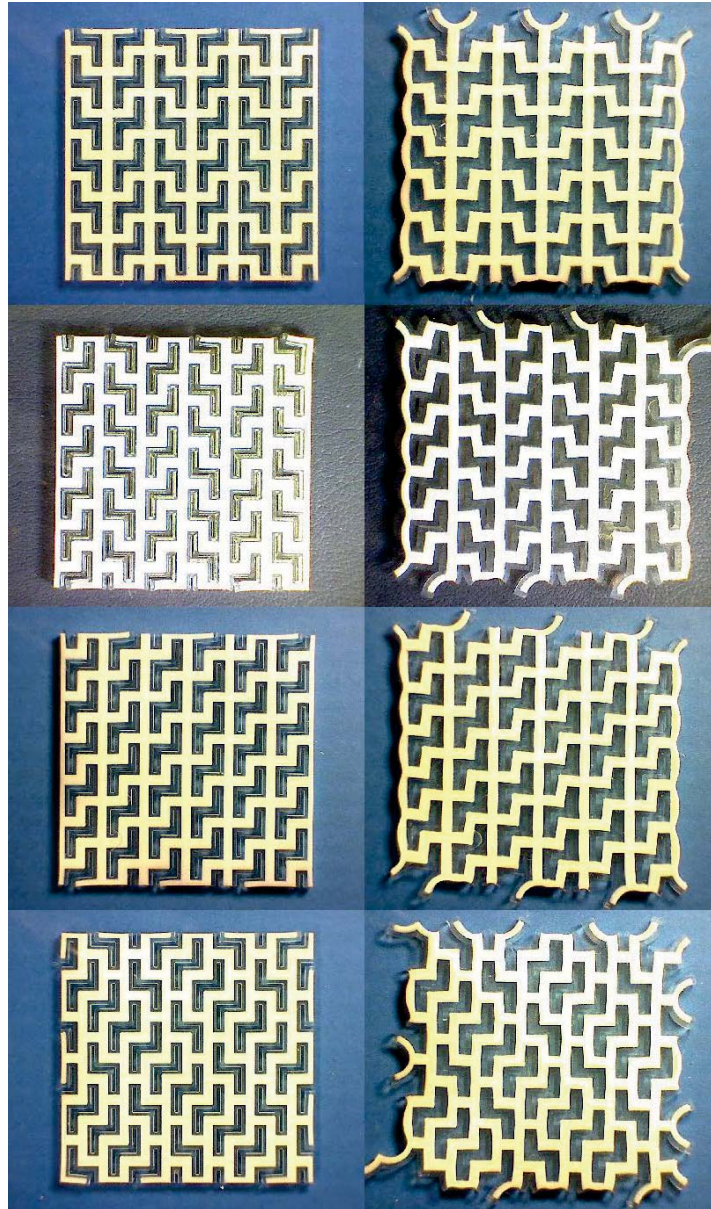


**Figure 4-28 Swelling of non-convex lattices based on the same cell geometry.**

*Samples of non-convex lattices (from top to bottom: T1, T4, T8, T6) in their original and swollen state prior to breakage. Although much lower, the swelling strains of these physical models confirm those calculated by the FE simulations presented in the previous section: in the simulations, T1 and T4 expand preferably along the horizontal direction with T4 expanding more than T1 (and here we measure 10% and 7.3% respectively); T8 undergoes in-plane shearing (7.3%) and horizontal extension; T6 expands in both principal directions but more markedly along the horizontal (5.5%).*

#### 4.4.5 Conclusions

In this section we have showed that the highest deformations achievable by a honeycomb with soft inclusions depend strictly on the absolute material properties chosen for both walls and inclusions. Also, the maximum deformations “saturate” and cannot be increased alone by choosing indefinitely soft inclusions. The existence of such a *plateau* can be explained by the fact that the chemical energy gained upon swelling decreases as the polymer gets more diluted (indeed it is a monotonous decreasing function of the polymer dilution  $v_2$ ): the more the inclusions expand, the smaller is the gain in energy. On the contrary, the mechanical work to stretch the polymeric network and deform the walls is a quadratic function of the stretching ratios. Since the mechanical work increases faster than the gain in chemical energy a plateau is reached. In the pressurized lattices instead, the pressure is constant and the volume of the cells can increase indefinitely. Our samples of honeycomb with inclusions function on the basis of an osmotic pressure: if the fluid volume fraction increases, the osmotic pressure sinks very rapidly. Therefore, to increase the maximum strokes in an artificial actuating system based on swelling, a proper choice of solvent and polymer with high chemical affinity should be made.

This sheds some light on the working principle of the active tissue in the *Delosperma nakurense* seed capsule: that is a system that converts chemical energy into mechanical work. A massive 4-fold elongation of the keels’ tissue (which is much higher than in our experiments) can be obtained because the hygroscopic CIL layer expands against a much more anisotropic –and hence softer– structure.





## 5. Conclusions & Outlook

The main inspiration for this work is the passive swelling driven actuation of the *Delosperma nakurense* seed capsule. Swelling as a phenomenon to generate expansion is at the basis of many natural and material based actuating systems. The best known examples of swelling driven actuating natural materials are based on fibre reinforced materials: these are usually found when high stresses need to be generated such as in reaction wood. Instead, those that are based on constrained swelling in a cellular material are able to generate large strains, as in the keels tissue of the *Delosperma nakurense*. In this work we tried to extrapolate a "minimal" description that was able to describe both qualitatively and quantitatively the actuation behaviour of cellular materials. Our methods included finite element simulations, micromechanical modelling and swelling experiments on rapid prototyped models made of two materials with different mechanical and swelling properties.

In particular, we considered various cellular material designs which are all non-rigid according to the Maxwell criterion. This is a necessary condition if one wants to obtain large deformations: these can only be achieved if the material microstructure behaves as a mechanism, with bending of the walls and localized distortion of the junctions in between.

Firstly we analyzed by means of finite element simulations and micromechanical modelling the expansion and mechanical properties of a diamond shaped honeycomb

## 5. Conclusions & Outlook

similar to the keels tissue found in the *Delosperma nakurense* seed capsule. In the diamond shaped honeycomb model we simplified our treatment and considered linear elastic walls internally pressurized by a fluid; here we could show that huge expansions (300% and more) can be achieved: the maximum extent of these depends on the geometrical anisotropy of the cell in its undeformed state. Also, as the honeycomb expands, its microstructure deforms which strongly influences its apparent mechanical properties. In this idealized system, both the swelling eigenstrains and the honeycomb apparent stiffness scale with the ratio  $p/E$  between the fluid pressure and Young modulus of the walls.

As cell anisotropy has proven to be relevant parameter affecting the expansion properties, we extended our search considering lattices based on two different non-convex cells. In this case the number of possible lattice designs increases because non-convex cells can be joined together in a variety of ways. We obtained a number of lattice architectures, which belong to different topological classes (where a topological class is defined by the average connectivity of the lattice beams). Therefore we could investigate the effect of cell convexity and connectivity on the expansion properties. By comparing the area expansion in all lattices, we were able to show that less convex cells are prone to achieve larger area expansions. Nonetheless the direction in which the material expands depends also on the local connectivity of each cell. This has repercussions both at the macroscopic (lattice level) and microscopic (cells level) scales. At the macroscopic scale, these non-convex lattices can experience large anisotropic (similarly to the diamond shaped honeycomb) or perfectly isotropic principal expansions, large shearing deformations or a mixed behaviour. Moreover, lattices that at the macroscopic scale expand similarly can show quite different microscopic deformation patterns that include zigzag motions and radical changes of the initial cell shape. Depending on the lattice architecture, the microscopic deformations of the individual cells can be equal or not, so that they can build up or mutually compensate and hence give rise to the aforementioned variety of macroscopic behaviours. Interestingly, simple geometrical arguments involving the undeformed cell shape and its local connectivity enable to predict the results of the FE simulations. Since the lattices' microstructure changes so drastically upon pressurization, a corresponding change in their apparent elastic properties is observed. Depending on the

## 5. Conclusions & Outlook

direction along which the beams align, the lattices can stiffen along their principal axes or become more compliant. Also a generalized increase of the shearing rigidity is observed. The swelling experiments on the rapid prototyped models qualitatively confirmed the same observations. In these systems though, the anisotropy of swelling depends also on the choice of the materials for walls and inclusions. In particular, anisotropy arises as a consequence of the mismatch in free swelling between stiff and soft materials. To assess this evidence we derived an analytical model that predicts the swelling expansions in a diamond honeycomb with stiff walls and soft inclusions. When the ratio between materials stiffness is too low, the expansion is isotropic. When the walls are several orders of magnitude stiffer than the inclusions, no swelling is observed. In our prediction a stiffness ratio of 100 to 1000 maximizes both the anisotropy and expansion along the honeycomb's soft axis ( $y$  direction). A major difference between the two swelling and pressurized honeycombs is that while in the pressurized honeycombs the eigenstrains scale with the ratio  $p/E$  between the pressure and the walls Young modulus, in the swelling system there isn't such a scaling law and the swelling expansion depends on the absolute values of both the walls and inclusions modulus.

Also, the extent of the expansion in the experiments was actually smaller than in the case of the simulations. This discrepancy is due to the different physical origin of the two phenomena. In the rapid prototyped models the honeycomb deformation is promoted by the gain in free energy connected to the swelling of the softer inclusion; as the polymer in the inclusions gets diluted, the chemical energy sinks and the honeycomb expansion stops. In the pressurized honeycombs instead the pressure is independent from the cell volume and therefore larger expansions that reach the stretching dominated regime are achieved. In other words, considering the source of actuation as a swelling phase limits the maximum expansions: chemical energy gained upon swelling is very limited at high dilutions; therefore expansion will be in general less than in the pneumatic counterpart. A system based on constrained swelling in cellular tissue could produce high strokes by minimizing the stiffness of the lattice. This explains why in the *Delosperma nakurense* the tissue architecture is characterized by a high geometrical anisotropy (much more than in our simulations): in this way the stresses needed to deform the honeycomb are kept

## 5. Conclusions & Outlook

low thereby increasing the maximum strains. This is a complementary behaviour to wood actuation, where, instead, the strains are usually very low and the stresses are maximized.

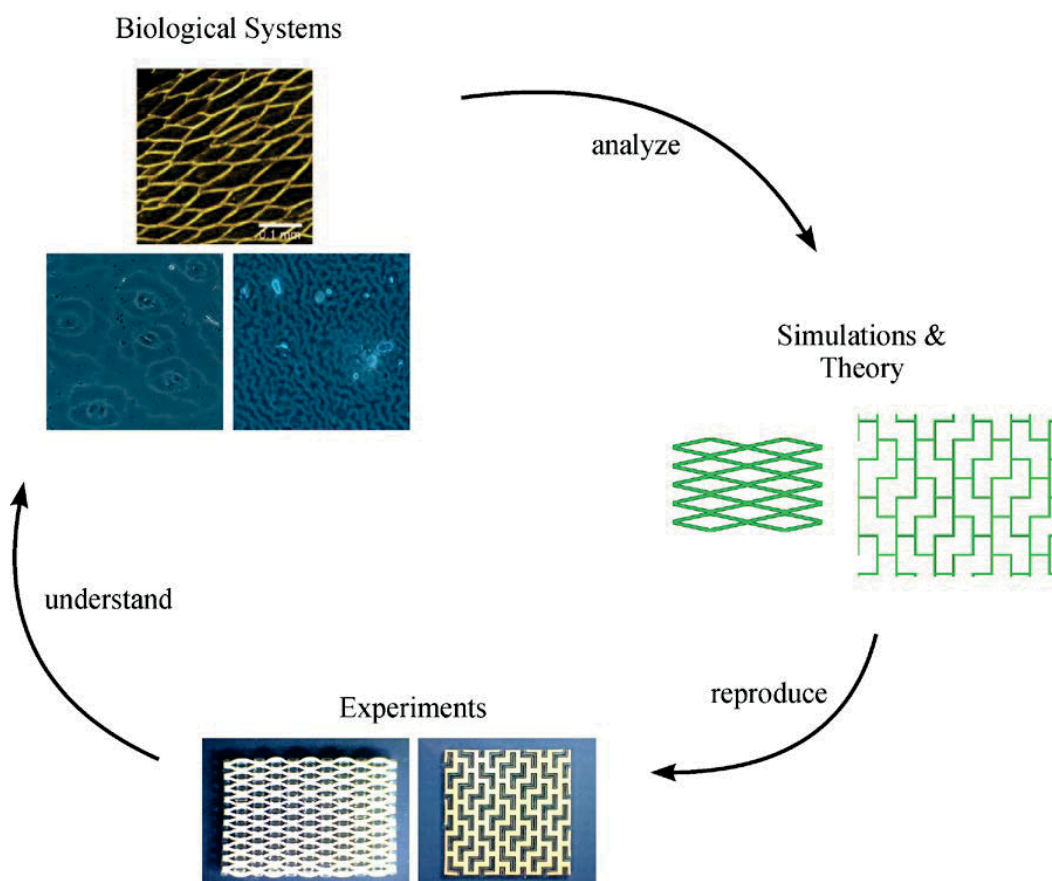


**Figure 5-1 Visual summary of the present work.**

*In this thesis we tried to understand the working principle of natural passive actuators based on swelling in cellular confinement. We firstly analyzed a simplified version of these by means of customized simulation methods; at this point many simplifications had to be considered, but we had the opportunity to investigate an extended range of materials' architectures. Here we could assess the influence of material architecture on the actuation capabilities. The relevance to real systems and applicability of our method was then tested on artificial system: the differences that arose were useful to understand the limits of our modelling technique, but also shed some light on how the biological systems work. Finally, the methods developed here could be useful to understand similar biological systems based on non-convex interdigitating cells (blue stained cross-sectional samples - pictures courtesy of Dr. Alexander Ivakov)*

In our treatment we considered the mechanical actuation of the planar lattices as a two-dimensional linear phenomenon. A possible extension of our work is to explore also the out-of-plane deformations and non linear behaviour of these lattices. In this regard, at least two scenarios deserve attention.

## 5. Conclusions & Outlook

The first one considers a negative pressure applied in the cells. In this case, past a given threshold pressure, local buckling of the cells would arise. This possibility was already explored by Bertoldi *et al.* in a study regarding buckling induced deformation patterns in two dimensional cellular solids made of an elastomeric polymer with periodic arrangement of holes [100]. The authors have shown that a uniaxial compressive strain causes a microscopic deformation pattern characterized by buckling of the ligaments between the holes. The buckling mode of the inter-hole ligaments depends on the microstructure: square and rhombic arrangement of circular holes bring respectively to rotation and shear buckling with a corresponding contraction of the material along the direction perpendicular to the load. The microscopic pattern transformations were influenced by choosing elliptical instead of circular holes or changing ligament thickness. If even such simple modifications to the microstructure could enable control on the buckling patterns, we argue that the non-convex lattices presented in this work (with their high geometrical variability) could also give rise to at least as rich pattern transformations.

A slight variation to this scenario would consider a cellular material composed of cells with different shapes. Depending on their connectivity, triangulated cells would behave as rigid, non collapsing elements whereas four (or more) sided cells would collapse producing high local strains. Then, if neighbouring cells show contrasting localized strains, the lattice could deform to more energetically favoured out-of-plane configurations. Also, these different configurations could be chosen a priori by mixing cells with different number of sides in the same lattice; something along these lines has been already observed in spherical lattices called “buckliballs” [101] : here the shape transformations are also “written in the structure” and the selective collapse of the cells brings to a reversible shrinking of the sphere.

The second scenario could be to exploit these non-convex honeycombs to produce out-of-plane wrinkling patterns. This could be achieved by assembling one of these honeycombs to a flat elastic sheet. As we have seen, the macro- and micro-deformations are bridged; therefore a simple uniaxial deformation imposed to the assembly would cause a specific, microscopic deformation. The latter would be frustrated by the high in plane rigidity of the sheet, giving rise to out-of-plane buckling of the membrane, with periodical patterns

## 5. Conclusions & Outlook

of bulges and valleys, that is, complex 3D motifs could arise. Provided a suitable manufacturing technique, such structures could be realized at the micron scale: then tuneable surfaces could be created that are activated by mechanical deformation. Similar actuating surfaces have been realized in a hydrogel-nano pillars system [102] where the surface responds to humidity changes.

In our modelling description (which is based on continuum mechanics) we neglected the fluid transport in the system: most probably this will result in size effects, with shorter time constants for the actuation process in smaller objects and longer ones in larger objects [34], but we argue that at equilibrium the actuated configurations would still be a result of just the architecture. Also, we are aware that at very smaller scales the continuum description is no longer valid and capillary effects that arise at sub-millimetre scales would become more important. When capillary size goes down to sub micron length scales the coupling between condensation and structural deformations becomes evident and large contraction strains are expected. This links back to the stability of these structures under negative pressures: buckling modes with structure folding could be triggered by condensation whereas large expansions (of the type introduced previously) could arise for positive hydraulic pressures of the fluid. Moreover these phenomena will depend on the physical properties of the adsorbed fluid and the interaction between the structure and the fluid, which would become a further aspect to be considered: therefore a complete description should not overlook the phenomena arising at these smaller scales. In this regard, preliminary simulation studies using Monte Carlo simulations of fluids in nanoconfinement could result most useful as a tool for exploring the influence of several specific parameters, such as fluid-structure affinity and geometry of nanoconfinement. All these aspects deserve more attention especially if one thinks that contraction forces increase by orders of magnitude at these scales.

The importance of shape, topology and architecture in the mechanical properties of 2D cellular materials has been well studied: surprisingly, till now little focus has been made on how these aspects are also relevant for the actuation capabilities of such cellular materials, as they confer specificity to simple swelling and pneumatic expansions. We also tried to outline the large horizon of possible applications. Nonetheless, Nature provides additional examples of structures that are similar to our non-convex lattices.

## 5. Conclusions & Outlook

These are found in the epidermal layer of the leaves of some bushes and short stem trees (see Figure 5-1). Interestingly in some species the cells display a complex interdigitating structure and in others the cells are more rounded or polygonal. It is suspected that that the geometry of these interlocking cells may have a structural role, however till now this has not been proved. Perhaps the modelling techniques developed in this thesis to describe *Delosperma nakurense*, may provide insight into this other system

## 6. Publications

1. Guiducci, L.; Fratzl P.; Bréchet Y.J.M.; Dunlop J.W.C.  
*Pressurized honeycomb as soft-actuators: a theoretical study.*  
Manuscript prepared for submission.
2. Guiducci, L.; Fratzl P.; Bréchet Y. J. M.; Dunlop J.W.C.  
*Designing actuators with a hidden length scale.*  
In preparation.
3. Turcaud, S.; Guiducci, L.; Fratzl, P.; Brechet, Y.J.M.; Dunlop, J.W.C.  
*An excursion into the design space of biomimetic architected biphasic actuators*  
International Journal of Materials Research, 102, 2011: 607-612
4. Harrington, M.J.; Razghandi, K.; Ditsch, F.; Guiducci, L.; Rueggeberg, M.; Dunlop, J.W.C.; Fratzl, P.; Neinhuis, C.; Burgert, I.  
*Origami-like unfolding of hydro-actuated ice plant seed capsules.*  
Nature Communications, 2011. **2**.
5. Razghandi, K.; Bertinetti L.; Guiducci, L.; Dunlop, J. W. C. ; Neinhuis, C.; Fratzl, P.; Burgert, I.  
*A Biogenic Engine Powered By Water Uptake.*  
Submitted to Journal of the Royal Society of Interfaces, 2013, under review.



## 7. References

1. Allen, R. and A. Wardrop, *The opening and shedding mechanism of the female cones of Pinus radiata*. Australian Journal of Botany, 1964. **12**(2): p. 125-134.
2. Harlow, W.M., W.A. Côté, and A.C. Day, *The Opening Mechanism of Pine Cone Scales*. Journal of Forestry, 1964. **62**(8): p. 538-540.
3. Haupt, W., *Physiology of Movements*. 1979, [S.l.]: Springer Verlag.
4. Ruhland, W., *Handbuch der Pflanzenphysiologie = Encyclopedia of plant physiology*. 1955, Berlin: Springer.
5. Reyssat, E. and L. Mahadevan, *Hygromorphs: from pine cones to biomimetic bilayers*. Journal of the Royal Society Interface, 2009. **6**(39): p. 951-957.
6. Forterre, Y., et al., *How the Venus flytrap snaps*. Nature, 2005. **433**(7024): p. 421-425.
7. Fratzl, P., *Biomimetic materials research: what can we really learn from nature's structural materials?* Journal of the Royal Society Interface, 2007. **4**(15): p. 637-642.
8. Burgert, I. and P. Fratzl, *Actuation systems in plants as prototypes for bioinspired devices*. Philosophical Transactions of the Royal Society a-Mathematical Physical and Engineering Sciences, 2009. **367**(1893): p. 1541-1557.
9. Lienhard, J., et al., *Flectofin: a hingeless flapping mechanism inspired by nature*. Bioinspiration & Biomimetics, 2011. **6**(4).
10. Laschi, C., et al., *Soft Robot Arm Inspired by the Octopus*. Advanced Robotics, 2012. **26**(7): p. 709-727.
11. Laschi, C., et al., *Design and Development of a Soft Actuator for a Robot Inspired by the Octopus Arm*. Experimental Robotics, 2009. **54**: p. 25-33.
12. Martinez, R.V., et al., *Robotic Tentacles with Three-Dimensional Mobility Based on Flexible Elastomers*. Advanced Materials, 2013. **25**(2): p. 205-212.
13. Martinez, R.V., et al., *Elastomeric Origami: Programmable Paper-Elastomer Composites as Pneumatic Actuators*. Advanced Functional Materials, 2012. **22**(7): p. 1376-1384.
14. Dunlop, J.W.C. and P. Fratzl, *Multilevel architectures in natural materials*. Scripta Materialia, 2013. **68**(1): p. 8-12.
15. Fratzl, P. and R. Weinkamer, *Nature's hierarchical materials*. Progress in Materials Science, 2007. **52**(8): p. 1263-1334.
16. Harrington, M.J., et al., *Origami-like unfolding of hydro-actuated ice plant seed capsules*. Nature Communications, 2011. **2**.
17. Razghandi, K.B., L.; Guiducci, L.; Dunlop, J. W. C. ; Neinhuis, C.; Fratzl, P.; Burgert, I., *A Biogenic Engine Powered By Water Uptake*. Submitted to Journal of the Royal Society of Interfaces, 2013.
18. Gao, H.J., et al., *Materials become insensitive to flaws at nanoscale: Lessons from nature*. Proceedings of the National Academy of Sciences of the United States of America, 2003. **100**(10): p. 5597-5600.
19. Gor, G.Y. and A.V. Neimark, *Adsorption-Induced Deformation of Mesoporous Solids*. Langmuir, 2010. **26**(16): p. 13021-13027.

## 6. References

20. Gor, G.Y. and A.V. Neimark, *Adsorption-Induced Deformation of Mesoporous Solids: Macroscopic Approach and Density Functional Theory*. Langmuir, 2011. **27**(11): p. 6926-6931.
21. Gunther, G. and M. Schoen, *Sorption strains and their consequences for capillary condensation in nanoconfinement*. Molecular Simulation, 2009. **35**(1-2): p. 138-150.
22. Schoen, M., et al., *Pore-lattice deformations in ordered mesoporous matrices: experimental studies and theoretical analysis*. Physical Chemistry Chemical Physics, 2010. **12**(37): p. 11267-11279.
23. Kumar, P., S.H. Han, and H.E. Stanley, *Anomalies of water and hydrogen bond dynamics in hydrophobic nanoconfinement*. Journal of Physics-Condensed Matter, 2009. **21**(50).
24. Gibson, L.J. and M.F. Ashby, *Cellular solids : structure & properties*. 1988, Oxford: Pergamon.
25. Gibson, L.J., M.F. Ashby, and B.A. Harley, *Cellular materials in nature and medicine*. 2010, Cambridge: Cambridge University Press.
26. Kumar, R.S. and D.L. McDowell, *Generalized continuum modeling of 2-D periodic cellular solids*. International Journal of Solids and Structures, 2004. **41**(26): p. 7399-7422.
27. Warren, W.E. and A.M. Kraynik, *Foam Mechanics - the Linear Elastic Response of Two-Dimensional Spatially Periodic Cellular Materials*. Mechanics of Materials, 1987. **6**(1): p. 27-37.
28. Warren, W.E., A.M. Kraynik, and C.M. Stone, *A Constitutive Model for Two-Dimensional Nonlinear Elastic Foams*. Journal of the Mechanics and Physics of Solids, 1989. **37**(6): p. 717-733.
29. Ashby, M.F. and Y.J.M. Brechet, *Designing hybrid materials*. Acta Materialia, 2003. **51**(19): p. 5801-5821.
30. Ionov, L., *Actively-moving materials based on stimuli-responsive polymers*. Journal of Materials Chemistry, 2010. **20**(17): p. 3382-3390.
31. Abraham, Y., et al., *Tilted cellulose arrangement as a novel mechanism for hygroscopic coiling in the stork's bill awn*. Journal of the Royal Society Interface, 2012. **9**(69): p. 640-647.
32. Vincent, O., et al., *Ultra-fast underwater suction traps*. Proceedings of the Royal Society B-Biological Sciences, 2011. **278**(1720): p. 2909-2914.
33. Niklas, K.J., *Plant biomechanics : an engineering approach to plant form and function*. 1992: University of Chicago Press.
34. Skotheim, J.M. and L. Mahadevan, *Physical limits and design principles for plant and fungal movements*. Science, 2005. **308**(5726): p. 1308-1310.
35. Gross, A.S. and J.W. Chu, *On the Molecular Origins of Biomass Recalcitrance: The Interaction Network and Solvation Structures of Cellulose Microfibrils*. Journal of Physical Chemistry B, 2010. **114**(42): p. 13333-13341.
36. Neagu, R.C. and E.K. Gamstedt, *Modelling of effects of ultrastructural morphology on the hygroelastic properties of wood fibres*. Journal of Materials Science, 2007. **42**(24): p. 10254-10274.

37. Gross, A.S., A.T. Bell, and J.W. Chu, *Thermodynamics of Cellulose Solvation in Water and the Ionic Liquid 1-Butyl-3-Methylimidazolium Chloride*. Journal of Physical Chemistry B, 2011. **115**(46): p. 13433-13440.
38. Cosgrove, D.J., *Growth of the plant cell wall*. Nature Reviews Molecular Cell Biology, 2005. **6**(11): p. 850-861.
39. Emons, A.M.C. and B.M. Mulder, *How the deposition of cellulose microfibrils builds cell wall architecture*. Trends in Plant Science, 2000. **5**(1): p. 35-40.
40. Burgert, I. and P. Fratzl, *Plants control the properties and actuation of their organs through the orientation of cellulose fibrils in their cell walls*. Integrative and Comparative Biology, 2009. **49**(1): p. 69-79.
41. Baskin, T.I., *Anisotropic expansion of the plant cell wall*. Annual Review of Cell and Developmental Biology, 2005. **21**: p. 203-222.
42. Marklund, E. and J. Varna, *Modeling the hygroexpansion of aligned wood fiber composites*. Composites Science and Technology, 2009. **69**(7-8): p. 1108-1114.
43. Burgert, I., et al., *Tensile and compressive stresses in tracheids are induced by swelling based on geometrical constraints of the wood cell*. Planta, 2007. **226**(4): p. 981-987.
44. Fratzl, P., R. Elbaum, and I. Burgert, *Cellulose fibrils direct plant organ movements*. Faraday Discussions, 2008. **139**: p. 275-282.
45. Goswami, L., et al., *Stress generation in the tension wood of poplar is based on the lateral swelling power of the G-layer*. Plant Journal, 2008. **56**(4): p. 531-538.
46. Schreiber, N., et al., *G-fibres in storage roots of Trifolium pratense (Fabaceae): tensile stress generators for contraction*. Plant Journal, 2010. **61**(5): p. 854-861.
47. Dawson, J., J.F.V. Vincent, and A.M. Rocca, *How pine cones open*. Nature, 1997. **390**(6661): p. 668-668.
48. Elbaum, R., S. Gorb, and P. Fratzl, *Structures in the cell wall that enable hygroscopic movement of wheat awns*. Journal of Structural Biology, 2008. **164**(1): p. 101-107.
49. Elbaum, R., et al., *The role of wheat awns in the seed dispersal unit*. Science, 2007. **316**(5826): p. 884-886.
50. Timoshenko, S., *Analysis of bi-metal thermostats*. Journal of the Optical Society of America and Review of Scientific Instruments, 1925. **11**(3): p. 233-255.
51. Armon, S., et al., *Geometry and Mechanics in the Opening of Chiral Seed Pods*. Science, 2011. **333**(6050): p. 1726-1730.
52. Forterre, Y. and J. Dumais, *Generating Helices in Nature*. Science, 2011. **333**(6050): p. 1715-1716.
53. Wu, Z.L., et al., *Three-dimensional shape transformations of hydrogel sheets induced by small-scale modulation of internal stresses*. Nature Communications, 2013. **4**.
54. Aharoni, H., et al., *Emergence of Spontaneous Twist and Curvature in Non-Euclidean Rods: Application to Erodium Plant Cells*. Physical Review Letters, 2012. **108**(23).
55. Gemeinhart, R.A., et al., *pH-sensitivity of fast responsive superporous hydrogels*. Journal of Biomaterials Science-Polymer Edition, 2000. **11**(12): p. 1371-1380.
56. Deshpande, V.S., M.F. Ashby, and N.A. Fleck, *Foam topology bending versus stretching dominated architectures*. Acta Materialia, 2001. **49**(6): p. 1035-1040.

## 6. References

57. Grima, J.N., et al., *Hexagonal Honeycombs with Zero Poisson's Ratios and Enhanced Stiffness*. Advanced Engineering Materials, 2010. **12**(9): p. 855-862.
58. Onck, P.R., E.W. Andrews, and L.J. Gibson, *Size effects in ductile cellular solids. Part I: modeling*. International Journal of Mechanical Sciences, 2001. **43**(3): p. 681-699.
59. Andrews, E.W., et al., *Size effects in ductile cellular solids. Part II: experimental results*. International Journal of Mechanical Sciences, 2001. **43**(3): p. 701-713.
60. Zhu, H.X., J.R. Hobdell, and A.H. Windle, *Effects of cell irregularity on the elastic properties of 2D Voronoi honeycombs*. Journal of the Mechanics and Physics of Solids, 2001. **49**(4): p. 857-870.
61. Zhu, H.X., J.R. Hobdell, and A.H. Windle, *Effects of cell irregularity on the elastic properties of open-cell foams*. Acta Materialia, 2000. **48**(20): p. 4893-4900.
62. Zhu, H.X. and A.H. Windle, *Effects of cell irregularity on the high strain compression of open-cell foams*. Acta Materialia, 2002. **50**(5): p. 1041-1052.
63. Silva, M.J. and L.J. Gibson, *The effects of non-periodic microstructure and defects on the compressive strength of two-dimensional cellular solids*. International Journal of Mechanical Sciences, 1997. **39**(5): p. 549-563.
64. Alkhader, M. and M. Vural, *Mechanical response of cellular solids: Role of cellular topology and microstructural irregularity*. International Journal of Engineering Science, 2008. **46**(10): p. 1035-1051.
65. Overaker, D.W., A.M. Cuitino, and N.A. Langrana, *Effects of morphology and orientation on the behavior of two-dimensional hexagonal foams and application in a re-entrant foam anchor model (vol 29, pg 43, 1998)*. Mechanics of Materials, 1999. **31**(4): p. 295-295.
66. Tekoglu, C. and P.R. Onck, *Size effects in two-dimensional Voronoi foams: A comparison between generalized continua and discrete models*. Journal of the Mechanics and Physics of Solids, 2008. **56**(12): p. 3541-3564.
67. Tekoglu, C., et al., *Size effects in foams: Experiments and modeling*. Progress in Materials Science, 2011. **56**(2): p. 109-138.
68. Gibson, L.J. and M.F. Ashby, *Cellular solids : structure and properties*. 2nd ed. ed. 1997, Cambridge: Cambridge University Press.
69. Fleck, N.A., V.S. Deshpande, and M.F. Ashby, *Micro-architected materials: past, present and future*. Proceedings of the Royal Society a-Mathematical Physical and Engineering Sciences, 2010. **466**(2121): p. 2495-2516.
70. Kanit, T., et al., *Determination of the size of the representative volume element for random composites: statistical and numerical approach*. International Journal of Solids and Structures, 2003. **40**(13-14): p. 3647-3679.
71. Lantuejoul, C., *Ergodicity and Integral Range*. Journal of Microscopy-Oxford, 1991. **161**: p. 387-403.
72. Jounaid, F. and K. Sab, *Elastic Buckling of 2-D Random Honeycombs: Does a Representative Volume Element Exist?* Iutam Symposium on Mechanical Properties of Cellular Materials, 2009. **12**: p. 77-86.
73. Sab, K., *On the Homogenization and the Simulation of Random Materials*. European Journal of Mechanics a-Solids, 1992. **11**(5): p. 585-607.

74. Forest, S., *Some Elements of the Mechanics of Continua*. 2010. **Archimat - First School on Architected Materials**.
75. Dirrenberger, J., S. Forest, and D. Jeulin, *Effective elastic properties of auxetic microstructures: anisotropy and structural applications*. International Journal of Mechanics and Materials in Design, 2013. **9**(1): p. 21-33.
76. Treloar, L.R.G., *The physics of rubber elasticity*. 3rd ed. ed. 2005, Oxford: Oxford University.
77. Flory, P.J., *Thermodynamics of high polymer solutions*. Journal of Chemical Physics, 1941. **9**(8): p. 660-661.
78. Guth, E. and H. Mark, *The elasticity of rubber and its connection with the structural model*. Naturwissenschaften, 1937. **25**: p. 353-359.
79. Rouquerol, F.o., J. Rouquerol, and K.S.W. Sing, *Adsorption by powders and porous solids : principles, methodology and applications*. 1999, San Diego, Calif. ; London: Academic Press.
80. Zickler, G.A., et al., *Physisorbed films in periodic mesoporous silica studied by in situ synchrotron small-angle diffraction*. Physical Review B, 2006. **73**(18).
81. Erko, M., et al., *Confinement-induced structural changes of water studied by Raman scattering*. Physical Review B, 2011. **84**(10).
82. Erko, M., et al., *Repeated sorption of water in SBA-15 investigated by means of in situ small-angle x-ray scattering*. Journal of Physics-Condensed Matter, 2012. **24**(28).
83. Zabler, S., et al., *Moisture changes in the plant cell wall force cellulose crystallites to deform*. Journal of Structural Biology, 2010. **171**(2): p. 133-141.
84. Zienkiewicz, O.C. and R.L. Taylor, *The finite element method. Vol. 1, The basis*. 5th ed. ed. 2000, Oxford: Butterworth-Heinemann.
85. Salmen, L., *Micromechanical understanding of the cell-wall structure*. Comptes Rendus Biologies, 2004. **327**(9-10): p. 873-880.
86. Buxton, G.A., C.M. Care, and D.J. Cleaver, *A lattice spring model of heterogeneous materials with plasticity*. Modelling and Simulation in Materials Science and Engineering, 2001. **9**(6): p. 485-497.
87. Hassold, G.N. and D.J. Srolovitz, *Brittle-Fracture in Materials with Random Defects*. Physical Review B, 1989. **39**(13): p. 9273-9281.
88. Lakes, R., *Deformation Mechanisms in Negative Poisson Ratio Materials - Structural Aspects*. Journal of Materials Science, 1991. **26**(9): p. 2287-2292.
89. Fratzl, P. and O. Penrose, *Ising model for phase separation in alloys with anisotropic elastic interaction .2. A computer experiment*. Acta Materialia, 1996. **44**(8): p. 3227-3239.
90. Schneider, C.A., W.S. Rasband, and K.W. Eliceiri, *NIH Image to ImageJ: 25 years of image analysis*. Nature Methods, 2012. **9**(7): p. 671-675.
91. Allen, M.P. and D.J. Tildesley, *Computer simulation of liquids*. 1987, Oxford: Clarendon.
92. Frenkel, D. and B. Smit, *Understanding molecular simulation : from algorithms to applications*. 2nd ed. ed. 2002, San Diego ; London: Academic Press.
93. Schoen, M. and S. Klapp, *Nanoconfined fluids: Soft matter between two and three dimensions*. Reviews of Computational Chemistry, 2007. **24**: p. 1-517.



## 6. References

94. Abascal, J.L.F. and C. Vega, *A general purpose model for the condensed phases of water: TIP4P/2005*. Journal of Chemical Physics, 2005. **123**(23).
95. Jorgensen, W.L., et al., *Comparison of Simple Potential Functions for Simulating Liquid Water*. Journal of Chemical Physics, 1983. **79**(2): p. 926-935.
96. Soper, A.K., *The radial distribution functions of water and ice from 220 to 673 K and at pressures up to 400 MPa*. Chemical Physics, 2000. **258**(2-3): p. 121-137.
97. Rafsanjani, A., et al., *Swelling of cellular solids: From conventional to re-entrant honeycombs*. Applied Physics Letters, 2013. **102**(21).
98. Zupan, M., M.F. Ashby, and N.A. Fleck, *Actuator classification and selection - The development of a database*. Advanced Engineering Materials, 2002. **4**(12): p. 933-940.
99. Urayama, K. and T. Takigawa, *Volume of polymer gels coupled to deformation*. Soft Matter, 2012. **8**(31): p. 8017-8029.
100. Bertoldi, K., et al., *Mechanics of deformation-triggered pattern transformations and superelastic behavior in periodic elastomeric structures*. Journal of the Mechanics and Physics of Solids, 2008. **56**(8): p. 2642-2668.
101. Shim, J., et al., *Buckling-induced encapsulation of structured elastic shells under pressure*. Proceedings of the National Academy of Sciences of the United States of America, 2012. **109**(16): p. 5978-5983.
102. Sidorenko, A., et al., *Reversible switching of hydrogel-actuated nanostructures into complex micropatterns*. Science, 2007. **315**(5811): p. 487-490.

## Acknowledgements

This section deserves at least the same attention as the rest of this dissertation, because it is really important for me to say thanks to all the great scientists I met here.

But... I'm really in a hurry<sup>\*</sup> for the submission and therefore I have to be concise and probably not as verbose as I would like. Apologies if I might forget someone!

My first and biggest thanks go to John W. C. Dunlop: it was great to have you as a supervisor and I cannot even say how thankful I am for all the support you gave me, both as a scientist and as a friend. I stopped counting your emails ending with a: "No problems at all!", after I was asking for help or I was late for some deadline. I never found a person as willing to help as you. When I was on a down phase with my research you were always there to show me new possibilities. Also, you taught me how fun science is, and, in the end, that's why it is worth doing it.

Next, my supervisor Peter Fratzl. I really enjoyed working with you. Especially I learned how important it is to keep things simple when possible, in order to get the most out of our research. When I discussed my project with you (and this happened many times) I could see the paradigm of the successful scientist in action: seeing interesting problems in our natural world, being rigorous in their analysis, sharp in finding a possible explanation and really able to put it "in the bigger picture", making their broad implications accessible to everyone.

My most felt thanks also go to Yves Bréchet, a great material scientist and *philosopher* (this would have been a fitting definition for you in the eighteenth century: maybe still valid?). Everything I said about Peter applies to you too; so imagine how glad I was to discuss with both of you at the same time! This was really great, at least as great as your *motto* about why you prefer cats to dogs!

---

<sup>\*</sup> as usual

Next I really want to acknowledge the great support that Luca Bertinetti was providing me. I hope you had fun helping a biomedical engineer as me approaching physical chemistry; I surely had it while seeing how mechanics would be digested by a chemist as you!

Big thanks to Marco Mazza, my compatriot, it has been a pleasure to work with you. The dedication you showed when we were working together was admirable. You taught me a lot, especially not to give up; citing your words: “the bug has to be somewhere!”

A lot of thanks also to James Weaver, our personal Santa Claus from overseas. You showed me how aesthetic science can be and how important is to convey this beauty when we present it. Please remember me to record one of your talks in the next conferences, who knows, maybe one day I will be able to talk half as fast as you?

Great thanks go to all the people in my group: Sebastien Turcaud and Cecile Bidan especially. Sebastien, how many scientific discussions did we have together? And how late was it when we were having them? Cecile, I have always been amazed by how efficiently you work: can you teach that to me?

All the other people in the Biomaterials Department: Igor, Lena, Roman, Jens, Yael, Khashayar, Felix, Luca, Admir, Maria, Agata, Teresa, Mathieu, Bernd, Susann, but also those who left already: Andre, Dmitri, Anayancy, Steffi, Caro and so on and so forth...you have been and will be my second family here. Thanks for the great time together!

A big hug and thanks go to my dad Carlo and mom Lia, my sister Benedetta and my “little” brother Andrea. I thank you for the support and the love and the teachings: simply for being there –even if a bit far away now.

And now, as last, the most difficult person to thank. Fede, *amore mio*, these with you have been dense years, isn’t it? I will never be enough thankful to you, for the moral



support you gave me, the intelligent way you supported me (because you are probably the most intelligent person I know, but at the same time the only crazy one who still wants to live at my side). We were (I for sure) almost kids when we started our common adventure and look at us now: Eugenio, our small *passerotto* joined our company since not even three months... *Grazie infinitamente per tutto l'amore e la fiducia e il rispetto... Ti amo piccolina mia!*